Study of the impact of the troposphere on Galileo navigation signals

Travail de fin d'étude réalisé par
Bertrand BONFOND
en vue de l'obtention du grade
d'ingénieur civil physicien
tendance techniques spatiales

ULg Promoter: Jean Pierre SWINGS
ESA Supervisor: Antonio MARTELLUCCI

Université de Liège
Academic year 2004-2005

September 22, 2005

Abstract

This work consists in a validation exercise for the tropospheric delay model that will be used in Galileo. A comparison between several models of the troposphere has been performed; the models have been evaluated using existing experimental measurements or maps generated from assimilation of experimental data.

The first chapter is a small general overview of the Galileo project with a particular regard to tropospheric effects on the propagation of the signals.

In the second chapter a description and a comparison of different ways of determining the tropospheric delay (vertical integration, models based on surface measurements and blind models) are exposed. In this chapter, an updated discussion on the refractivity coefficients is also presented.

The third and the fourth chapters expose how the two validation exercises have been performed. The sources used for this work come from the British Atmospheric Data Center as well as data gathered during the validation campaign of Ra2, the RADAR altimeter of ESA's Envisat Earth observation satellite. A critical analysis of the existing procedures has been performed and new ones have been developed. As far as radiosonde data are concerned, some serious improvements in the processing of the measurements have been found. The results of this work have led to an evaluation of the performances of the models in several sites of the world.

Concerning the second data set, we focused on the Numerical Weather Prediction data in order to assess the ESA model on a worldwide basis. The procedures used to derive the delay from these data have been studied in depth. Finally an assessment of the models during the Ra2 validation campaign is exposed.

The last chapter is consecrated to the conclusion of these analyses and validations, knowing that some points underlined during this study will be useful for the next versions of the Galileo tropospheric model.

Travail de fin d'étude réalisé par
Bertrand BONFOND
en vue de l'obtention du grade
d'ingénieur civil physicien
tendance techniques spatiales
Année académique 2004-2005

Contents

Acknowledgment

I would like to acknowledge Dr. Antonio Martellucci from ESA/ESTEC for his teaching, his advice and for the time he granted me.

I am also grateful to Pr. Jean-Pierre Swings from the University of Liège and to M. Peter Claes from ESA/ESTEC for letting me work at the European Space Research and Technology Center (ESTEC) on the Galileo Project.

I would like to thank the staff of the TE-EE division, and particularly my office mates Chiara Civitelli, Christina Dinis and Vanja Platzic. Among the TEC-EEP, my special thanks go to Dr. Bertram Arbesser-Rastburg and Dr. Pedro Baptista for the information they provided me.

Finally I would like to thank Joseph Bonfond, Benoît Ferrière and Luca Matarazzo for spending hours in re-reading my work and providing me English feedback.

Chapter 1

Overview of the Galileo project

1.1 Introduction

In the first sections of this chapter, a short overview of the Galileo Navigation System will be presented. Please keep in mind that the aim of this approach is to replace this work on his context and not to give an extensive description of the whole Galileo Project. As the reader will progress in the document, more precisions will be given on the structure of the atmosphere and on the possible causes on inaccuracies due to the propagation of the signal in its different layers. Of course I will finally focus on the tropospheric effects.

1.2 Global Navigation Satellite Systems

The most famous Global Navigation Satellite System (GNSS) is of course the US Global Positioning System (GPS). Actually the Russian Federation has another comparable GNSS project called Glonass. Initially these systems have been conceived for strategical military reasons: they are used to guide military planes, ships, troops, missiles or even bombs. Nowadays, the GPS constellation is composed of 27 operational satellites[1] and is complete. Only 7 Glonass satellites have been launched until now but the complete deployment of the system requires 24 satellites. These systems are under military control but some channels of these signals are open to civil users.

The applications of GNSS based services now have a big success. As the number of users will still increase, the economical importance of these applications will increase in the same way. Aviation and shipping are the more obvious areas where navigation signals are very useful. It will also help emergency services, like fire brigades or sea rescue, to be more efficient. Nowadays, more and more GPS

[1] In fact only 24 of them are in use, the 3 remaining ones will be activated in case of failure of one of them in order to ensure continuity of the signals.

receivers are placed in taxis, lorries or cars in order to help the drivers to find their way. In combination with locally provided information (with GPRS or UMTS), it could avoid traffic jams and reduce travel time and pollution. GNSS provide in their signals a very stable time reference, which can also be used to facilitate interconnection between communication, banking or electrical networks.

Nevertheless the use of these signals can be problematic. First of all the reliability of the signals is not constant and the high latitude regions are not well covered. The integrity of the signals is not guaranteed either, which means that the user has no indication of the reliability on the displayed position. This can be anecdotal for car receivers, but it is more problematic when GPS is used to guide a civil airplane with several hundreds of passengers on-board. Then the governments controlling the constellations can decide for any reasons to switch down the availability of the signals for civil users. If GPS based services are widely spread, this can severely affect the economy and even endanger human lives.

For political and economical independence reasons, the European Commission, in collaboration with the European Space Agency, has decided to create its own GNSS called Galileo. The overall cost of the project is estimated around 3,4 billion of Euros.

Actually Galileo will not be the first step of the European navigation policy. In collaboration with Eurocontrol, the European Commission and ESA have deployed the European Geostationary Navigation Overlay Service (EGNOS)[2], a system designed to improve the GPS signals. It consists in a network of sensors all over Europe measuring the GPS signals and providing a correction by means of three geostationary satellites. Analogue systems are in operation over USA (WAAS) and over Japan (MSAS).

1.3 The Galileo Project

The global idea of a GNSS system is the following one. A constellation of satellite provides time signals. The receiver picks up the signals (at least three satellites must be visible), determines the propagating time for each emitter and converts it into the relative distance to the satellites and finally provides the position of the user.

The Galileo system can be divided in three segments, the User segment, the Space segment and the Ground segment.

The User Segment consists in the development of receivers and related applications.

The Galileo Space Segment will be composed of 30 satellites orbiting along 3 circular orbits at an altitude of 23222 km (Medium Earth Orbit). The orbit planes will be inclined at 56° to the equator. In each plane, 9 satellites will

[2]The service will be fully available in 2006 when the Safety-of-Life service will be certified.

provide navigation signals, and one will be dormant, ready to be activated in case of failure of one other. Each satellite will weight approximately 700 kg, so that several of them can be launched by a single rocket. In order to provide a precise time reference, two atomic clocks will be placed in each spaceship: a Rubidium Atomic Frequency Standard and a Passive Hydrogen Maser.

The Galileo Ground Segment consists in a worldwide network of sensor stations, control centers[3] and uplink stations. Their purpose is to monitor the quality of the signals, to gather and process the data, and finally to provide the corrections to be applied.

Five types of services are defined in the project:

- The Open Service (OS). Free of charge and destined to the mass market, this service provides timing and positioning signals to any user equipped with a receiver. No integrity message is sent to the user.

- The Safety-of-Life (SoL) service. The accuracy of this service will be the same as for the OS, but an integrity message is also provided. This service will be used mainly in transport applications. The future Galileo Operating Company (GOC) will certify and guaranty this service. Certified dual frequency receivers will be required.

- Commercial Service (CS). On payment of a fee, two additional encrypted signals can be provided to the users. The value-added information provided will depend on the needs of the user. It can be independent data for their own applications or data improving timing or positioning accuracy.

- The Public Regulated Service (PSR). This service will be mainly used by the police, coastguards or customs. The characteristics of this service are the encryption and the robustness against jamming[4] and spoofing[5].

- The Search And Rescue (SAR) service. Complementing the current COSPAS-SARSAT system[6], Galileo will serve as a relay for distress signals. It will reduce the time of response of the system and will permit a more precise localisation of the emitting beacon.

[3]The control center is, in a way, the head of the system: the orbit and clock errors are computed here, as well as the integrity of the signals. Two control centers are planned, for redundancy reasons.

[4]Jamming consists in the emission of a signal that disrupts the correct transmission of the navigation signals. It can be intentional or unintentional.

[5]Spoofing consists in emitting a misleading signal that looks like a navigation signal but which is not the one sent by the satellite.

[6]The current COSPAS-SARSAT system is composed of 4 Low Earth Orbit and 3 geostationary satellites.

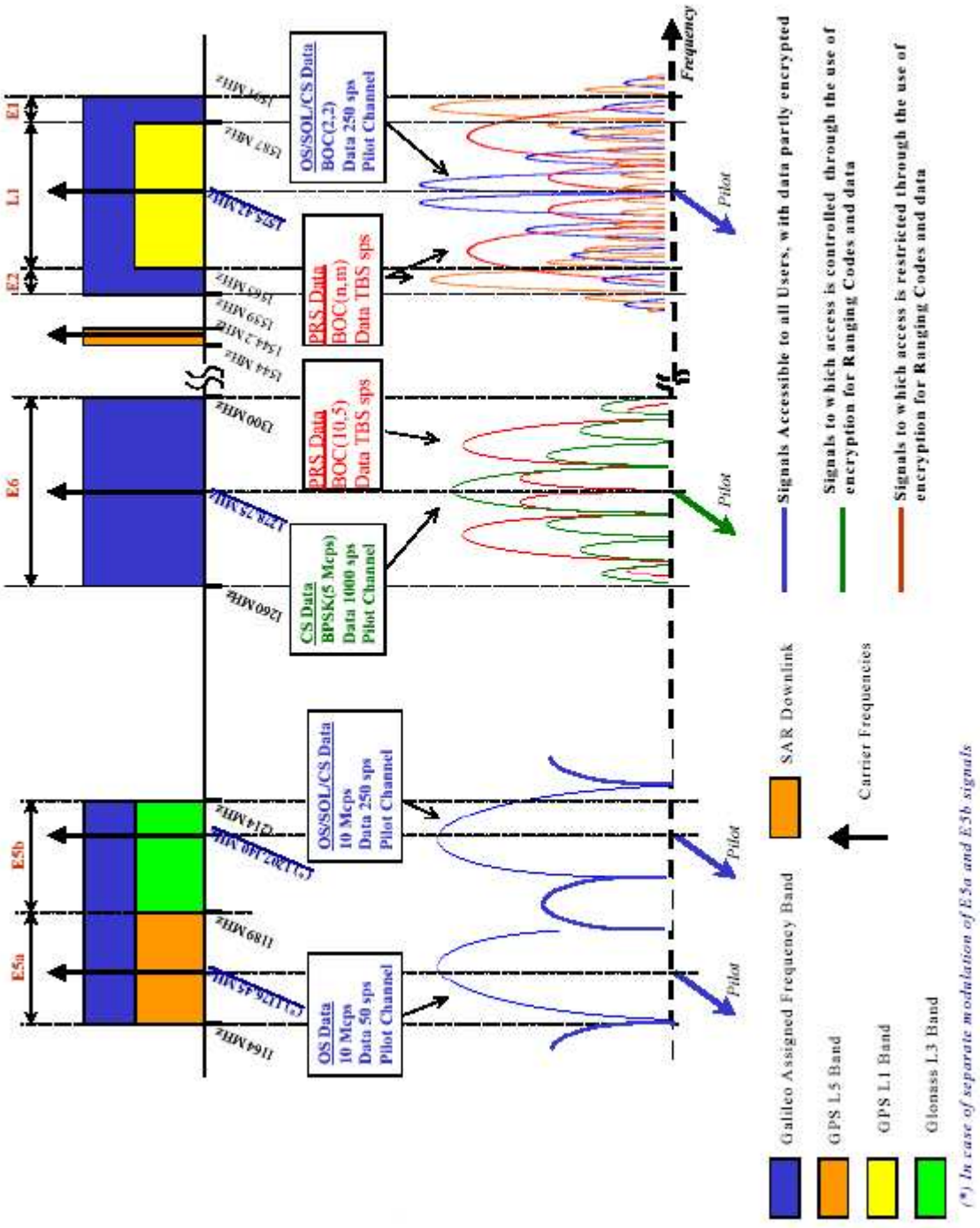

Figure 1.1: Galileo frequency spectrum.

The overall system is planned to be operational in 2008. In order to be ready at this date, many tests and simulations have been and will be performed. Two main simulation tools are the Galileo System Simulation Facility (GSSF) and the Galileo Signal Validation Facility (GSVF). The first one is an end-to-end simulation software built to model all the elements of the ground, the space or the user segment. With this tool, the behaviour (accuracy, integrity, etc.) of the complete system can be simulated in any configuration. The GSVF is conceived to assess the user receivers. It provides a realistic signal that can be introduced in the receivers instead of the signal coming from the antenna in order to test the receiver algorithms and electronics.

Before launching the satellite constellation, two large scale exercises have been planned: the Galileo System Test Bed -Version 1 and 2 (GSTB-V1 and GSTB-V2). The first one has been completed in early 2004, and consisted in an experimental ground segment. The second test bed is planned for the end of 2005 and will consist in an in-orbit validation of two experimental satellites.

During this huge set of studies gathered in GSTB-V1, performances of the ESA tropospheric models have already been assessed and lead to improvements of the model. Our work is in fact a kind of prolongation of these studies, as the model has evolved since. All the evaluations of the ESA tropospheric model have been performed by external contractors, but now ESA wishes to build an internal validation tool for the fine-tuning of the model.

1.4 Signal perturbations

Several effects can affect the precision of the signals. Errors can come from:

- clock imprecision effects,
- orbit errors,
- relativistic effects,
- atmospheric effects,
- multi-path problems.

The time provided by the atomic clocks will be regularly compared to time measured on Earth and the needed information will be sent directly to the satellites for on-board corrections. The orbital errors can also be corrected directly because the satellites are equipped with motors. The relativistic effects are multiple: the frequency shift due to the Einstein effect and effects due to the fact that the orbits are not perfectly circular, which induces a altitude variations, accelerations and

related perturbations of the signal. These effects are very predictable and easily modelled.

For the atmospheric effects, the problem is more complex, because the perturbations are out of control for the system as it will be explained in detail in the next section. Multi-path problems will not be discussed here.

1.4.1 Atmospheric effects

1.4.1.1 Atmospheric layers

Scientists decompose earth atmosphere in different layers according to various criteria. The most commonly used is the temperature profile.

The lower part is called the troposphere, it contains the major part of the total air mass. It is characterized by a nearly constant decrease of the temperature. The higher limit of this layer is the tropopause. With a temperature comprised between 190 K and 220 K, its altitude varies from 15 km at the equator to 8 km at the poles. Just above the troposphere is the stratosphere, which is characterized first by a stabilisation of the temperature and then by an increase of it, mainly due to interactions between UV rays ($\lambda < 3000$Å) and ozone molecules. The upper frontier of this layer is called the stratopause, at an altitude of approximately 50 km and a temperature of 270K. Then the mesosphere begins where the temperature declines again. The mesopause stands 85km above the surface at temperature of 190K. Finally the upper layer is the thermosphere where the temperature increases asymptotically up to 1000K[7].

Another criterion based on the charge of the particles is also used to distinguish two atmospheric parts. The first 100km of the atmosphere are mainly composed of neutral molecules. Then the ionosphere begins , which owes its name to its composition: mainly ionized particles created by the interaction of the upper atmosphere and solar radiations.

[7]This is a cinematic temperature, linked to the mean quadratic speed of the particles. The density of this layer is very low and the thermodynamic equilibrium is not respected anymore.

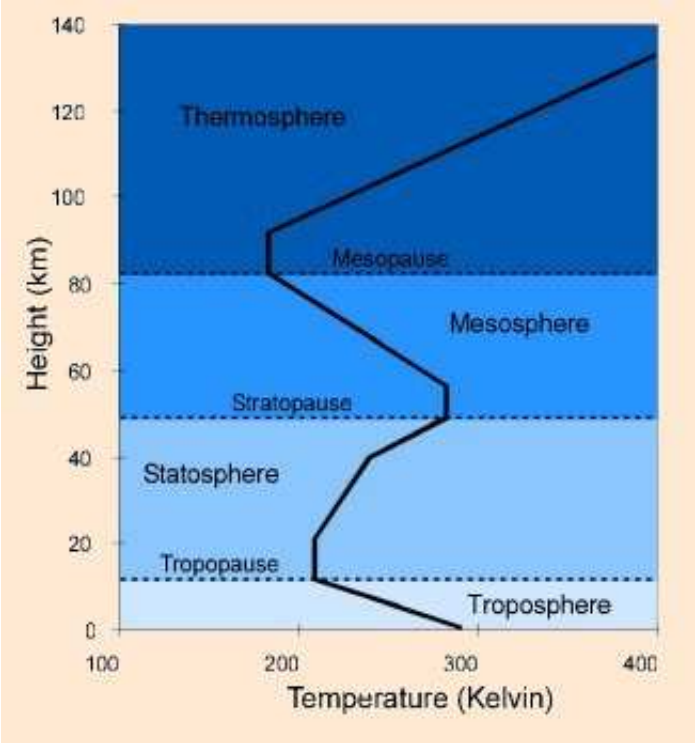

Figure 1.2: Illustration of the layers of the atmosphere and of the temperature profile. (image coming from http://www.ace.mmu.ac.uk/eae/Atmosphere/Older/Atmospheric_Layers.html).

This is the more widespread picture of the atmospheric profile and the more commonly accepted definitions of the layers. You will see in the following sections that these conventions are rarely respected in the domain we are interested in. This is not due to a poor understanding of the atmosphere but to the specific needs inherent to the study of the propagation of signals in the atmosphere.

1.4.1.2 The Ionospheric Delay

To illustrate directly what has been said in the previous paragraph, Bevis and al. [6] consider in their appendix that the ionosphere begins approximately at 50km and finishes at 1000km, simply because this is the relevant extension to estimate the contribution of the charged particles to the perturbation of the signal.

Above 30MHz the electromagnetic waves can propagate through the ionosphere, but the electric charges induce a dispersion of the signal. For a signal coming from the vacuum, the phase velocity of the waves increases but the group velocity is slowed down (so that the celerity is not overtaken). The order of magnitude of the phase advance and of the group delay is approximately the same

and the ionospheric propagation error is equal (at the first order) to:

$$\text{delay} \approx 40,3\frac{TEC}{\nu^2} \tag{1.1}$$

where TEC is the Total Electron Contend in TEC units($1\,TECU = 10^{16}$electrons by square meters), which represents the integrated quantity of electrons along the path between satellite and receiver and ν is the carrier frequency in GHz. A typical daily average value of the zenith delay produced by the ionosphere is 10 meters but the TEC can vary from 1 to $10^3\,TECU$. The amount of free electrons depends mainly on the solar radiation flux that ionizes the atmospheric gas. Phenomena affecting the TEC can be separated in two types: the regular and the irregular ionospheric effects. The first category concerns large variations induced by modification in the average solar radiation interacting with the plasma, such as diurnal cycles, seasonal cycles or sunspot cycles. The second category is induced by violent solar events as coronal mass ejections, proton events or x-flares. When these energetic particles or radiations arrive in the vicinity of the earth, these can cause geomagnetic storms, ionospheric storms, travelling ionospheric disturbances, etc. which then perturb the phase, the amplitude and the delay of the wave.

There are actually three ways to take the ionospheric delay into account. The first one uses dual frequency receivers. If we measure the distance between the satellite and the receiver at two different carrier frequencies, we can simply get rid of the unknown TEC in equation (1.1). That is the reason why the GPS dual frequency receivers use the frequency bands L1 at 1.57542 GHz and L2 at 1.22760 GHz. In Galileo, even for Open Service users, several frequencies will be available. With this method we can get rid of the first order errors, but second order errors still remain. One example of second order effect results from the fact that as the electromagnetic path is not the same for the two frequencies, it may go through regions of different electronic densities (see figure (1.3)). This results in a lack of accuracy in the recovered electronic contend.

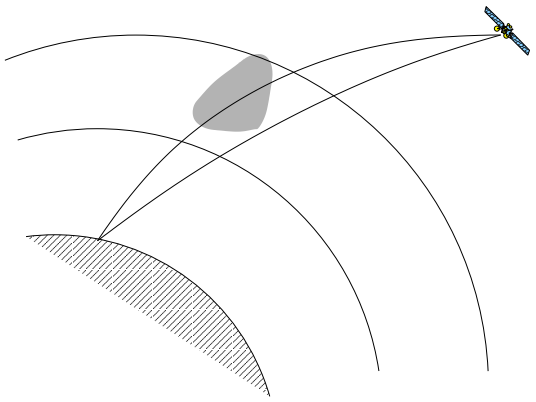

Figure 1.3: Schema of the electric path of the two signals emitted at two different frequencies. If one of them passes through a zone characterized by a different TEC, this could result in a decrease of the accuracy in the estimation of the ionospheric delay.

Unfortunately, most of the receivers use or will only use a single frequency signal. For these receivers the ionospheric delay has to be modeled. As the ionospheric delay is a very variable delay (from 1 meter to 100 meters depending on the state of the ionosphere), and as these variations cannot be predicted, the system (GPS or Galileo) has to provide to the receiver some parameters to enter inside the model. GPS simple receivers use the Klobuchar model where the ionosphere is described by 8 parameters contained in the GPS signal.

Galileo will use a more refined 3D model of the ionosphere that only requires 3 parameters: the Nequick model. These parameters will be generated from the observations performed by the ground stations during the previous day and will be updated every 24 hours. The ionospheric delay is calculated from the 3 coefficients, from the latitude of the receiver and from the hour of the day. If an ionospheric storm or any event causing a loss of accuracy out of the tolerated range is detected by the ground stations, a flag is immediately risen in the transmitted signals. The users will be immediately warned of the loss of reliability of the positioning, which is not the case for GPS receivers.

A third and even more accurate technique is used by EGNOS (and the other augmentations of the GPS system). For EGNOS receivers, a detailed map[8] of the ionospheric delay is calculated thanks to a dense network of ground stations and provided to the receivers every 5 minutes.

[8]This map has a 5° resolution in latitude and longitude but only covers the zone concerned by the augmentation.

1.4.1.3 The Tropospheric Delay

When an electromagnetic radiation propagates in the neutral part of the atmosphere, it is also altered. In the frequency range used by the GPS and Galileo (1200-1500MHz), the dispersion phenomenon is nearly negligible.

In the 1-2GHz frequency domain, the atmospheric absorption is mainly due to oxygen, but this is also insignificant. To give an order of magnitude, let us imagine a satellite situated at zenith, the attenuation due to the propagation of the signal through the troposphere would only be of $0,035\,dB$ (see Spilker's paper [44] for example).

Another perturbation could come from scintillation, but the impact of atmospheric turbulence only appears at very low elevation angles. If these angles are useful in VLBI[9] applications, they are not appropriate for navigation. In practice, for ground users, the horizon is rarely open enough to see satellite at low elevation angles, so that the minimal elevation angle is set to 15° in order to avoid multipath problems. For receivers placed in planes, the minimal elevation angle is also fixed at 15 degrees, because of possible perturbations induced by the wings and the fuselage.

The only important perturbations introduced by the neutral atmosphere are due to the refraction which slows down the speed of the signal and bends its trajectory. This phenomenon is called "*tropospheric delay*", which is twice an improper appellation, because this delay is always expressed in length units and not in time units and because about 25% of the tropospheric delay does not take place in the troposphere.

The electrical path of the signal is expressed as the integral of the refraction index along the trajectory followed by the signal.

$$L = \int_S n\, ds \tag{1.2}$$

This path is not exactly a straight line as it would be in the vacuum because of the Fermat's Principle[10]. What we call *tropospheric delay* is in fact the difference between the real electric path and the shorter geometric path:

$$\Delta L = \int_S n\, ds - G \tag{1.3}$$

where G stands for the geometrical straight-line length.

1.4.1.3.1 Refraction But before diving into the geometrical considerations, a little physical explanation would be suitable. The scattering of the incident wave

[9] Very Long Baseline Interferometry.

[10] The modern statement of Fermat's Principle is: "A light ray, in going between two points, must traverse an optical path length which is stationary with respect to variations of the path".

by bound charges in the air molecules induces scattered waves which combine themselves with the incident wave to form a slightly retarded wave. To explain the phenomenon, two approaches are possible, the classical physics and the quantum physics. The second point of view is indispensable to get precise results, but the first one provides an easier way to explain the phenomenon.

Let us imagine a free electron submitted to an electromagnetic wave. It oscillates in phase with the incident electric vector and thus creates an electric field, the direction of which is opposite to the first one. This results in a net electric field equal to zero and in this case we can see that there is a phase reversal for the scattered wave .

On the other hand, bound electrons experience a restoring force so that there is no change of phase of 180° anymore. This situation is very similar to a system composed of a mass (representing the electron) attached to a string with a certain stiffness (representing the bond) and the extremity of which is a fixed point (representing the core). This system corresponds to the following expression of the Newton law, which equals the sum of the electric force and the restoring force to the acceleration of the electron multiplied by its mass:

$$-eE_0e^{-i\omega t} - kx = m_e\ddot{x}$$

where e is the the absolute value of the charge of the electron. If we assume that the displacement of the electron is oscillatory (i.e. $x = Xe^{-i\omega t}$) we can write:

$$-eE_0 - kX = -\omega^2 m_e X$$

so that, taking into account that $k = \omega^2{}_0 m_e$, we obtain:

$$X = \frac{-eE}{k - \omega^2 m_e} = \frac{-eE}{m_e(\omega^2{}_0 - \omega^2)}$$

We can replace this expression in the definition of the dipolar momentum of the atom:

$$p = -ex = \frac{e^2 E}{m_e(\omega^2{}_0 - \omega^2)}$$

and then , according to the definition of the polarity $P = Np$ where N is the specific density of atoms and to the definition of the electric displacement

$$\begin{aligned} D &= \epsilon E \\ &= E + P \\ &= \left(1 + \frac{Ne^2}{(\omega^2{}_0 - \omega^2)m_e}\right) E \end{aligned}$$

We also know that

$$n = \sqrt{\mu\epsilon} \tag{1.4}$$

and finally we have

$$n = \sqrt{\mu(1 + \frac{Ne^2}{(\omega^2{}_0 - \omega^2)m_e})}$$

If the incident frequency becomes equal to the natural frequency, the amplitude X increases and an absorption occurs. When the incident frequency is far lower than the incident frequency, the electric vector becomes in phase with the incident vector. This classical model describes quite well the behaviour of the refractivity index for dry air because the natural frequencies of the induced dipoles ν_0 usually lie in the ultraviolet domain for the electrical bonds.

Unfortunately, the case of water is not so easy to model because we have to take into account the dipolar nature of the molecule and the anomalous dispersion, which is due to resonance lines in the IR and microwave domain.

The neutral atmosphere can be considered as a large ensemble of randomly distributed scattering particles. The local electric field being the sum of the electric vector due to the remaining incident radiations and of the electric vectors coming from the scattered waves. To understand more clearly what is happening, imagine two particles reached simultaneously by the incident wave, along a line perpendicular to the wavefront, three contributions are added, the incident wave and the two scattered waves which are a little bit late comparing to the other. The resulting wave is retarded so that this leads to a decrease of the phase speed. Of course, more the medium is dense, more the speed decreases. Nevertheless it is noticeable that this does not necessarily produce any decrease in the amplitude of the propagating wave.

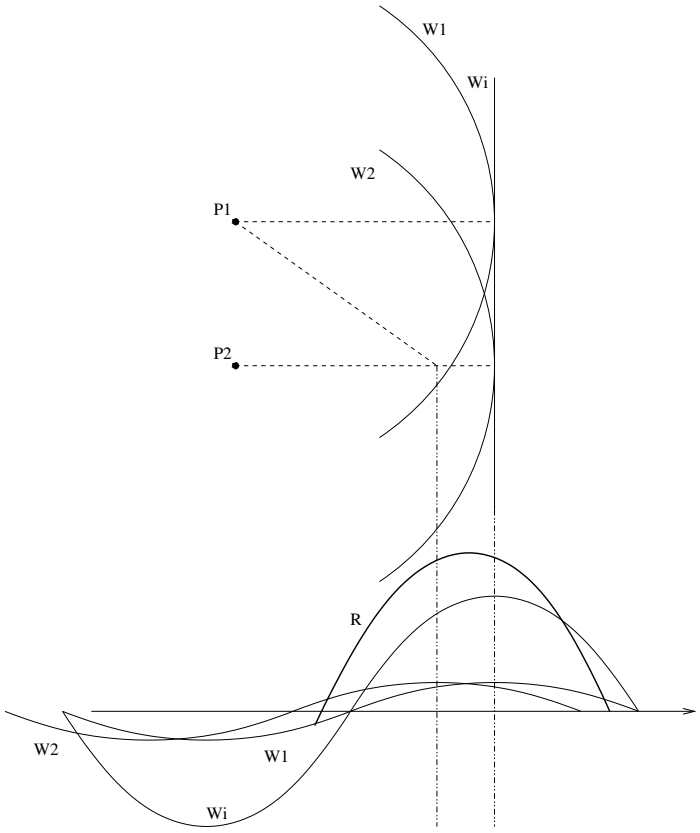

Figure 1.4: (upper part) I is the incident wave, P1 an P2 are the scattering particles and W1 and W2 are the scattered waves. (lower part) Wave profiles along the line perpendicular to the wave front and starting from P1. R is the resultant wave which is retarded comparing to the incident wave.

This diminution of the propagation speed when a media becomes more dense has another consequence: the bending of the wavefront. The relation between the incidence angle and the refracted angle is called the Snell-Descartes's law.

$$\frac{c_1}{c_2} = \frac{\sin i_1}{\sin i_2} \tag{1.5}$$

where c_1 and c_2 are respectively the phase speed in the media 1 and 2 and where i_1 and i_2 are the incident and refraction angles.

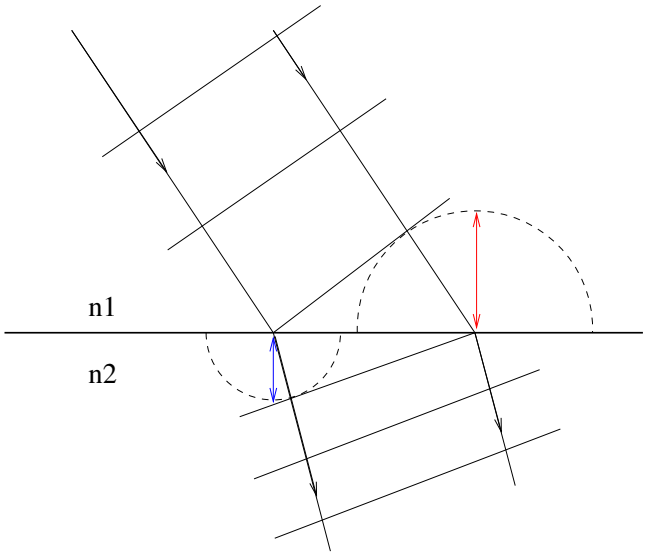

Figure 1.5: Illustration of Snell-Descartes's law. The red arrow represents the length $c_1\Delta t$ and the blue arrow represents $c_2\Delta t$.

1.4.1.3.2 Calculation of the delay We have just seen that the diminution of the speed of the wavefront also bends the rays. We can artificially separate these two effects in the equation (1.3) by writing:

$$\Delta L = \int_S (n-1)\, ds + S - G$$

where S stands for $\int_S ds$. By doing this, we have separated the purely geometric part from the delay caused by the slowing. The delay due to bending

$$\Delta L_g = S - G = \int_S ds - \int_G ds$$

is equal to zero if the elevation angle is equal to 90° and increases as the angle vanishes. For an angle of 10°, the geometric delay is approximately in the order of 3 cm and reaches about 10 cm for an angle of 5°[12].

We could also imagine another way to express equation (4.4):

$$\Delta L = \int_G (n-1)\, ds - \int_G n\, ds + \int_S n\, ds$$

This formula leads to a different definition of the geometric delay, here it will represent the difference between the electric path calculated along the real path and the electric path along the real path, so we will name it $\Delta L'_g$:

$$\Delta L'_g = \int_S n\, ds - \int_G n\, ds$$

According to the Fermat's Principle, we have

$$\Delta L_g > 0 \text{ and } \Delta L'_g < 0$$

In this thesis we will not consider ΔL_g because we will only compare zenith delays. But please notice that both approaches exist in literature. For example, we can see in his paper [8] that Black has adopted the $\Delta L'_g$ convention, while Saastamoinen [41] has adopted the other one.

As the refractive index of air is very near from 1, another quantity is preferably used: the refractivity N defined as:

$$N = (n-1)10^6$$

1.4.1.3.3 Refractivity In literature, the refractivity is expressed as the sum of two parts :

$$N = N_d + N_w$$

where N_d is the refractivity of dry air and N_w is the refractivity of water vapor. We will see in the next chapter that there are many variants of that formula depending of the assumptions adopted by the author, but the principle remains the same. The first part is owed to the non dipolar molecules of the atmosphere. We have seen in a previous paragraph that the refraction index was proportional to the density of the medium. So we can simply write the refractivity of dry air as

$$N_d = n_d - 1 = a\rho_d$$

where ρ_d is the specific mass of dry air and a is a proportionality coefficient.

The case of the water vapor refractivity is a little bit different as this molecule is dipolar. Of course there is an induced dipole part in its expression, but there is also a part dependent on the temperature linked to the re-orientation of the permanent dipole in the incident field.

$$N_w = n_w - 1 = b\rho_w + c\frac{\rho_w}{T}$$

where ρ_w is the water vapour specific mass and T is the temperature. At low temperatures, the incident electric field tends to align the dipoles, which contributes to the total polarisation of the medium and increases the refractivity. But at high temperatures, the thermal agitation tends to orient the dipoles in any directions, so the contribution of the permanent dipoles to the total polarisation becomes smaller.

Chapter 2

Models of the atmosphere

In this chapter several models of the tropospheric delay are presented as well as the assumptions related to these models. Other ways to measure the delay are also mentioned. Then follows a quick discussion on mapping functions. Finally, the last part of the chapter is devoted to a discussion on refractivity coefficients.

2.1 Computation of the delay

2.1.1 Ground based models

The principle of these methods is to model the tropospheric delays thanks to equations describing the physics of the atmosphere. Different assumptions have been performed to get simple equations that only need variables measurable on the ground. In the following section, we will describe three famous classical models.

Some hypothesis are nevertheless common to every model; so we will explain and comment them in a common section, so we can then insist later on the differences.

2.1.1.0.4 Hydrostatic equilibrium All these authors assume that majority of the air constituents are in an hydrostatic equilibrium, excepted for the water vapor:

$$-\frac{1}{\rho}\frac{\partial p}{\partial z} = g$$

where ρ is the density of air, p is the pressure and g is the acceleration of gravity. This equation states that the pressure force per unit mass is equal to the force of gravity per unit mass. In fact the hydrostatic equilibrium is a simplification of the vertical equation of motion which is originally in the form:

$$\frac{Dv_z}{Dt} + 2(\Omega \times V)_z + (\Omega \times (\Omega \times R))_v = -\frac{1}{\rho}\frac{\partial p}{\partial z} - g$$

where Ω is the angular velocity vector of the Earth and V is the fluid velocity vector. The first term represents the total derivative of the vertical speed, the second term represent the Coriolis force and the third term is the centripetal term[1].

Hauser [17] studied the effects of the perturbations of the the hydrostatic equilibrium for laser range measurements. He vertically integrated the equation of motion so that:

$$\int_0^\infty \rho \left(\frac{\partial v_z}{\partial t} + v_x \frac{\partial v_z}{\partial x} + v_y \frac{\partial v_z}{\partial y} + v_z \frac{\partial v_z}{\partial z} - 2\Omega u \cos\phi \right) dz = \int_0^\infty \rho g \, dh - p_0$$

Then he evaluated the biggest possible values for the first member of the equality, which represents the deviation from the hydrostatic equation. In very unlikely cases, he found that the deviation can reach values around 2 hPa (to be compared to $p_0 \sim 1000$ hPa). From this result, we can conclude that these effects can be neglected.

In their book [14], Fleagle and Businger considered that the maximal vertical acceleration in the atmosphere is around $0,1 ms^{-2}$ in thunderstorms, tornadoes and severe turbulence. As this only represents 1% of the gravity force, they also considered that we can neglect its influence without making a big mistake.

2.1.1.0.5 The perfect gas law The perfect gas law states that pressure, density and temperature are linked by the following equation:

$$P_i = \rho_i R T$$

This state relation assumes that the particles interact as if they were hard spheres. This assumption does not provide enough accuracy for our purposes, so that some authors prefer a variant introducing the compressibility Z of the constituents.

$$P_i = \rho_i R T Z_i$$

The inverse of the compressibility for dry air is calculated from this formula given by Thayer [46] (who refers to a papers wrote by Owens [36][2]

$$Z_d^{-1} = 1 + p_d \left[57,90 \times 10^{-8} \left(1 + \frac{0,52}{T} \right) - 9,4611 \times 10^{-4} \frac{t}{T^2} \right]$$

[1]Here we have separated the two terms, but generally this term is included in the acceleration of the gravity.

[2]Davis & al. [9] have given a slightly different formula referring to the same paper from Owens:

$$Z_d^{-1} = 1 + p_d \left[57,97 \times 10^{-8} \left(1 + \frac{0,52}{T} \right) - 9,4611 \times 10^{-4} \frac{t}{T^2} \right]$$

So to decide which one of the two authors was right, we had to go back to the paper from Owens. The given formula is

$$\rho = 348,328 \frac{P}{T} \left[1 + P \left(57,90.10^{-8} - \frac{0,94581.10^{-3}}{T} + \frac{0,25844}{T^2} \right) \right]$$

where p_d is the dry air pressure in hPa, T is the temperature in Kelvin and t is the temperature in Celsius. For the wet inverse compressibility, the author advises the formula:

$$Z_w^{-1} = 1 + 1650 \left(\frac{e}{T^3}\right) \left(1 - 0,01317t + 1,75 \times 10^{-4} t^2 + 1,44 \times 10^{-6} t^3\right)$$

where e is the water vapor pressure in hPa.

Actually the effects of the inverse compressibility are very small and are generally neglected in the models, or, more precisely, a mean of the inverse compressibility is already included in the refractivity coefficients. In order to have an idea of the influence of the dry and the wet inverse compressibilities, we can have a look at the graphics of the inverse compressibilities against the altitude calculated from a radiosonde profile in Uccle. We can observe that the extreme values are 1,006 for the dry part and 1,004 for the wet part.

Knowing that $\rho = \frac{MP}{RTZ}$ and after a little calculations, we came to the conclusion that there was a typographic error in Davis's article. In his thesis, Torben Schuler [45] also refers to Owens but he actually copied the formula from Davis [9].

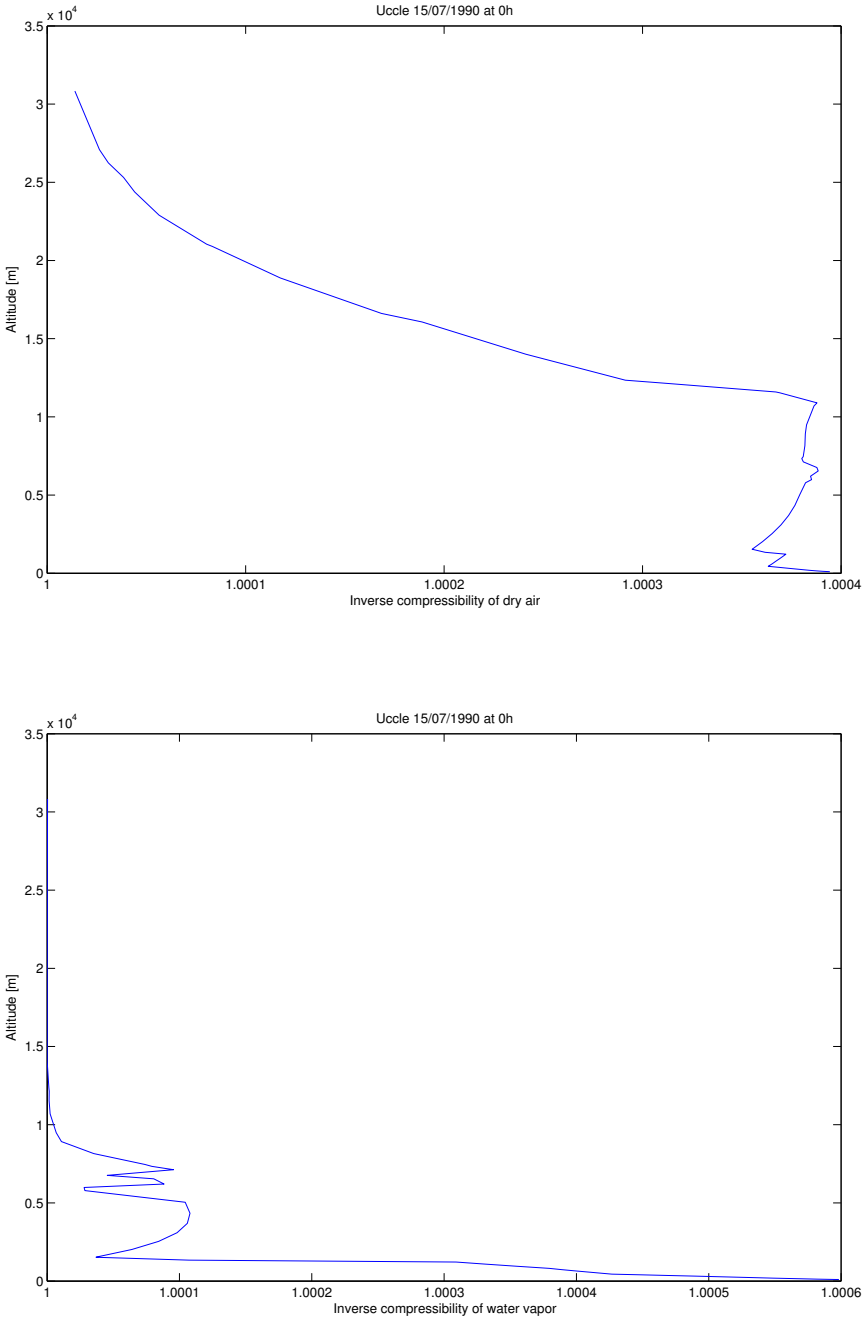

Figure 2.1: *(Top)* Graphic of the inverse dry compressibility as a function of the altitude for a radiosonde profile. The maximal value is equal to 1,006. This value is approximately constant in the troposphere and then decreases. *(Bottom)* Graphic of the inverse wet compressibility as a function of the altitude for a radiosonde profile.

2.1.1.0.6 Convective equilibrium Another important assumption is the linear decease of the temperature with altitude. This assumption comes from the hydrostatic equilibrium, the perfect gas law and the first law of the thermodynamics:

$$\delta Q = PdV + C_v dT + LdW$$

where δQ represents the exchange of heat between the air mass and the external medium, P is the pressure, dV represents an increase in volume of the air mass, C_v is the specific heat for a constant volume , dT is an increment of temperature, L is the latent heat of liquefaction and dW represents the quantity of water that is liquefied (or vaporised).

If we assume an adiabatic equilibrium ($\delta Q = 0$) and dry air ($LdW = 0$) we can deduce

$$\frac{dT}{dz} = -\frac{g}{c_p}$$

where c_p is the specific heat for a constant pressure par mass unit. When we integrate this law, we obtain

$$T(z) - T_0 = -\alpha(z - z_0)$$

where $\alpha = \frac{g}{c_p}$ is the temperature lapse rate. If the air is wet, the temperature lapse rate becomes lower but the linear law remains correct. This law is generally valid but it happens that the adiabatic equilibrium is not respected and in this case temperature inversions can occur.

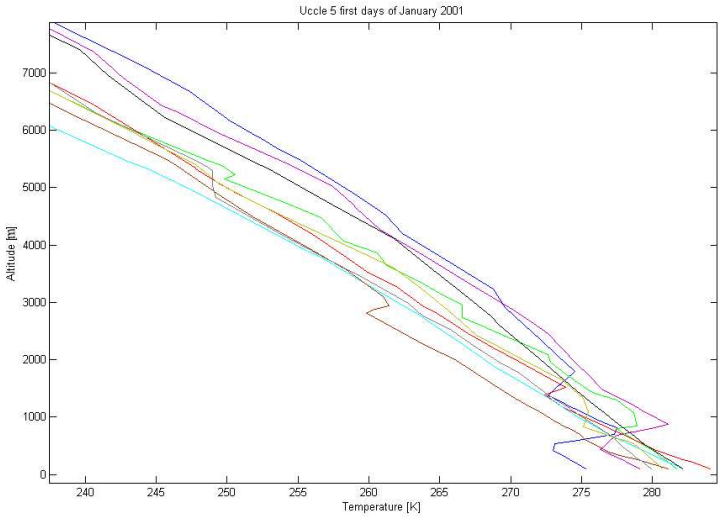

Figure 2.2: Graphs of the temperature as a function of the altitude for the five first days of January 2001 in Uccle. These curves have been generated from radiosonde measurements.

2.1.1.1 Hopfield's model

In 1969, Hellen Hopfield proposed a first model for the tropospheric delay. To be precise, her first paper [21] was more oriented on the Doppler effect correction than on the delay, but the principles were there. In a second paper, in 1971 [22], she focused on the delay corrections and provided improvements to her model. This model is still currently in use, for example in the GSSF[3] simulations, because of its simplicity. She assumed that the refractivity was only formed by two terms, one for the hydrostatic part and one for the wet part:

$$N_d = 77,6\frac{P}{T} \text{ and } N_w = 77,6\frac{4810e}{T^2} = 373256\frac{e}{T^2}$$

where P in the total pressure in hPa, T is the temperature in K and e is the water vapor pressure in hPa. In her paper, the word "dry" and the index d refer in fact to the hydrostatic part of the refractivity. Starting from the hypothesis of a linear diminution of the temperature as a function of the height$T = T_0 - \alpha h$ and that g can be considered as constant, the hydrostatic equilibrium gives:

$$P = P_0 \exp\left(-\frac{g}{R}\int_0^h \frac{dh}{T}\right)$$

[3]GSSF is a simulation facility used to simulate the behaviour of the Galileo system in case of dysfunctions of some elements (see Chapter 1).

$$= P_0 \left(\frac{T_0 - \alpha h}{T_0} \right)^{\frac{g}{R\alpha}}$$

which leads to

$$N_d = N_{0d} \left[\frac{\left(\frac{T_0}{\alpha}\right) - h}{\left(\frac{T_0}{\alpha}\right)} \right]^{\mu}$$

where $\mu = \frac{g}{R\alpha} - 1$ and $N_{0d} = 77,6P_0/T_0$ is the surface refractivity. This formulation puts $\frac{T_0}{\alpha}$ in evidence, which is in fact the virtual altitude at which the temperature would be null if the temperature lapse rate was constant up to the top of the atmosphere. By integrating this term we obtain

$$\int_0^{T_0/\alpha} N_d dh = \frac{N_{0d}(T_0/\alpha)}{\mu + 1} = \frac{77,6P_0R}{g} \tag{2.1}$$

If we derive the refractivity

$$\left(\frac{dN_d}{dh} \right)_{h=0} = -\frac{N_{0d}g}{RT_0} \left(1 - \frac{R\alpha}{g} \right)$$

The purpose of the author was to find a value of μ so that both the delay and the slope of the refractivity at the surface are correctly approximated. She found that the best value for μ was 4, so that the refractivity can be expressed as:

$$\begin{aligned} N_d &= k_d \left(h_d - h\right)^4 \quad h \leq h_d \\ &= \frac{N_{Td}}{\left(h_d - h_T\right)^4} \left(h_d - h\right)^4 \end{aligned}$$

where h_{0d} is the equivalent height of the atmosphere, h_T the height of the station, h the actual height and N_{0d} is the surface refractivity for dry air.

The zenith delay then becomes equal to:

$$\begin{aligned} \int_{h_s}^{h_d} N_d \, dh &= 0,2.10^{-6}.N_{0d}(h_d - h_s) \\ &= 0,2.10^{-6}.77,6\frac{P_0}{T_0}(h_d - h_s) \end{aligned} \tag{2.2}$$

In the 1969 paper, the equivalent height of the atmosphere was calculated stating a maximal value at the equator and a sinusoidal decreasing when going to the poles:

$$h_d = h_{d(eq)} + A_d \sin^2 \varphi_T$$

where A_d is the the difference of the atmospheric virtual upper limit between the poles and the equator ($A_d < 0$) and φ_T is the latitude of the station. Realising

that the equatorial bulge was a consequence of hotter atmospheric temperatures rather than a consequence of centrifugal forces, she proposed in her second article another way to derive the equivalent height of the atmosphere using the ground temperature. As the expression (2.1) has to be equal to the expression (2.2), it is obvious the the h_d parameter should be a linear function of the surface temperature:

$$h_d = h_{0d} + a_d T_c$$

where h_{0d} is the value of h_d at 0°C and a_d a coefficient describing the relationship between h_d and T_C. To determine this constants, she used radiosonde measurements all over the word and deduced $h_{0d} = 40,082$ km and $a_d = 0,14898$ km/°C.

For the wet refractivity, even if there is no physical reasons to do this, a similar refractivity profile is postulated so we obtain the same formulation:

$$\begin{aligned} N_w &= k_w \left(h_{0w} - h\right)^4 \quad h \leq h_{0w} \\ &= \frac{N_{Tw}}{\left(h_{0w} - h_T\right)^4} \left(h_{0w} - h\right)^4 \end{aligned}$$

By vertically integrating this equation, we obtain:

$$\begin{aligned} \int_{h_s}^{h_d} N_w \, dh &= 0,2.10^{-6}.N_{0w}(h_w - h_s) \\ &= 0,2.10^{-6}.373256\frac{e}{T^2}(h_w - h_s) \end{aligned}$$

2.1.1.2 Black's model

Harold Black's model (see details in [8]) is a model derived from the Hopfield model and like the former one, it neglects the bending. It uses the quartic profiles proposed by his predecessor, but makes other assumptions for the integration. From

$$\Delta L = 10^{-6} \int_0^{\rho} N_d + N_w d\rho$$

where $\rho = \left(r^2 - {r_s}^2 \cos^2 E\right)^{1/2} - r_s \sin E$ is the geometrical path, Black deduced:

$$\Delta L_d = 10^{-6} N_{ds} h_d \int_0^1 l^4 \left(1 - \left(\frac{\cos E}{\left(1 + (1-l)\frac{h_d}{r_s}\right)}\right)^2\right)^{-\frac{1}{2}} dl$$

Remarking that $(1-l)\frac{h}{r_s}$ is significantly smaller than unity, Black proposed to replace it by a constant $l_c = 0,85$ chosen in such a way that the integral stayed quasi identical.

Following a proposition that Hopfield suggested in 1971, the upper limit of the atmosphere is calculated from a linear function of the surface temperature T_s(in Kelvin):

$$h_d = 148,98(T_s - 4,12)$$

For the wet part of the delay, Black stated that no physical laws could be applied to describe the water vapor distribution in the atmosphere so that he followed more or less the Hopfield's hypothesis for the part linked to the elevation angle, but the zenith delay should be chosen for a best fit to the measurements. In fact, the Black model is, in a way, only an hydrostatic delay model.

Knowing that $N_{ds} = 77,6\frac{P_S}{T}$, the model can finally be expressed as follows:

$$\Delta L = \Delta L_d + \Delta L_w$$

$$\Delta L_d = 2,343 P_s \left(\frac{T_s - 4,12}{T_s}\right) I(h = h_d, E)$$

$$\Delta L_w = k_w I(h = h_w, E)$$

$$I(h, E) = \left(1 - \left(\frac{\cos E}{\left(1 + (1 - l_c)\frac{h}{r_s}\right)}\right)^2\right)^{-\frac{1}{2}}$$

$$h_d = 148,98(T - 4,12)$$

2.1.1.3 Saastamoinen's model

This model was proposed by J. Saastamoinen in 1972 (see details in [41]). Starting from the equation (4.4) the integration variable is modified in order to express the electric path as a function of the altitude ($ds = \sec z \, dr$). The expression $\sec z$ is then approximated by

$$\sec z \approx \sec z_1 - \frac{1}{r_1}(\sec^3 z_1 - \sec z_1)(r - r_1)$$

and the integral becomes:

$$\Delta L = \sec z_1 \int_{r_1}^{r'} (n - 1) dr - \frac{\sec z_1 \tan^2 z_1}{r_1} \int_{r_1}^{r'} (n - 1)(r - r_1) dr$$

To calculate these integrals, Saastamoinen considered the air as the mixture of two ideal gas, dry air and water vapor.

He also assumed that the temperature profile can be written

$$T = T_1 + \alpha(r - r_1)$$

and that the temperature lapse rate $\alpha = \frac{dT}{dr}$ is constant in the troposphere and is equal to zero in the stratosphere. The refractivity formula is expressed as:

$$n - 1 = \frac{(n_0 - 1)T_0}{p_0}\left(\frac{p}{T}\right) - c_w\left(\frac{e}{T}\right) + c'_w\left(\frac{e}{T^2}\right)$$

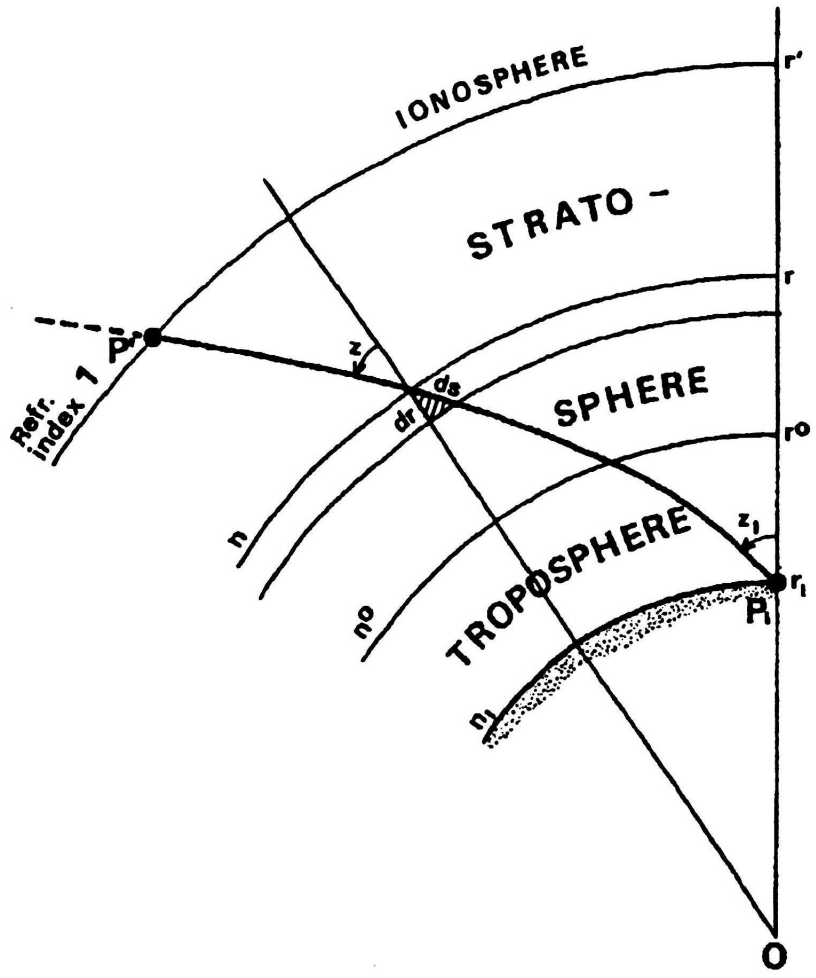

Figure 2.3: Schema of the electrical path of the signal in a spherical atmosphere. The notations in this paragraph are linked to this picture.

where n_0 is the refractive index of dry air at pressure p_0 and at temperature T_0 and c_w ans c'_w are constants. He took the equation and the values recommended by the *International Association of Geodesy*[4]

$$(n-1).10^6 = 77.624\left(\frac{p}{T}\right) - 12.92\left(\frac{e}{T}\right) + 371900\left(\frac{e}{T^2}\right)$$

In order to evaluate the integrals linked to water vapor pressure, Saastamoinen postulated the following relationship between e and the temperature:

$$e = e_1\left(\frac{T}{T_1}\right)^{\frac{-4g}{R\alpha}}$$

where g is the acceleration of gravity. As he stated that:

$$p = p_1\left(\frac{T}{T_1}\right)^{\frac{-g}{R\alpha}}$$

we can deduce that

$$e = e_1\left(\frac{P}{P_1}\right)^4$$

After calculations (see details in his paper), the tropospheric delay becomes:

$$\begin{aligned}\Delta L &= \frac{(n_0-1)RT_0}{p_0 g_m}p_1 \sec z_1 - \frac{(n_0-1)R^2T_0}{r_1 p_0 g_m^2}.\left[\frac{p_1T_1 - \left(\frac{R\alpha}{g_m}\right)p^0T^0}{1-\frac{R\alpha}{g_m}}\right]\sec z_1 \tan^2 z_1 \\ &+ \left[\frac{(n_0-1)RT_0}{4p_0g_m}\left(1-\frac{R}{R_w}\right) - \frac{Rc_w}{4g_m} + \left(\frac{c'_w}{\frac{4g_m}{R}+\alpha}\right)\frac{1}{T_1}\right]e_1 \sec z_1\end{aligned}$$

This formula is quite complex, it is composed of a term depending on p_1, a term depending on $\tan^2 z_1$, a term depending on e_1 and a term depending on $\frac{e_1}{T_1}$. Saastamoinen noticed that the second term of this equation was a correction due to the curvature of the atmosphere, so that it did not depend a lot on meteorological conditions but only on the altitude of the station so that the coefficient of the term in $\tan^2 z$ could be replaced by an average value.

We can re-arrange the terms in the following way:

$$\begin{aligned}\Delta L &= 10^{-6}\sec z_1 \frac{R_d}{g_m}\left(k_1p_1 - \frac{k_1R_d}{r_1g_m}.\left[\frac{p_1T_1 - \left(\frac{R\alpha}{g_m}\right)p^0T^0}{1-\frac{R\alpha}{g_m}}\right]\tan^2 z_1\right. \\ &\left. + \left[\frac{k'_2}{4} + \left(\frac{k_3}{4+\alpha R/g_m}\right)\frac{1}{T_1}\right]e_1\right)\end{aligned}$$

[4]Which are in fact the values from Essen and Froome. we will develop the discussion on the refractivity coefficient in a following section.

where $k_1 = (n_0 - 1)T_0/p_0$is the refractivity coefficient for dry air, $k_2' = k_2 - k_1 M_w/M_d$ (M_w and M_d are respectively the molar mass of water and dry air) and $k_3 = c_w'$.

He also made a useful assumption on the on the local gravity at the centroid of the atmospheric column:

$$\begin{aligned} g_m &= 98,07(1 - 0,0026\cos 2\Phi - 0,00031\bar{H}) \\ &= 97,84(1 - 0,0026\cos 2\Phi - 0,00028H) \end{aligned}$$

where $\bar{H}$ is the altitude of the center of gravity of the column of air. This value can be approximated by $\bar{H} = 7,3 + 0,9H$, H being the station height.

The final formula for practical computation given by Saastamoinen is the following one:

$$\Delta L = 0,002277 \sec z \left[p + (1255/T + 0,05)e - C\tan^2 z\right]$$

where C is tabulated in table (2.1).

In literature, the following equation for the zenith hydrostatic delay is often called the Saastamoinen model:

$$\Delta L_h = 10^{-6}\frac{k_1 R_d}{g}p$$

This is a little bit unfair to Hopfield who found this formulation before. Nevertheless, in the following of this text, we called it the Saastamoinen formula to be coherent with the other authors.

Height above sea level [km]	Coefficient C
0	1,16
0,2	1,13
0,4	1,10
0,6	1,07
0,8	1,04
1	1,01
1,5	0,94
2	0,88
2,5	0,82
3	0,76
4	0,66
5	0,57
6	0,49

Table 2.1: Coefficient $C = \frac{R}{r_1 g}\left[\frac{p_1 T_1 - (R\beta/g)p^\circ T^\circ}{1 - R\beta/g}\right]$

2.1.1.4 Askne and Nordius 2 parameters model

This model (see details in [3]) is a very interesting one even if it requires more information about the atmosphere than only ground measurements[5] because it is a precursor to the blind models that are currently used. Oppositely to the previous models this formulation is only correct for the zenith delay. To extend the equation to elevation angles different from 90° it is necessary to use mapping functions.

For the hydrostatic part of the delay, the formulation is identical to the Saastamoinen one and only depends on the surface pressure and the receiver height and latitude.

As far as the wet delay is concerned, Askne and Nordius adopted a different point of view then their predecessor. Where this last one stated a relationship between the water vapor pressure profile and the temperature profile, the two Swedish authors started from a formula linking the mixing ratio profile and the pressure profile (the subscript s stands for surface):

$$w = w_s(p/p_s)^{\lambda}$$

and with the mixing ratio defined as:

$$w = \frac{M_w}{M_d}.\frac{e}{p}$$

so that they obtained

$$e = e_s \left(\frac{p}{p_s}\right)^{\lambda+1}$$

They then defined the mean temperature of the column of air as

$$T_m = \frac{\int_H^\infty \frac{e}{T}\,dz}{\int_H^\infty \frac{e}{T^2}\,dz} \tag{2.3}$$

so, that the wet delay can be expressed as

$$\Delta L_w = 10^{-6}\left(k_2' + \frac{k_3}{T_m}\right)\int_H^\infty \frac{e}{T}\,dz$$

The remaining problem was the estimation of T_m. Askne and Nordius found a way to express the mean temperature as a function of the ground temperature, the temperature lapse rate and the mixing ration lapse rate. Using an approximation of the hydrostatic equation

$$\frac{p}{T}\,dz = -\frac{R_d}{g}\,dp$$

[5] That is the reason why this model is rarely (if ever) used in practical situations.

, postulating a constant temperature lapse rate $T = T_s - \alpha(z - H)$ and introducing it into the hydrostatic equation they obtained after integration:

$$T = T_s \left(\frac{p}{p_s} \right)^{\frac{\alpha R_d}{g_m}}$$

Then if this equation replaces T in equation (2.3) the result is:

$$T_m = T_s \left(1 - \frac{\alpha R_d}{(\lambda + 1) g_m} \right)$$

Replacing the mean temperature with this last expression, Askne and Nordius's model is:

$$\Delta L = 10^{-6} \frac{k_1 R_d}{g_m} \left(p_s + e_s \left(\frac{k_2'}{k_1(\lambda + 1)} + \frac{k_3}{k_1(\lambda + 1 - \alpha \frac{R_d}{g_m}) T_s} \right) \right)$$

2.1.2 Blind models

In fact blind models do not really differ from the ground based models, the main difference is that the input information does not come from measurements but from tabulated coefficients. These coefficients replacing actual measurement are composed of a mean value corrected with a sinusoidal term simulating seasonal or diurnal fluctuations.

2.1.2.1 RTCA-MOPS

The RTCA-Mops model [39] is the model currently used for the GPS receivers. The parameters taken into account are the total pressure P [hPa], the temperature T [K], the water vapor pressure e [hPa], the temperature lapse rate α [K/m] and the water vapor mixing ratio lapse rate λ. For each parameter a mean annual value and a maximum seasonal variation are given for 5 latitudes belts (15, 30, 45, 60 and 75 degrees). The numbers are the same for the northern and the southern hemispheres.

The equations determining each of these parameters have the same form which is the following one:

$$\xi(\phi, D) = \xi_0(\phi) - \Delta\xi(\phi). \cos \left(\frac{2\pi \, (D - D_{min})}{365.25} \right)$$

where $\xi_0(\phi)$ and $\Delta\xi$ are respectively the mean and the maximal variation of ξ at latitude ϕ, D is the day of the year (1 is the first of January) and D_{min} is the day of the minimum ($D_{min} = 28$ in the northern hemisphere and $D_{min} = 211$ in

Average					
Latitude (°)	P_0 (mbar)	T_0 (K)	e_0 (mbar)	α_0 (K/m)	λ_0
15° or less	1013.25	299.65	26.31	6.30e-3	2.77
30°	1017.25	294.15	21.79	6.05e-3	3.15
45°	1015.75	283.15	11.66	5.58e-3	2.57
60°	1011.75	272.15	6.78	5.39e-3	1.81
75° or greater	1013.00	263.65	4.11	4.53e-3	1.55
Seasonal variation					
Latitude (°)	ΔP (mbar)	ΔT (K)	Δe (mbar)	$\Delta\alpha$ (K/m)	$\Delta\lambda$
15° or less	0.00	0.00	0.00	0.00e-3	0.00
30°	-3.75	7.00	8.85	0.25e-3	0.33
45°	-2.25	11.00	7.24	0.32e-3	0.46
60°	-1.75	15.00	5.36	0.81e-3	0.74
75° or greater	-0.50	14.50	3.39	0.62e-3	0.30

Table 2.2: Meteorological parameters for the RTCA-MOPS blind model (from [39]).

the southern hemisphere). The means and the maximal variations at a latitude ϕ ($15^\circ < \phi_i < \phi < \phi_{i+1} < 75^\circ$) are linearly interpolated according to the formulae

$$\xi_0(\phi) = \xi_0(\phi_i) + \left[\xi_0\left(\phi_{i-1}\right) - \xi_0\left(\phi_i\right)\right] \frac{(\phi - \phi_i)}{(\phi_{i+1} - \phi_i)}$$

$$\Delta\xi(\phi) = \Delta\xi(\phi_i) + \left[\Delta\xi\left(\phi_{i-1}\right) - \Delta\xi\left(\phi_i\right)\right] \frac{(\phi - \phi_i)}{(\phi_{i+1} - \phi_i)}$$

If $\phi < 15^\circ$ then $\xi_0(\phi) = \xi(15^\circ)$ and $\Delta\xi(\phi) = \Delta\xi(15^\circ)$. Alternatively if $\phi > 75^\circ$ then $\xi_0(\phi) = \xi(75^\circ)$ and $\Delta\xi(\phi) = \Delta\xi(75^\circ)$.

The implemented values of the parameters are compiled in table (2.2).

The zenith hydrostatic delay at sea level (in meters) is expressed as

$$z_{hyd} = \frac{10^{-6} k_1 R_d P}{g_m}$$

where $k_1 = 77,604$ K/mbar, $R_d = 287,054$ J/kg/K, P is the pressure in mbar and $g_m = 9,784$ m/s^2. The zenith wet delay is

$$z_{wet} = \frac{10^{-6} k_2 R_d}{g_m(\lambda + 1) - \alpha R_d} . \frac{e}{T}$$

At a height H (in meters) above sea level, the delays become:

$$d_{hyd} = \left(1 - \frac{\alpha H}{T}\right)^{\frac{g}{R_d \alpha}} .z_{hyd}$$

$$d_{wet} = \left(1 - \frac{\alpha H}{T}\right)^{\frac{(\lambda+1)g}{R_d \alpha}-1} .z_{wet}$$

with $g = 9,80665$ m/s^2 is the acceleration of the gravity.

The mapping function for an elevation angle E used in this model is

$$m(E) = \frac{1,001}{\sqrt{0.002001 + \sin^2(E)}}$$

This equation is considered valid as soon as the angle is not lower than 5 degrees.

2.1.2.2 UNIFAF/ESA

As usual, the zenith delay is expressed as the sum of an hydrostatic delay and a wet delay:

$$\Delta L = \Delta L_h + \Delta L_w$$

The hydrostatic delay has the same form as Saastamoinen's or Askne and Nordius's models:

$$\Delta L_h = 10^{-6} \frac{k_1 R_d}{g_m} p_s$$

The wet delay has also a form that is very close to the Askne and Nordius's delay, but neglecting the k_2 part:

$$\Delta L_w = 10^{-6} \frac{R_d}{g_m} . \frac{k_3}{(\lambda + 1)} . \frac{e_s}{T_{ms}}$$

As in the RTCA model, an harmonic seasonal fluctuation is assumed for the ground pressure, the mean temperature of the water vapor above the surface, the mean temperature lapse rate, the water vapor pressure at surface and the vapor pressure decrease factor:

$$X_i(D_y) = a1_i - a2_i \cos\left(2\pi \frac{D_y - a3_i}{365,25}\right)$$

where $a1_i$ is the average value of the parameter, $a2_i$ is the seasonal fluctuation of the parameter, $a3_i$ is the day of the minimum value of the parameter and D_y is the day of the year.

Contrarily to his predecessor, the ESA model takes also into account diurnal variations for the mean temperature of the water vapor above the surface, the water vapor pressure at surface and the vapor pressure decrease factor. The equation describing these parameters becomes:

$$X_i(D_y, H_y) = a1_i - a2_i \cos\left(2\pi \frac{D_y - a3_i}{365,25}\right) - b2_i(D_y) \cos\left(2\pi \frac{H_d - b3_i(D_y)}{24}\right)$$

where H_y is the hour of the day, $b2_i$ is the daily fluctuation of the parameter and $b3_i$ is the hour of the minimum value of the parameter.

The parameters introduced in the tables were calculated from numerical weather prediction maps issued from the ECMWF ERA 15 re-analysis [10] of the meteorological measurements.

2.1.3 Tropospheric delay estimations based on vertical distribution models

In the previous models, we made the assumption that the vertical profile of the atmosphere can be estimated only thanks to variables available from the surface, which introduces of course imprecision when the profile is not as regular as expected, for example at the proximity of a front.

The other way to calculate the tropospheric delay would be to precisely know the vertical profile so that it would be possible to perform the integration without any assumption on atmospheric behaviour.

The first method would be to measure directly with a radiosonde the vertical profile of the atmosphere. Radiosondes are balloons filled with helium (or hydrogen) lifting a little meteorological station. The carried sensors measure total pressure, relative humidity and temperature. These data are directly sent by a radio transmitter. By tracking the position of the balloon, meteorologists can also deduce information on the speed and the direction of the wind but this information is not relevant in our case. Because of the prize of each radiosonde and taking into account the fact that only 20% of the packages are recuperated, usually only 2 launches are performed per station and per day (sometimes it can go up to 4 launches).

Another possible method to get through this problem would be to use the data diffused by the meteorological institutes describing the totality of the atmosphere: the Numerical Weather Prediction (NWP) data sets. The problem is that the grids are very large (1 degree by 1 degree which is equivalent to more or less 100km by 100km) and that they are provided only every 6 hours while the phenomena related to the wet delay have a characteristic length of 40 km and a characteristic duration of 30 minutes.

Nevertheless, these meteorological grids are very useful to statistically calculate the coefficients used in the blind models. They can also be used to validate the model at an earth level.

2.1.4 Direct measurements of the delay

There also exist two more direct ways to measure the tropospheric delay:

- the Water Vapor Radiometers (WVR) which allows the measurement of the water vapor contend and thus we can deduce the tropospheric wet delay.
- the GPS ground stations, which deduce the total tropospheric delay from stochastic filtering of GPS data.

2.1.4.1 Water vapor radiometers

Water vapor radiometer are ground based upward looking microwave radiometers operating at least at two frequencies. One is centered around the 22 GHz water vapor rotational line and one is located typically around 31 GHz. The technique consists measuring the sky brightness temperature in both channels. This "sky noise" temperature and the frequency dependence of the background microwave radiations give us information on the Integrated Water Vapor (IWV) content and on the Integrated Liquid Water (ILW) content of the atmosphere. As the IWV content and the wet tropospheric delay are directly related, we can deduce this one with a good accuracy (around 20 mm). The other advantage is the temporal resolution of the measurements. The drawbacks are its complexity and the need of frequent calibrations.

2.1.4.2 GPS

The second technique requires the use of precise GPS dual frequency receivers. Assuming that the delay is constant over a short period of time and the azimuthal symmetry of the atmosphere, the delay can be computed from its elevation dependence by means of stochastic filtering. The precision of this method is even slightly better than the radiometers'one (only 15 mm).

2.2 Mapping functions

We have seen in the previous descriptions of the models that some of them were designed to directly take the elevation angle (E) into account. Some others only model the zenith delay, so that a mapping function is needed if the satellite is not located at zenith, so we have:

$$\Delta L(E) = m_h(E)\Delta L_{h\,zenith} + m_w(E)\Delta L_{w\,zenith}$$

For the RTCA model, we have seen that the wet and the hydrostatic mapping functions were the same. Nevertheless, a higher precision is needed for Galileo, so we have to consider different mapping functions for the hydrostatic and the wet parts.

Most of these mapping functions use atmospheric parameters like total pressure, water vapor pressure, temperature, the temperature lapse rate or the height of the troposphere. In 1996, A.E. Niell [33] has proposed a set of mapping functions that were only height, time (day of the year) and latitude dependent. Similarly to the "blind" models for the delay, these two mapping functions do not use the current meteorological measurements but tabulated parameters. Additionally, he showed by means of radiosonde measurements and ray-tracing algorithms that his equations have equivalent or better performances than the ones related to surface meteorology.

The equation of both mapping functions is the same but the parameters a, b and c are different:

$$m(E,a,b,c) = \frac{1+\frac{a}{1+\frac{b}{1+c}}}{\sin E + \frac{a}{\sin E+\frac{b}{\sin E+c}}} \tag{2.4}$$

As far as the hydrostatic mapping function is concerned, the parameters a, b and c depend on latitude and are subjected to seasonal fluctuations:

$$X_{hi}(D_y) = X_{m\,hi} - X_{f\,hi}\cos\left[2\pi\frac{(D_y - D_o)}{365,25}\right]$$

where $X_{m\,hi}$ and $X_{f\,hi}$ are the average values and the seasonal fluctuation of the parameters a, b and c for the hydrostatic part (these values are tabulated), D_y is the day of the year and D_o is the day of the minimum of the year, respectively 28 and 211 for the northern and the southern hemispheres. This corresponds to the correction at mean sea level; in order to take the height into account, we have to use

$$m_h(E,h) = m_h(E) + \Delta m_h(E,h)$$

where

$$\Delta m_h(E,h) = \left[\frac{1}{\sin E} - m(E,ch_1,ch_2,ch_3)\right]$$

where h is the height above sea level (in km), ch_1 ch_2 and ch_3 are height correction coefficients (tabulated) and m is the mapping function as calculated in equation (2.4).

The coefficients of the wet mapping function are not subjected to seasonal fluctuation nor to height corrections but only depend on the latitude of the considered point. According to this latitude, the values of a, b and c are extracted from a table.

The performances of this set of mapping function are totally satisfying to the requested accuracy and are not discussed anymore in the Galileo project.

In some applications like in VLBI, very low elevation angles are sometimes used (in the order of 5°), additional refinements of the mapping functions are needed. An assumption is hidden in Niell's mapping functions: the azimuthal homogeneity. Some models have been developed in order to take azimuthal asymmetries in the atmospheric refractive index (see the papers from MacMillan [27] or from Bar-Sever & Kroger [4]). The tropospheric delay usually takes the following form:

$$\begin{aligned} \Delta L &= m_h(E)\Delta L_{h\,zenith} + m_w(E)\Delta L_{w\,zenith} \\ &\quad + m_\Delta(E)\,\cot E\,(G_N\cos\phi + G_E\sin\phi) \end{aligned}$$

where ϕ is the azimuthal angle, G_N and G_E are respectively the north and the east values of the gradient vector and $m_\Delta(E)$ is the mapping function that gives the dependence of the delay on E.

2.3 Refractivity coefficients

One of the most problematic issues in modeling the tropospheric delay is the value of the coefficients used in the evaluation of the refractivity. In this section we will chronologically expose the various proposed values for the refractivity coefficients. Afterwards we will discuss these values.

2.3.1 Smith and Weintraub

We will begin the review with the values proposed by Smith and Weintraub in 1953 [42]. We chose to begin with this paper even if there were older propositions because it gives evidence of a real improvement in the accuracy, and it is often mentioned as a reference by many more recent authors. They adopted the following form for refractivity:

$$N = K_1\frac{p_d}{T} + K_2\frac{e}{T} + K_3\frac{e}{T^2} \tag{2.5}$$

Their calculation of the K_1 parameter is based on three previously measured values for the dielectric constant of dry air[6] at different wavelengths. As these measurements for dry air were made without CO_2 and considering ideal gas, they corrected the values (assuming an average CO_2 concentration of 300 ppm) and then evaluated the mean dielectric constant. This parameter leads directly to the refractive index thanks to the formula $n = \sqrt{\mu\epsilon}$ (considering $\mu = 1$). Then they

[6]The values they refer to are from Barell (1951) in the optical range and from Birnbaum, Kryder and Lyons (1951) and Essen and Froome (1951) in the microwave range.

deduced K_1 from the knowledge of the dry air pressure and the temperature, since $N = K_1 p_d/T$. The result is:

$$K_1 = 77,607 \pm 0,013 \frac{K}{mb}$$

For the K_2 and K_3 parameters, they assumed an ideal gas behaviour for water vapor. They justified this hypothesis by explaining that, in the atmosphere, its partial pressure is very low so that the difference between a realistic gas and a perfect gas is negligible. For their calculation, they leaned on the evaluations of the Debye constants from Birnbaum and Chatterjee. This leads to:

$$\begin{aligned} K_2 &= 71,6 \pm 8,5 \frac{K}{mb} \\ K_3 &= (3,747 \pm 0,031) 10^5 \frac{K^2}{mb} \end{aligned}$$

2.3.2 Thayer

Needing a higher accuracy, Thayer [46] proposed in 1974 new refractivity coefficients. Instead of taking directly the correction to the perfect gas law in the K_1 coefficient, Thayer preferred to add the inverse compressibility directly in the formula:

$$N = k_1 \frac{p_d}{T} Z^{-1} + k_2 \frac{e}{T} Z_w^{-1} + k_3 \frac{e}{T^2} Z_w^{-1}$$

Then his conclusions were based on more recent laboratory measurements in both optical and radio domains. As the precision of optical values was superior to the radio ones, he used interrelationships between radio and optical refractivities. He noted that, theoretically, the dielectric constant for the non-dipolar terms should be the same, and that it is not the case for the dipolar term. The reason is that natural frequencies of the water molecule dipole moment are below the optical frequency domain but far above the radio one. This explains why in the optical range, k_3 is equal to zero and why in the radio range k_3 is independent from the frequency.

He showed that we could extrapolate k_1 and k_2 coefficients from optical measurements if the magnetic permeability is corrected and if the appropriate dispersion formula is used. As far as the k_1 coefficient was concerned, he concluded that direct measurements in the radio domain were more accurate anyway. It is nevertheless noticeable that the "radio" value he chose came in fact from the Smith and Weintraub, and consequently was partly "optical".

He also remarked that the problem was more complex for k_2 and k_3, because the measured wet refractivity[7] is $N_w = k_2\frac{e}{T} + k_3\frac{e}{T^2}$,so it is not easy to distinguish the first contribution from the second one. He compared the accuracy obtained from the two methods. The first one was a statistical method and is based on a reformulation of the wet refractivity:

$$N_w\frac{T}{e} = k_2 + k_3\frac{1}{T}$$

and on the least square fit of data from radio measurements made by Boudouris in 1963. The parameters deduced from the linear regression were $k_2 = 72,0 \pm 10,5$ and $k_3 = (3,754 \pm 0,030)10^5$.

The second technique consisted in deducing the k_3 coefficient from the k_2 value obtained thanks to optical measurements and from refractivity measurements in the radio range:

$$k_3 = \frac{N_w}{e}T^2 - k_2T$$

The final k_3 value is a weighted mean of the numbers calculated for different temperatures.

He noticed that the optical method gave a better precision and from his conclusions it results that

$$\begin{aligned} k_1 &= 77,60 \pm 0,014\frac{K}{mb} \\ k_2 &= 64,8 \pm 0,08\frac{K}{mb} \\ k_3 &= (3,776 \pm 0,004)10^5\frac{K^2}{mb} \end{aligned}$$

2.3.3 Hasegawa and Strokesberry

Saburo Hasegawa and Daniel Strokesberry were no specialists in refractivity but they did explain in their paper how they tested a new kind of hygrometers based on microwave measurements. Their technique consisted in a comparison of resonance frequencies in two cavities, one containing dry air and one containing moist air, so they needed to know as precisely as possible the refractivity coefficients. As their purpose was only to validate and calibrate their instrument, they gathered many measurements and calculated the mean, using the given error estimations as weighting coefficients. Looking at the tables of this article, we can observe that, as the error from Essen and Froome was very small, this set of measurements dominates all the others.

[7]For more concision, we will not take any more the inverse compressibility into account in the remaining part of the paragraph.

The proposed values are:

$$\begin{aligned} K_1 &= 77,600 \pm 0,032 \frac{K}{mb} \\ K_2 &= 69,400 \pm 0,146 \frac{K}{mb} \\ K_3 &= (3,701 \pm 0,003) 10^5 \frac{K^2}{mb} \end{aligned}$$

2.3.4 Hill

Hill, Laurence and Priestley chose the theoretical point of view rather then the experimental one. They studied the refractivity due to water vapor in the radio wavelength induced by resonances in the infrared spectrum. Their method consisted in summing all the resonance contributions coming from the vibrational and the vibrational-rotational transitions. The refraction index associated with each sharp line has the form:

$$n_i = \frac{S_i Q}{2\pi^2 {\nu_i}^2}$$

where S_i is the integrated absorption strength of the resonance, ν_i is its line frequency and Q the number of density of absorbing molecules. The result of their calculations is:

$$\begin{aligned} K_2 &= 98 \pm 1 \frac{K}{mb} \\ K_3 &= (3,583 \pm 0,003) 10^5 \frac{K^2}{mb} \end{aligned}$$

They criticised Thayer's hypothesis on the basis that K_2 should have the same value in the radio range as in the optical range. Theory in fact showed that IR resonance should have an impact on K_2, and their calculation resulted in a 33,3 K/hPa augmentation of this coefficient. They conclude that the values deduced from this assumption should not be used.

The problem in the values calculated by Hill & al. is that they do not match precisely enough the experimental values, even those coming exclusively from the microwave domain (i.e. Boudouris). They gave two possible explanations to this discrepancy. The first one was that there were some inaccuracies in the estimation of some S_i/ν_i parameters. The other possibility came from the fact that only monomer contribution of the water vapor has been considered but not the impact of water clusters.

In their appendix they discussed the average values obtained by Hasegawa and Strokesberry and pointed out the domination of the Essen & Froome's experimentation in their final values. As Essen & Froome only considered a short range of temperatures and pressure for their fittings and as they used K_2 values from

optical measurements, their results can not be as accurate as it was mentioned, and consequently Hasegawa & Strokesberry values have the same inaccuracies.

2.3.5 Bevis & al.

Revisiting the values of Hasegawa & Strokesberry (1975), Bevis & al. made an inventory of the available measurements for the three coefficients in 1994 and plotted them with their error in the annex of their paper. They mentioned the critics of Hill & al. on the too optimistic estimation of the error by Essen & Froome. Nevertheless Bevis & al. considered that they were not able to decide which value of the accuracy is correct. They provided a value obtained by weighting the different numbers according to the error attached to the measurements but, considering the remarks of Hill, they were very careful with these numbers.

As they do not trust on the given standard errors, and especially the error provided by Essen & Froome, they also provided an unweighted value and a related standard error which were preferred in their conclusions. The following values are still recommended nowadays:

$$\begin{aligned} K_1 &= 77,60 \pm 0,05 \frac{K}{mb} \\ K_2 &= 70,400 \pm 2,2 \frac{K}{mb} \\ K_3 &= (3,739 \pm 0,012) 10^5 \frac{K^2}{mb} \end{aligned}$$

We can notice that the values of the uncertainties are higher then those given by Hasegawa and Strokesberry.

2.3.6 Rüger

Remarking that the interest for applications needing precise refractivity coefficient (VLBI, microwave EDM[8] and GNSS) was growing, the *International Association of Geodesy* (IAG) decided in 1991 to prepare a new resolution on refractive indexes. Effectively, the only resolution of the IUGG (*International Union of Geodesy and Geophysics*, a branch of which the IAG is) dated from 1963 and has almost never been applied because it was based on Essen and Froome measurements from 1951, and more recent measurements were usually chosen. The old adopted formula was

$$N_r = 77,624 \frac{p_d}{T} + 64,700 \frac{p_w}{T} + 371897 \frac{p_w}{T^2}$$

[8]Electronic Distance Measurement

Leading the Ad-Hoc IUGG party charged to update the formula, Rüger made a review of all the values available and criticised the successive proposed values. He pointed out the use of too limited range of pressure and temperature of Essen and Froome and the introduction of optical measurements in microwave values (Essen and Froome, Smith and Weintraub, Thayer,etc.). He also noticed that Hasegawa & Stokesberry and Bevis & al. in their review did not take into account the high correlation between k_2 and k_3 for the estimation of the error but had only computed independent means.

He also mentioned Mendes's PhD dissertation and his considerations on the impact of the refractivity formulae on the zenith delay. Mendes calculated that the omission of compressibility would lead to an error of maximum 0,2 mm on the wet delay, which is negligible. He also demonstrated that the formula adopted for the saturation water pressure could also be a source of errors: this could lead to a difference of delay of approximately 3 mm.

After this complete review of the available data Rüger proposed to update the values of the k_1 coefficient according to the augmentation of the CO_2 concentration in the atmosphere. Actually, the carbon dioxide atmospheric contend has increased from 300 ppm in 1960 to 375 ppm in 2004.

He then adopted three different strategies to obtain new coefficients. His first choice was to select the best available values according to the previous considerations. Starting from

$$N_r = K_1' \frac{p_{d-c}}{T} + K_2 \frac{p_w}{T} + K_3 \frac{p_w}{T^2} + K_4 \frac{p_c}{T}$$

where p_{d-c} is the partial pressure of dry air without taking the carbon dioxide into account, p_w is the water vapor pressure and p_c is the partial pressure of the carbon dioxide. He selected the values given by Boudouris in 1963 for K_2 and K_3 and the work from Newel and Baird (1965) to derive K_1' and K_4. This results in

$$\begin{aligned} K_1' &= 77,674 \pm 0,013 \\ K_1(300ppm) &= 77,691 \pm 0,013 \\ K_1(375ppm) &= 77,695 \pm 0,013 \\ K_2 &= 71,97 \pm 10,5 \\ K_3 &= 375406 \pm 3000 \\ K_4 &= 133,484 \pm 0,022 \end{aligned}$$

His second option was to adopt the best average values from independent experiments in order to avoid systematic errors, averaging the measurements in function of the previous remarks about methodological mistakes. His recalculations lead to the following numbers:

$$K_1' = 77,6681 \pm 0,0094$$

$$
\begin{aligned}
K_1(300ppm) &= 77,6848 \pm 0,0094 \\
K_1(375ppm) &= 77,6890 \pm 0,0094 \\
K_2 &= 71,2952 \pm 1,3 \\
K_3 &= 375463 \pm 760 \\
K_4 &= 133,4800
\end{aligned}
$$

Here Rüger did not give the error for each coefficient but provided a conservative overall accuracies of 0,02% of N_d for the dry refractivity and 0,20% of N_d for the dry refractivity. The values of the errors given here come from Mendes[31].

His third option consisted in adopting the theoretical point of view, so he used the Liebe's Millimeter Propagation Model (MPM) algorithm to calculate refractivity. Liebe's computer program calculates complex refractive index for frequencies from 1 Hz up to 1 THz from 44 oxygen and 30 local water resonance lines, from non resonant spectra for dry air and from an empirical water vapour continuum. This algorithm has been tested in many laboratories and has been improved and refined with time so that it is considered as reference by many scientists. Rüger also mentioned two other algorithms on preparation; Hill's IR_N and Prado & al., but the first one seems very difficult to use and the second one is not finished yet.

At the end of his paper, his main message was that we should not use the Essen & Froome nor the Thayer values anymore. On the other hand Rüger does not conclude on the best of the three approaches that he presented.

2.3.7 Conclusions

Smith & Weintraub and Tayer's coefficient set is one of the first relatively reliable coefficient set available, but they are burden with errors due to the use of optical values for the calculation of the k parameters. Hasegawa & Strokesberry's approach is interesting, but they did not realise that their analysis was dominated by questionable coefficients.

Hill & al. pointed out misleading assumptions in the previous works, but their theoretical method did not give more convincing results.

The choices of Bevis & al. to keep Essen & Froome values in their mean seem a little bit surprising, since they were informed of Hill's critics. It is probable that we should understand Bevis & al.'s position in this way: the fact that the standard errors of Essen and Froome were excessively small, because they came from optical measurements does not mean that the values coming from microwave measurements were less sensible to experimental errors and were necessarily more reliable. Nevertheless our opinion is that it was an error and that these values should have been discarded.

Rüger is the author who has taken into account the greatest number of errors sources (the increase of CO_2 in the atmosphere for example) . The problem with

Rüger's paper is that he does not provide any clear recommendation. This lets us in front of three possibilities: should the coefficient be chosen on the base of the best experience, with a strong risk of methodological error, should we chose the coefficient according to theoretical considerations, even if it does not match exactly to the experimental values or should we average the available values, even if we know that some of them are contestable?

Our opinion is that the theoretical approach has not given entirely satisfying results for the time being. The discrepancies from experiments are still too large to trust these numbers blindly as long as we do not exactly know the origin of the differences. Water is a very particular molecule and many phenomena related to its behavior are still misunderstood. We should also keep in mind that MPM93 is the only reliable and usable program available; it would be better to consider more then one algorithm in order to validate the approach.

On the other hand, relying on a single experience to derive the parameters is too dangerous. IUGG made this choice in 1963, relying essentially on Essen and Froome's values with the consequences that were exposed above.

The only remaining acceptable choice seems to be the mean values. But, in this calculation, we should discard values which are issued from wrong assumptions.

As we do not have into any additional and decisive experiment available, we think that Rüger's considerations on the "Best average" values are the most complete ones and that we can consider them as the best values available.

2.3.8 Sensibility analysis on the refractivity coefficients

An interesting issue in the delay determination is the influence of the choice of the k_1 and k_3 coefficients on the delay calculated thanks to the ESA/UNIFAF blind model. The purpose was to check if the precise knowledge of the correct coefficients was really an important issue in the validation of the models. We created an algorithm scanning the world map during one year and examining 12 hours per day. We could restrict the calculation to only a half year and half days because of the cosinusoidal nature of seasonal and daily fluctuations, but as the day (and the hour) of the minimum is not the same for each point, it is not easy to carry on this approach.

At this point of the work, we decided to take the Thayer values as a reference because these were the values evaluated in the GSTB-V1 tests. So, the results can be easily interpreted, as it answers to the question: "What is the difference in the zenith propagation delay if we use other values than Thayer's ones?".

The first set of values that we considered was the Bevis "weighted" ones because these numbers have been proposed to replace Thayer's ones at a certain moment during the project after GSTB-V1 tests. After Bevis's paper was reconsidered, the Bevis "unweighted" values were preferred and are the values that are actually taken in consideration in the actual form of the ESA blind model. The last parameter

Author	k_1 $\left[\frac{K}{mb}\right]$	k_2 $\left[\frac{K}{mb}\right]$	k_3 $\left[\frac{K^2}{mb}\right]$
Essen & Froome (1951)	$77,636 \pm 0,027$	$64,695 \pm 0,198$	371800 ± 400
Smith & Weintraub (1953)	$77,607 \pm 0,013$	$71,6 \pm 8,5$	$(374700 \pm 3100$
IUGG (1963)	$77,624$	$64,700$	371897
Boudouris (1963)	$77,64 \pm 0,08$	$71,98 \pm 10,82$	375400 ± 3600
Thayer (1974)(*)	$77,60 \pm 0,014$	$64,8 \pm 0,08$	377600 ± 400
Liebe (1977)	$77,676 \pm 0,023$	$71,631$	374656
Hill (1980)		98 ± 1	358300 ± 300
Bevis (unweighted) (1996)	$77,6 \pm 0,05$	$70,4 \pm 2,2$	373900 ± 1200
Bevis (weighted) (1996)		$69,4$	370100
Rueger (best available) (2002)	$77,695 \pm 0,013$	$71,97 \pm 10,5$	375406 ± 3000
Rueger (best average)(375ppm CO_2)	$77,6890 \pm 0,0094$	$71,2952 \pm 1,3$	375463 ± 760
Galileo Ref. Model	$77,6 \pm 0,05$	$70,4 \pm 2,2$	373900 ± 1200

Table 2.3: Review of k_i coefficients available in literature. The value with an (*) means that the inverse compressibility has not been taken into account.

set that we tested was the Rüger's one because it is the last set available and it was proposed by a specialist of the subject that has reviewed and discussed all the previous results. Also note that for this last set of values, not only the k_3 coefficient is sensibly different, but the k_1 takes into account a more realistic amount of CO_2 in the atmosphere.

	k_1	k_3
Thayer	$77,6$	377600
Bevis weighted	77,6	370100
Bevis unweighted	77,6	373900
Rueger	$77,6890$	375463

Table 2.4: Tested coefficients

The maps shown below are the the maps of the mean delay difference, of the RMS difference and the standard deviation for the total, hydrostatic and wet delays. The mean and the RMS maps show us that the maximal differences stand more or less at the level of the equator. This is logical because that zone is the most humid one, so that this is the region where the k_3 coefficient has the greatest influence.

The maps of the mean difference in the hydrostatic delay look like elevation maps of the world. This result is due to the fact that higher is a location, the lower is the surface total pressure, so the shorter is the delay. This is the reason why the differences of delay are also shorter at high altitudes.

k_1 values from Thayer, Bevis weighted and Bevis unweighted are the same, so that the difference in total delay comes only from the wet delay. Replacing Thayer's k_3 by Bevis weighted's one would lead to a maximal difference of 6 mm. If we decide to use Bevis unweighted coefficient, this would lead to a maximal difference of around 3 mm.

Rüger's set of coefficients also modifies the hydrostatic delay. The maximal difference for the hydrostatic part is around 1,6 mm. The maximal difference of wet delay is around 2,1 mm. As the mean difference in hydrostatic difference in hydrostatic and wet delays have opposite signs, the maximal difference of total delay is only around 2 mm. Contrarily to the two other sets we can see here that the difference would be essentially located in the highest latitude. To conclude we would say that the choice of the set of k coefficients induces very minor differences, but as long as we know that Rüger's "Best average" set of values is based on assumptions that are less wrong than the others, it should be used anyway.

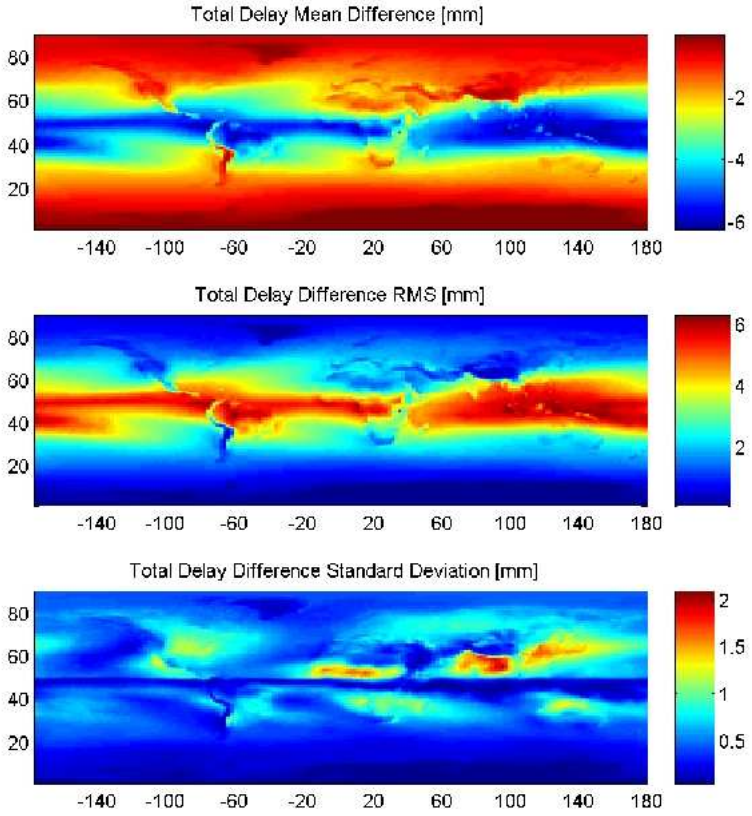

Figure 2.4: Maps of the differences of total delay between Thayer and Bevis "weighted". We can see the mean difference during one year, the RMS difference and the standard deviation. [The latitude and longitude labels are inverted].

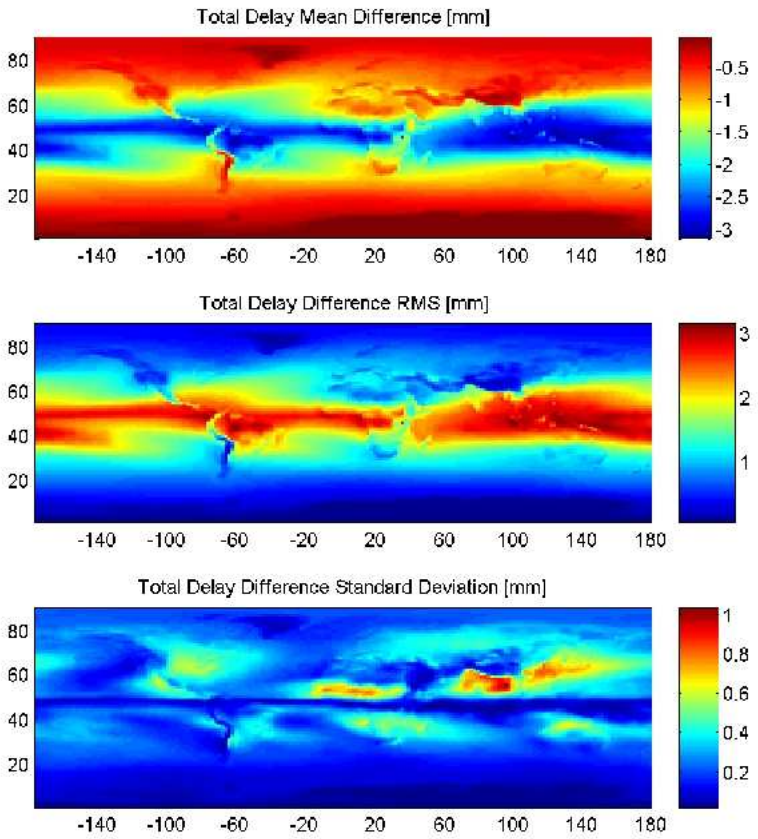

Figure 2.5: Maps of the differences of total delay between Thayer and Bevis "unweighted". We can see the mean difference during one year, the RMS difference and the standard deviation.

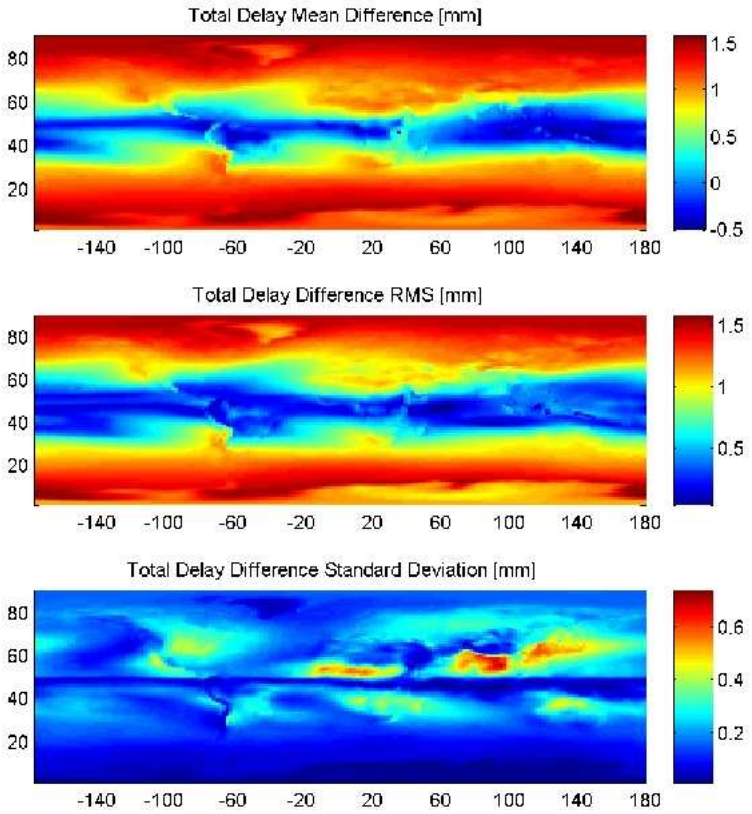

Figure 2.6: Maps of the differences of total delay between Thayer and Rueger. We can see the mean difference during one year, the RMS difference and the standard deviation.

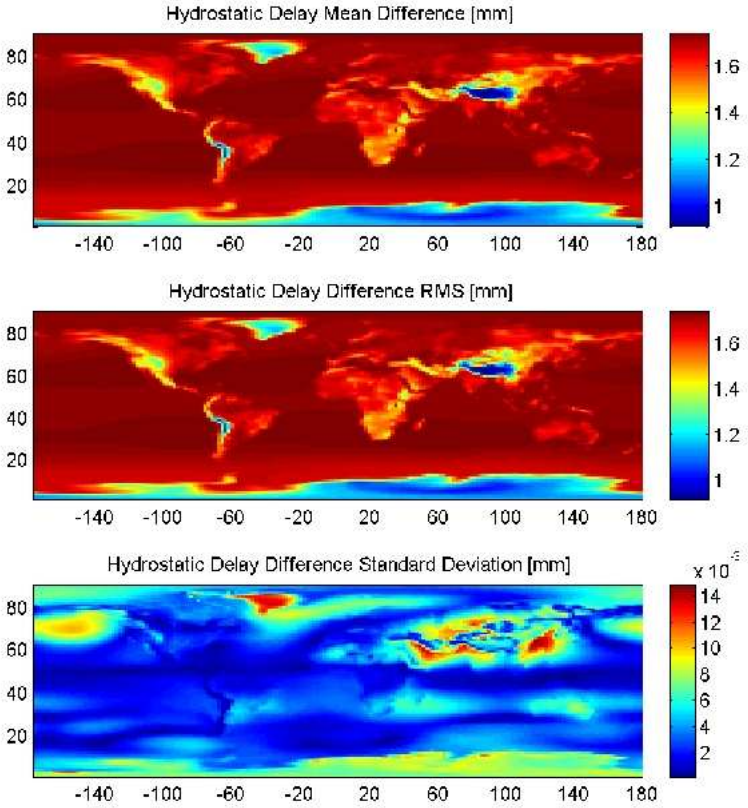

Figure 2.7: Maps of the differences of hydrostatic delay between Thayer and Rueger. We can see the mean difference during one year, the RMS difference and the standard deviation.

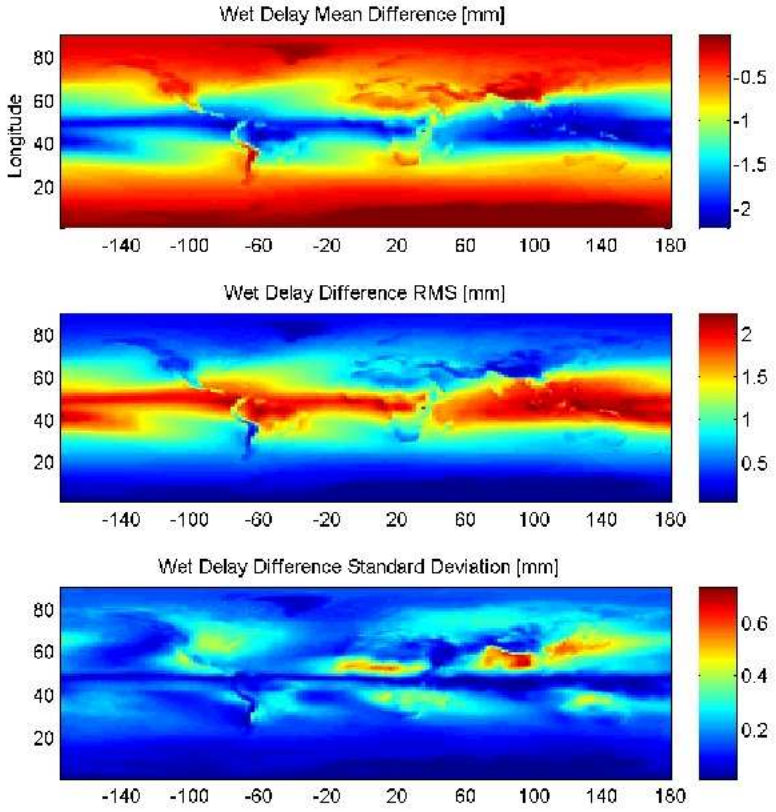

Figure 2.8: Maps of the differences of wet delay between Thayer and Rueger. We can see the mean difference during one year, the RMS difference and the standard deviation.

Chapter 3

Assessment of the models with radiosonde profiles

3.1 British Atmospheric Data Center (BADC) Global Radiosonde Data

Radiosondes are balloon-borne meteorological stations measuring pressure, temperature and humidity vertical profiles *in situ*. The wind speed and directions can also be deduced thanks to tracking high gain antennae providing elevation and azimuthal position. This is the main meteorological data source for tropospheric pressure, temperature and humidity profiles. Radiosondes are usually launched twice a day in meteorological stations all over the world.

Dealing for radiosonde profiles has several advantages:

- the vertical resolution is quite good (a few tenth of meters at low altitude).
- the profiles are site specific.
- the data come from direct measurements and have not been processed (but the counterpart is that there are many outliers).

On the other hand the drawbacks of these measurements are the following ones:

- the repartition of the stations on Earth surface is irregular. In Africa, for example the number of stations is very low. We also have no information over oceans.
- The quality of the measurements is not constant, but it depends on the station and on the year.

We decided to use British Atmospheric Data Center (BADC) data because of the great number of available stations and the great number of levels contained in the data. Please note that other sources of radiosonde profiles are available, like the FUB-ESA RAdioSonde (FERAS) database or the NOAA database[35]. They have been used during this study for cross comparisons.

The British Atmospheric Data Center provides 2 types of radiosonde profiles. The first one consists in standard profiles from all over the world from 1995 to 2005. In general, it contains between 80 and 100 levels from surface to 20000-30000 m. Only a dozen of them are directly exploitable because of the great number of outliers and errors of transmission.

The second type of data is a set of high resolution data and are only available for United Kingdom. Here the number of levels attains 2000, the mean distance between 2 levels is approximately 12 meters and all the levels are immediately useful. In fact, when a balloon is launched, measures are taken regularly during the ascent and directly sent to the receiver. Then, for an easier processing of the data for meteorological applications, only a few number of measurements are kept in the profiles. For the BADC high-resolution data set, good quality radiosondes have been used and all the received data have been stored in the files.

The first data set is a useful worldwide source of atmospheric data and the second one could serve as a reference for estimating the accuracy in the treatment of the standard raw data.

The following text explains how we could improve the retrieval of the profiles from the raw files in order to gain accuracy in the tropospheric delay computation. The section 3.2 is devoted to saturation partial pressure models because this parameter is the key element to translate the provided dew-point temperature into the water vapor pressure that we use in our formulas. In sections 3.3 and 3.4, we discuss two strategies to complete missing information in the profiles, and thus to improve the precision of the calculated delay. Section 3.5 is devoted to a comparison of the integration algorithms. Then in section 3.6, we made a cross-comparison between profiles measured in Uccle (Belgium) provided by the Belgian Royal Meteorological Institute and BADC. We made this comparison because researchers working on scintillation phenomena found different results using one data set instead of the other. We wanted to be sure that the BADC data set was not corrupted or biased. Finally, the last section is devoted to a comparison of the models to the integrated delays in several places around the world.

3.2 Saturation partial pressure

As we were checking the procedures used in the data processing in ESA algorithm, we found that the conversion from relative humidity to water vapor pressure could

be a source of problems. The implemented equation came from the Goff-Gratch formulae (see details below), but the function was cut into two parts. Above -40°C, an equation related to water vapor pressure above liquid water was used, while under this threshold we applied another relationship linked to the water vapor pressure above ice. A consequence of this implementation was that the overall function was not continuous.

3.2.1 Introduction to the physics of the saturation partial pressure

Let us take a closed recipient containing liquid water at a temperature between the freezing point and the boiling point. Due to the molecular kinetic energy, some particles leave the surface of the fluid during a phenomenon called evaporation. In the same time, water vapor particles condensate because the ambient temperature is below the boiling temperature. The saturation vapor pressure is the vapor pressure reached when the condensation rate is equal to the evaporation rate. Experience shows that the higher the temperature is, the bigger the water vapor contents in the air will be. Before the end of the eighteenth century the phenomenon was explained by the fact that hot air could dissolve more vapor that cold air. Since Dalton, we know that the partial pressure of a gas is totally independent from the pressure of the others. It only depends on the temperature which shifts the equilibrium state. As the temperature increases, the water molecules possess more kinetic energy so that more particles can escape from the surface. The consequence is that the amount of water in the air is higher; this also means that the condensation rate becomes higher thus leading to another equilibrium state.

When the temperature is sufficiently low, ice can be transformed directly into vapor without passing by the liquid state thanks to sublimation. As the sublimation rate is different from the evaporation rate, the values of the saturated vapor pressure are not the same. In literature this phenomenon is referred as saturated vapor pressure over ice as opposed to the saturated vapor pressure over liquid water.

Anyway, by convention, when dealing with conversions from relative humidity to dew point temperature or to water vapor pressure, the equation to take into account in the saturation partial pressure over water, even if the real physical situation would lead into the formation of ice.

3.2.2 Review of the formulae

We know that the equation of the water vapor pressure is an increasing function of the temperature but there is no simple analytical relationship. To bypass this

inconvenient, empirical relations are used by meteorologists and physicians of the atmosphere. Here is a short review of these equations:

Goff Gratch: This is the original formula edited by Goff and Gratch in 1946

$$\begin{aligned}\log_{10} e_s &= -7,90298\left(\frac{373,16}{T_k}-1\right)\\ &\quad +5,028008\log_{10}\left(\frac{373,16}{T_k}\right)\\ &\quad -1,3816\,10^{-7}\left(10^{11,344.(1-T_k/373,16)}-1\right)\\ &\quad +8,1328\,10^{-3}\left(10^{-3,49149.(\frac{373,16}{T_k})}-1\right)\\ &\quad +\log_{10}(1013,246)\end{aligned}$$

where e_s is the saturated water pressure in hPa and T_k is the temperature in K.

Magnus Teten: In 1967 Magnus Teten proposed the following equation:

$$\log_{10} e_s = \frac{7,5T_c}{T_c+237,3}+0,7858$$

where T_c is the temperature in °C.

Vaisala: In 1980, Vaisala has given two expressions of the saturated vapor pressure, one using exponents of 10 and one using an exponential function:

$$\begin{aligned}e_s &= 6,1\,10^{\frac{7,5T_c}{237,3+T_c}}\\ e_s &= 6,1\,\exp\left(\frac{17,27T_c}{237,3+T_c}\right)\end{aligned}$$

The first formulation is in fact very similar to Magnus Teten's one.

Bolton: Still in 1980, Bolton proposed another similar equation:

$$e_s = 6,112\,\exp\left(\frac{17,67T_c}{243,5+T_c}\right)$$

Hyland and Wexler: In their paper from 1993, Hyland and Wexler suggested the following equation:

$$\begin{aligned}\log_{10}(e_s/100) &= -0,58002206\,10^4\,\frac{1}{T_k}+1,3914993\\ &\quad -0,4864768\,10^{-1}T_k+0,41764768\,10^{-4}T_k^2\\ &\quad -0,14452093\,10^{-7}T_k^3+6,5459673\,\log(T_k)\end{aligned}$$

Sonntag: In 1994, Sonntag proposed the following formulation:

$$\begin{aligned}\log_{10} e_s &= -6096,9385\frac{1}{T_k} + 16,635794 \\ &\quad -2,711193\,10^{-2}T_k + 1,673952\,10^{-5}T_k^2 \\ &\quad +2,433502\,\log(T_k)\end{aligned}$$

Liebe: Liebe gave the following formula (1997):

$$e_s = 2,408\,10^{11}\left(\frac{300}{T_k}\right)^5 e^{-22,644\frac{300}{T_k}}$$

ITU-R P453-8: The International Telecommunication Union recommends a formulation very close to Vaisala's one:

$$e_s = 6,1121\,\exp\left(\frac{17,502T_c}{240,97+T_c}\right)$$

Buck: In 1996 Buck updated his previous expression from 1981. That became:

$$e_s = 6,1121\,\exp\left(\frac{18,678-T_c}{234,5}.\frac{T_c}{257,14+T_c}\right)$$

WMO: The World Meteorological Organisation proposes the formula:

$$\begin{aligned}\log_{10} e_s &= 10,79574\left(1-\frac{273,16}{T_k}\right) \\ &\quad -5,02800\log_{10}\left(\frac{T_k}{273.16}\right) \\ &\quad +1,50475\,10^{-4}\left(1-10^{-8,2969\frac{T_k}{273,16}-1}\right) \\ &\quad +0,42873\,10^{-3}\left(10^{4,76955.(1-273,16/T_k)}-1\right) \\ &\quad +0,78614\end{aligned}$$

this formulation is derived from Goff's 1957 paper. We recommend the interested reader to have a look at the history and the relative comments given by Vömel [47].

3.2.3 Results

In the first two figures, we plotted these functions in order to compare them. We also added functions coming from linear interpolation of tabulated values. The reference tables that we used came from Rogers and Yau [38] and from the web

site HyperPhysics [23]. We notice immediately that the given numbers do not correspond exactly. If we look carefully to the first graph, we can remark that the curve from the HyperPhysics tables is slightly different from the others. This is due to imprecision issued from the rough interpolation: the given points are not close enough. We can already conclude that, to estimate the saturated vapor pressure, it is preferable to use continuous functions, and that the measurements should only be used to select the best relationship.

In the legend of the first figure, we can see two Goff Gratch curves; the first one refers to the equation that was implemented and in which it was considered that the equation above ice should be utilized under -40°C.

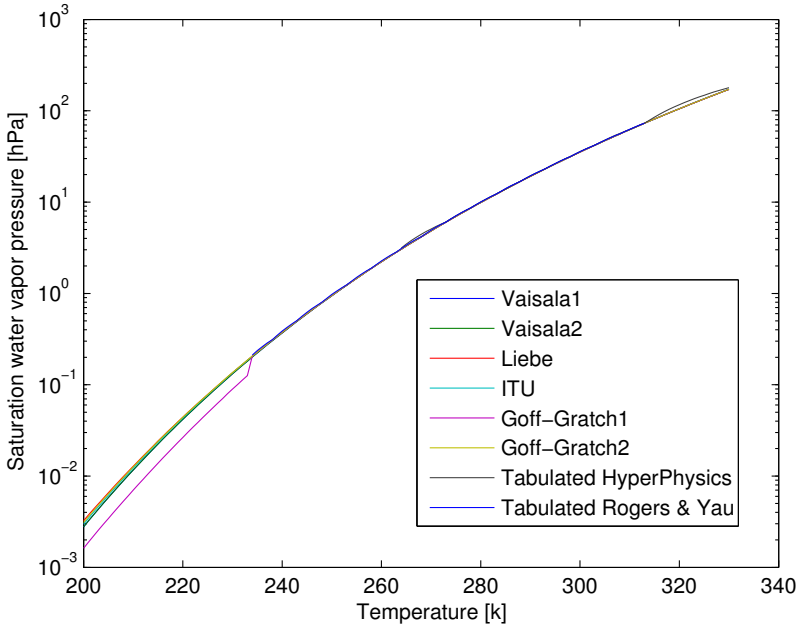

Figure 3.1: Graphics of the saturation vapor pressure as a function of the temperature with logarithmic scale (*first part*). Goff-Gratch1 refers to the formulation where the function is spread into two parts, one for temperatures above 40°C and one for temperatures under 40°C. In fact the part under 40°C is the formulation above ice and not above liquid water. We have separated the figure in two graphics for more clarity. We can observe that except the Goff-Gratch1 formulation all these curves are very close to each other.

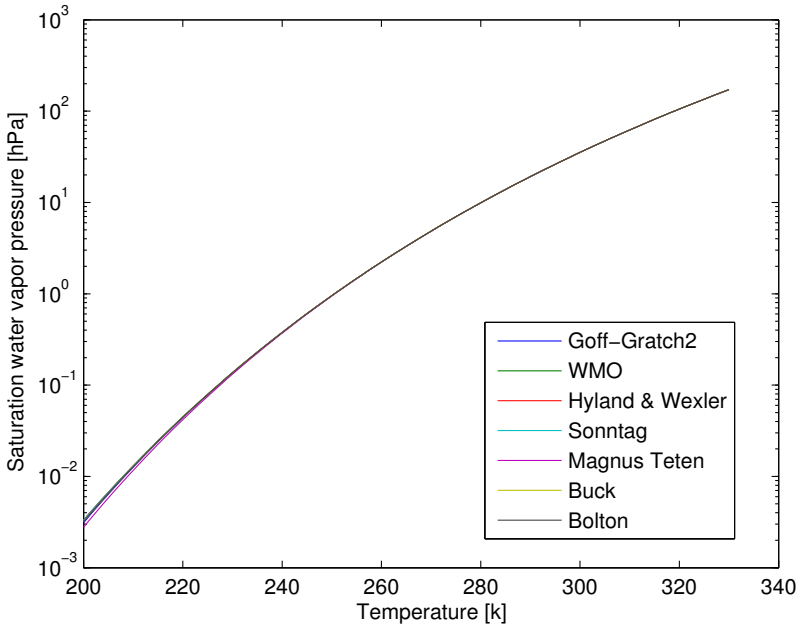

Figure 3.2: Graphics of the saturation vapor pressure as a function of the temperature with logarithmic scale (*second part*).

As the curves are very close to each other, and as the pressure range is quite large, it is interesting to display the differences between these formulas and one of them taken as a reference. Following the example of Vömel, we chose the Goff Gratch equation because it is the most widely used.

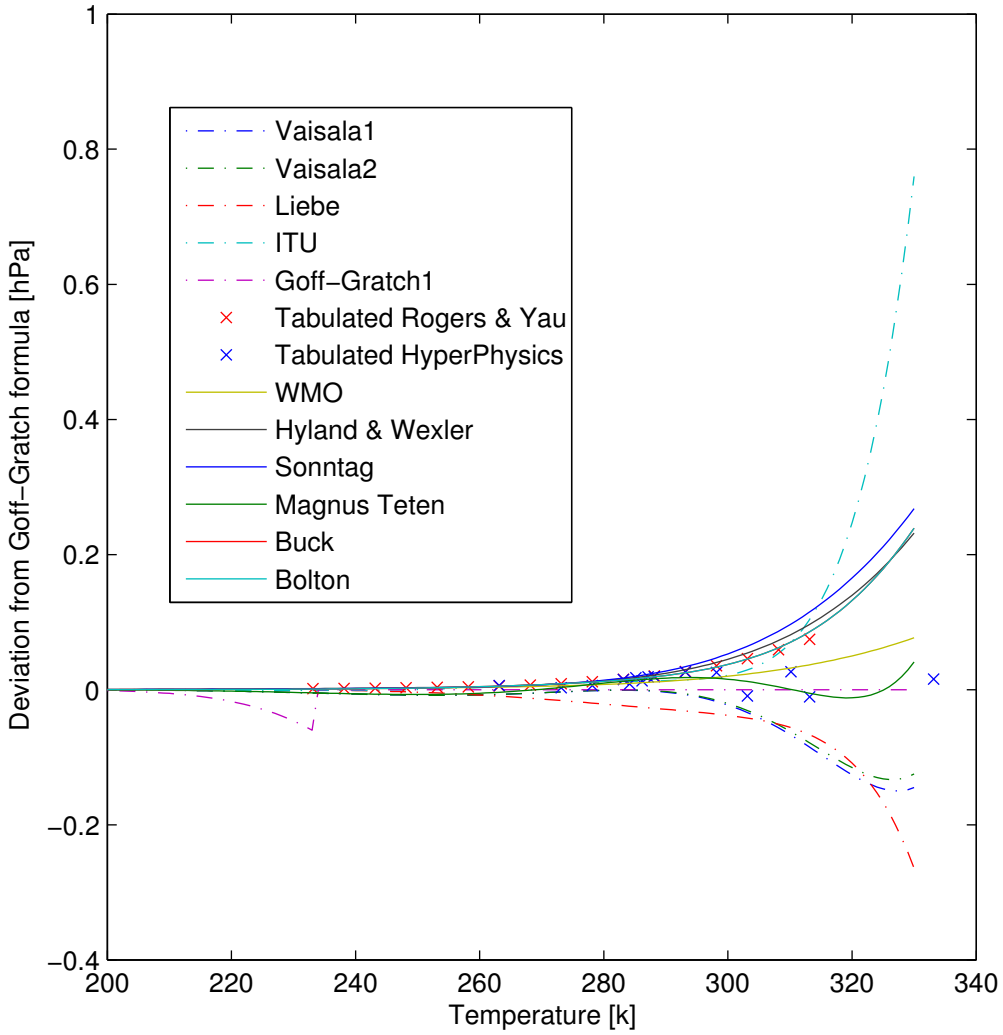

Figure 3.3: Graphic of the deviation from Goff-Gratch over liquid water formula in hectopascals. The crosses are the tabulated values. We can already notice that the two Vaisala, the Liebe and the ITU formulae are not the best choices.

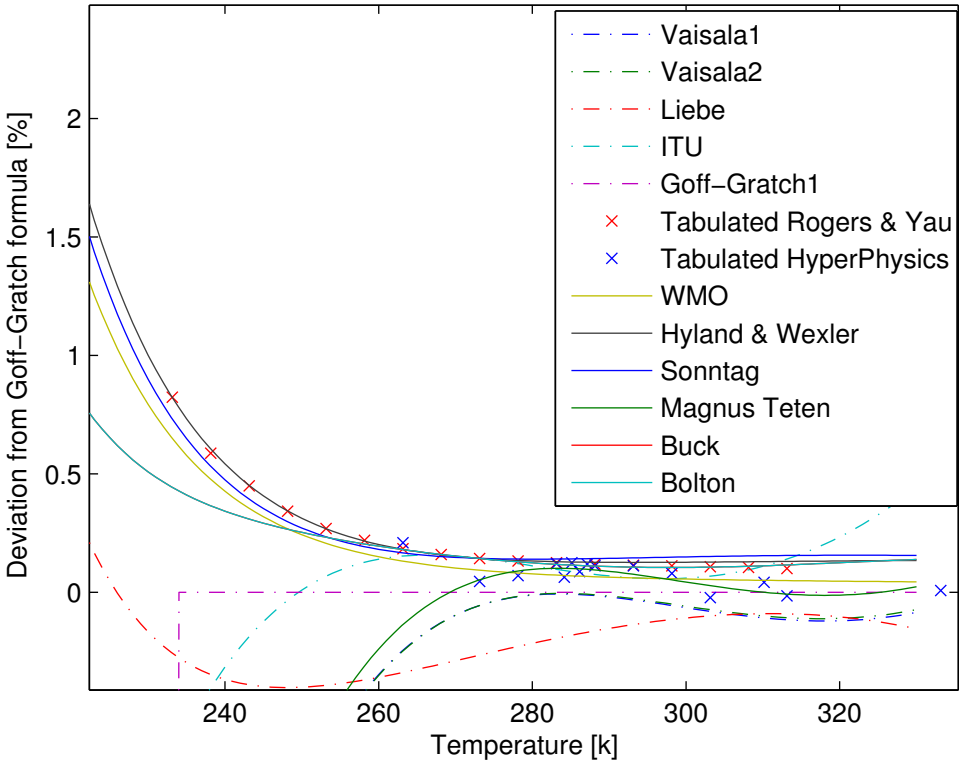

Figure 3.4: Graphic of the deviation from Goff-Gratch over liquid water formula in percents. It is obvious that the tabulated values are different at high temperature depending on the data origin.

The equations that fit the best with the observations are Goff-Gratch, WMO, Buck and Bolton. The Magnus and Teten seemed to be a good choice in the graphic of the absolute deviation, but in the graphic of the relative deviation, we can observe a big difference with the measured values at low temperatures. To choose between the remaining formulations, as the tabulated values are different and as we do not have any estimation of the errors, we think that we should use a compromise. This conclusion is consolidated by the curve reported on Vömel's web page referring to experimental measurements made by Fukuta and Gramada which are different as well at low temperature from the ones reported here. The problem of the measurements of the water vapor pressure at low temperatures should still be considered as an open issue.

Our opinion is that Buck's curve and Bolton's one have an excellent fitting with the values given in Rogers and Yau, but this is slightly artificial since the coefficients have been chosen for fitting to this particular data set. We would

recommend either the WMO formula that has been revisited in 2000, because this curve gives the best fitting with all the tables in my possession, or the Goff-Gratch's one as suggested by Vömel because it is still considered as the reference equation by many meteorologists in the range from -50°C to 102°C.

Anyway we should remain conscious that the differences between the formulae are only a few hundredth of hectopascals at high temperature but can reach 5% at 210K and 25% at 185K. This is no really critical issue in our applications, as water vapor pressure is not important at high altitudes, but the error induced by the saturated pressure formula in the estimation of water vapor pressure using dew point temperature is not negligible in the upper atmosphere.

3.2.4 Comparison with the formula used for the BADC high-resolution profiles

The BADC high-resolution profiles contain more fields than the standard ones. For example, we can find both relative humidity and dew point temperature. This allows us to check which formula was used comparing the given relative humidity to the one calculated from dew point temperature. Assuming that BADC used the same equation for standard resolution data, this will enable us to gain further accuracy in the determination of the water vapor pressure.

On the graphics below we compared the different ways to recompute relative humidity in order to estimate which equation was used by the BADC. It obviously appears that they did not use a two part function but simply a formula above liquid water.

For more clearness, we plotted on a second graphic focusing the more probable formulae. We can remark easily that the Goff-Gratch equation does not match.

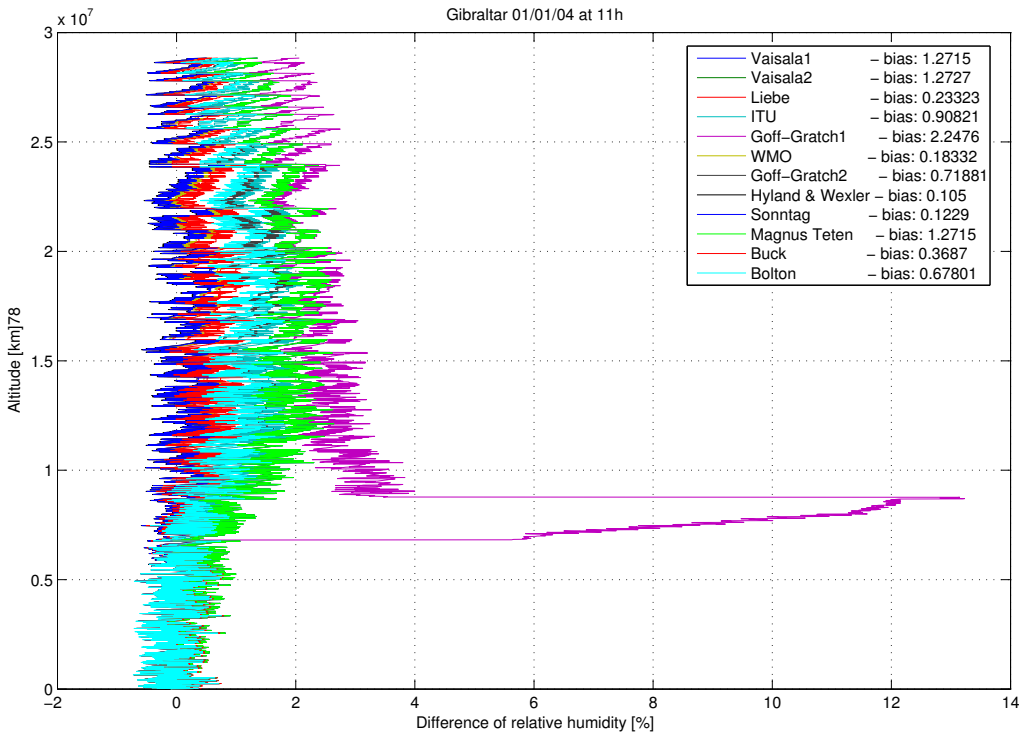

Figure 3.5: Graphic of the difference between the given relative humidity and the relative humidity recalculated from the given dew point temperature as a function of the altitude. Goff-Gratch1 refers to the implemented function and Goff-Gratch2 refers to the equation above liquid water. We can notice that the way the Goff-Gratch formula was implemented does not correspond at all to the formula used by BADC. In the legend there are also the values of the mean difference between the relative humidity for each function.

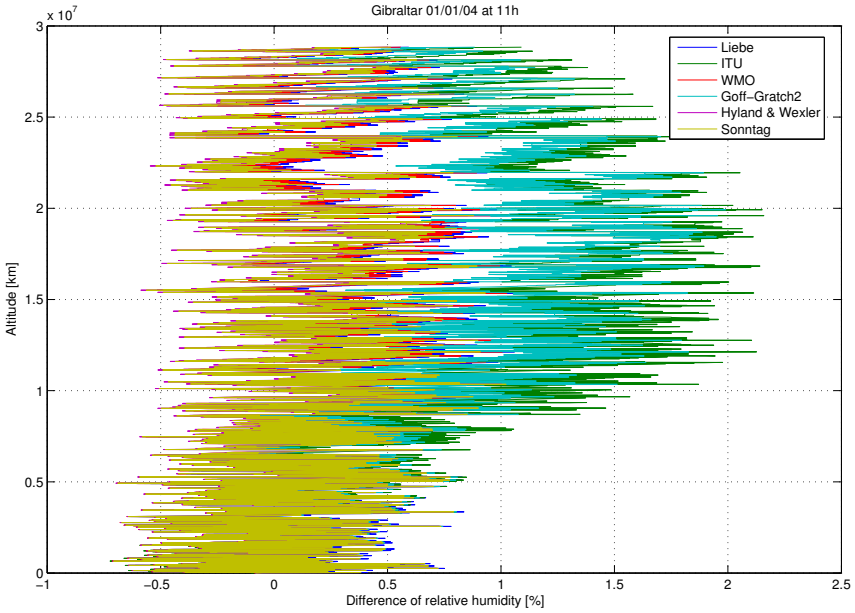

Figure 3.6: The same graphic, but some uninteresting curves have been removed. It is noticeable that the Goff-Gratch equation does not give the best fitting.

It came out from our tests in Gibraltar that the best fitting formulae came from Liebe, WMO, Hyland & Wexler and Sonntag with a mean difference in relative humidity of less than 0,2% (and often even under 0,01%).

3.3 Altitude recovering

For the standard case, five physical variables are known for each level: pressure, altitude, temperature, dew point temperature, wind force and wind direction. The last two data are not relevant for us, because it doesn't influence the tropospheric delay.

In order to get rid of the outliers, we can use levels where all the values are correct or an already existing procedure called BADC_UAD_FILTER designed to remove errors and to interpolate the data when existing levels were very separated.

We noticed that, by using these two methods, we were losing a lot of data because there were many levels where only the altitude was missing. The first thing that we wanted to verify was whether there was a real difference between the temperature from the BADC_UAD_FILTER against pressure profiles (where intermediate levels were added) and the equivalent profiles available in the original data. The result is that the filter interpolates linearly so that the addition of levels

does not improve the resolution of the data. It also appears that there was, as expected, unused information in the data set that would be useful to acquire in order to improve the accuracy of the profile.

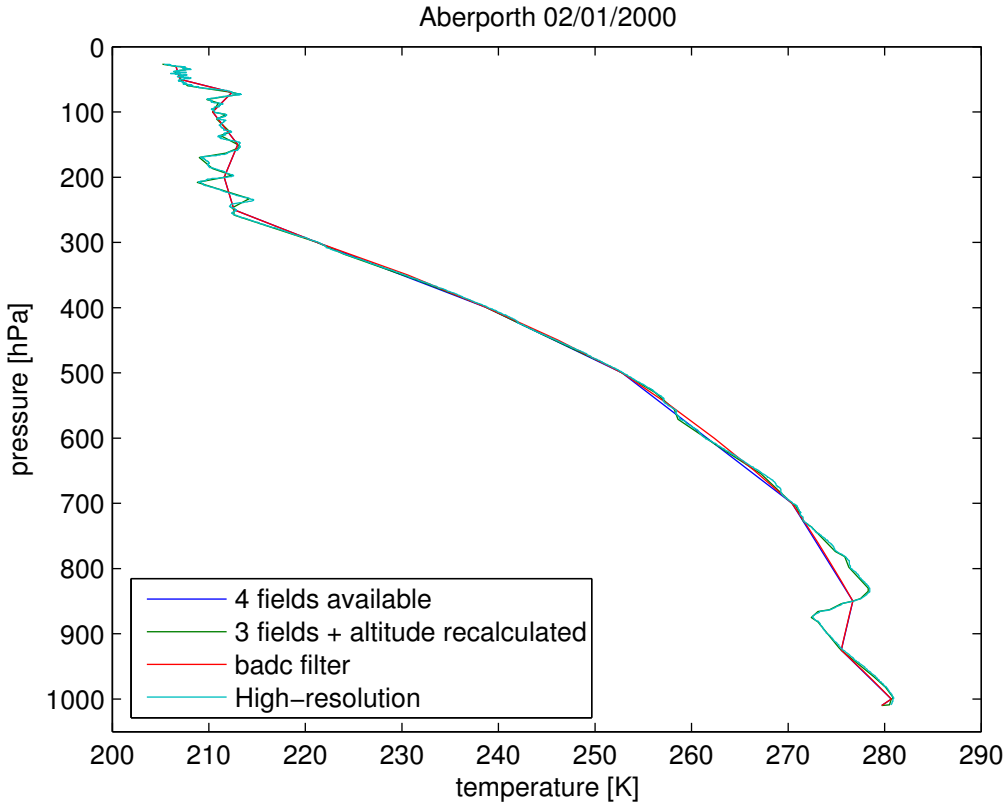

Figure 3.7: Graphic of the temperature profiles as a function of the pressure. We can see that the BADC_UAD_FILTER data and the 4 fields available data profiles are very close. When we compare these profiles to the ones obtained when using all the levels where pressure and temperature are available, we notice that there is an information loss. The high resolution profile proves that the lost information was relevant and should not be ignored.

The problem consisted then in retrieving altitude from the three other fields (pressure, temperature and dew point temperature) thanks to the hydrostatic equilibrium and the perfect gas law.

$$-dp = g\rho\, dz \quad \text{and} \quad p = R\rho T$$

Before getting a satisfactory equation we tried a very rough approximation:

$$Z_1 \;=\; Z_0 + R_d \frac{T_0 + T_1}{2g} \ln\left(\frac{p_0}{p_1}\right)$$

where Z_i is the altitude of the level i, $R_d = 287[J/(K\,kg)]$ is the gas constant for dry air, T_i is the temperature of level i, p_i is the total pressure of the level i and g is the acceleration of the gravity at sea level. This equation totally neglects the humidity, but when we compared the altitude deduced from this technique to the given values for the levels where all the variables were available, the relative error was already very low.

Nevertheless, we tried several ways to improve the method thanks to more physical assumptions. We first used only the dry pressure instead of the total pressure. We secondly tried to weight the gas constant according to the partial pressures of dry air and vapor. Finally we used the virtual temperature[1] instead of the real temperature. We also attempted to correct the acceleration of the gravity with respect to the height.

For our final attempt we assumed that the virtual temperature in the layer between two levels was constant and equal to the mean of the lower value and the upper one. The same assumption was performed for the gravity acceleration.

$$Z_1 = Z_0 + R_d \frac{T_{v0} + T_{v1}}{g_0 + g_1} \ln\left(\frac{p_0}{p_1}\right) \tag{3.1}$$

with

$$T_{vi} = \frac{T_i}{1 - (e_i/p_i)(1-\epsilon)} \;;\; g_i = g\left(\frac{h + R_T}{R_T}\right)^2 \text{ and } g = 9,807(1 - 0,0026\cos(2\phi))$$

where Z_i is the altitude of the level i in meters, $R_d = 287[J/(K\,kg)]$ is the gas constant for dry air, T_{vi} is the virtual temperature of level i in Kelvin, p_i and e_i are respectively the total pressure and the water vapor pressure of the level i in hectopascals, $\epsilon = \frac{R_d}{R_v} = 0,622$ is the ratio between the dry air gas constant and the water vapor gas constant , g is the acceleration of the gravity at sea level in meters per square seconds, h is the height above sea level in meters, R_T is the radius of the earth in meters and ϕ is the latitude in degrees.

As we already mentioned it previously, we compared the values given by the recalculations of the height to the given values. The following graphics show the relative difference as a function of the pressure. We can remark that the relative error is generally decreases as the pressure decreases. Sometimes the error suddenly explodes up to 3% at the higher levels. Our opinion is that this effect is due to inaccuracies at high altitude in the original data set.

[1]The virtual temperature is a fictitious temperature used to easily write the perfect gas law for moist air (p is the moist air pressure and ρ is the moist air density) with the same gas constant as for dry air:

$$p = R_d \rho T_v$$

One of the following graphics shows the mean relative errors for the 14th of each month for the various attempts, in order to verify that there were no real differences in the results along the year.

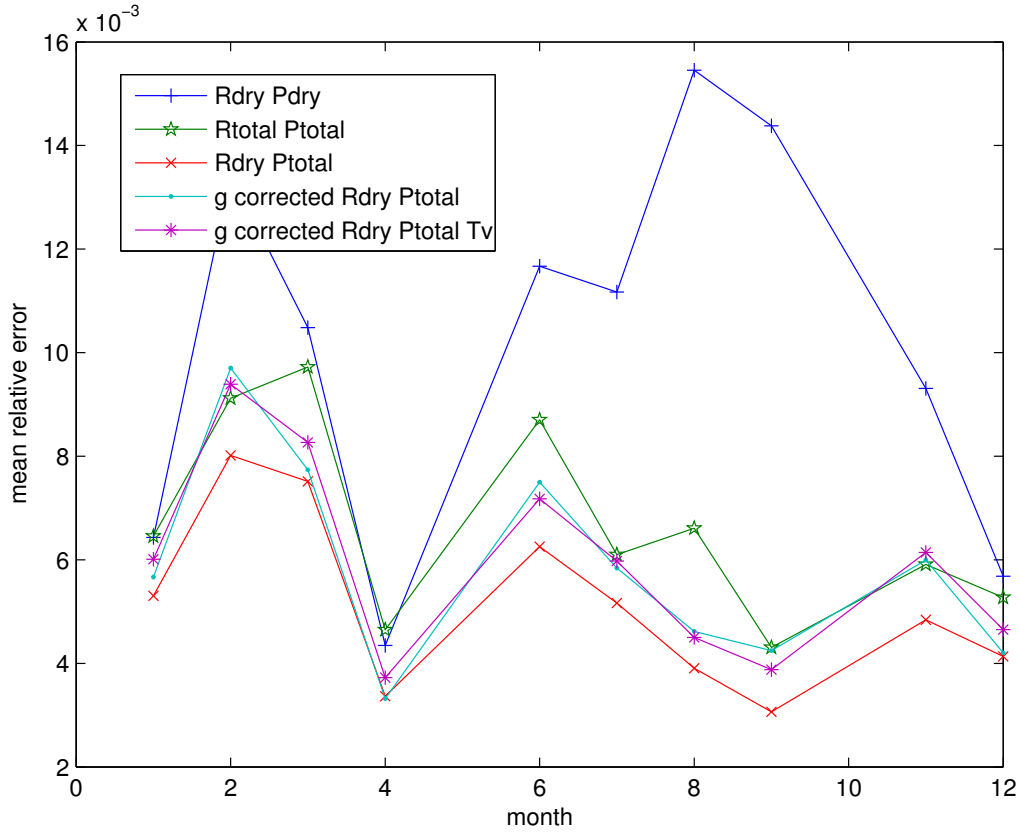

Figure 3.8: Graphic of the mean relative errors for the 14th of each month for the various attempts of altitude recalculation. The blue curve is for dry air values for the pressure and the gas constant. The green curve uses total pressure and a weighted value for the gas constant. The red curve uses total pressure and the gas constant of dry air. The cyan curve uses the same values as the precedent one, but with correction of the gravity acceleration. The purple curve uses dry air constant, virtual temperatures and correction of g.

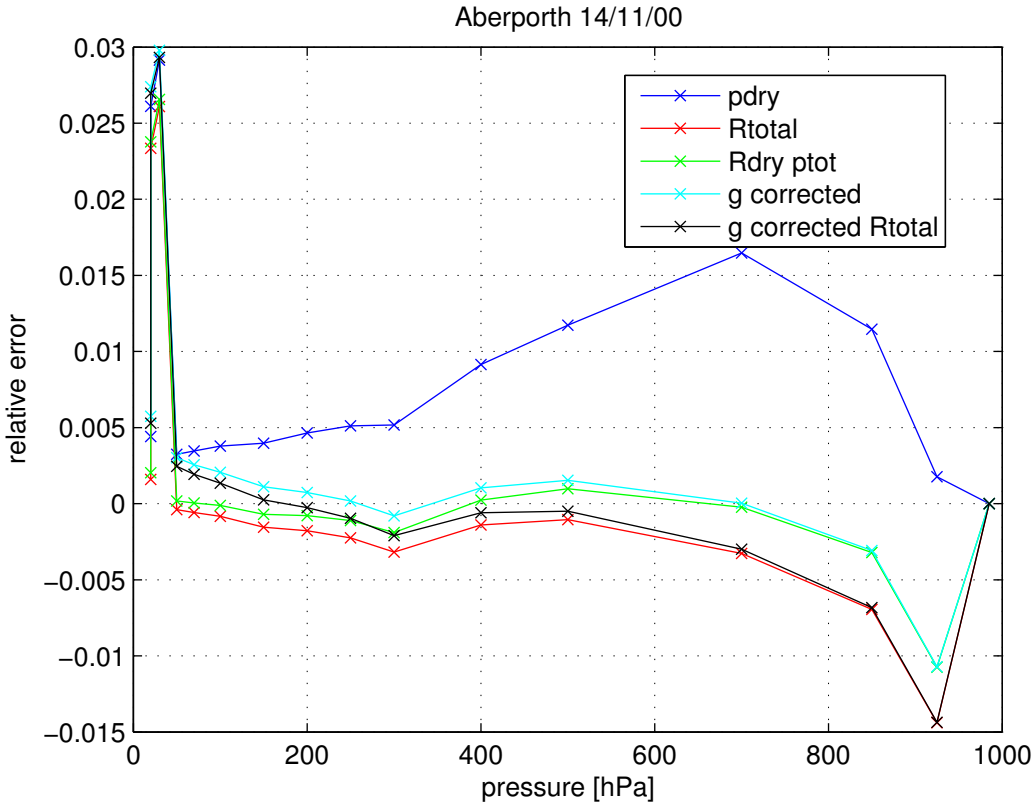

Figure 3.9: Graphic of the relative error as a function of the pressure for the 14/11/2000 at 5h.

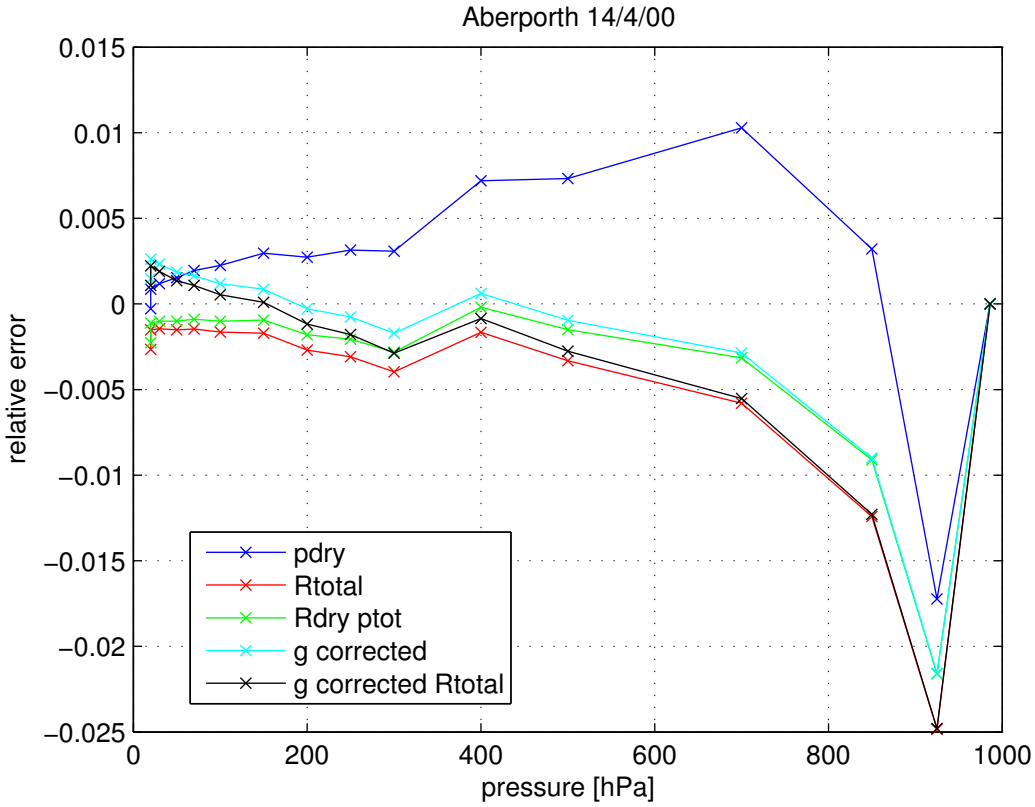

Figure 3.10: Graphic of the relative error as a function of the pressure for the 14/04/2000 at 5h.

Surprisingly we realised that the first equation that we tried, the one supposed to be the least physical, was closest the given values. The most probable reason for this result is that the relative error is so low that the differences of relative errors are due to numerical discrepancies rather than to mistakes in the physical model. Another source of imprecision may be due to the fact that the "most physical" equation introduces more measurement errors because more physical values are introduced. As the differences between the models were minor (less then 0,005), we chose to retain the simplest equation.

We also decided to keep the altitude values when they were given and to recalculate the profile only when the three other fields were available because our purpose was to use as efficiently as possible all the information of the data set and not to discuss the given values.

In order to validate this method, we compared the obtained profiles with high resolution profiles. We can see in the following graphics that the retrieval of the altitude really improves the accuracy of the profiles.

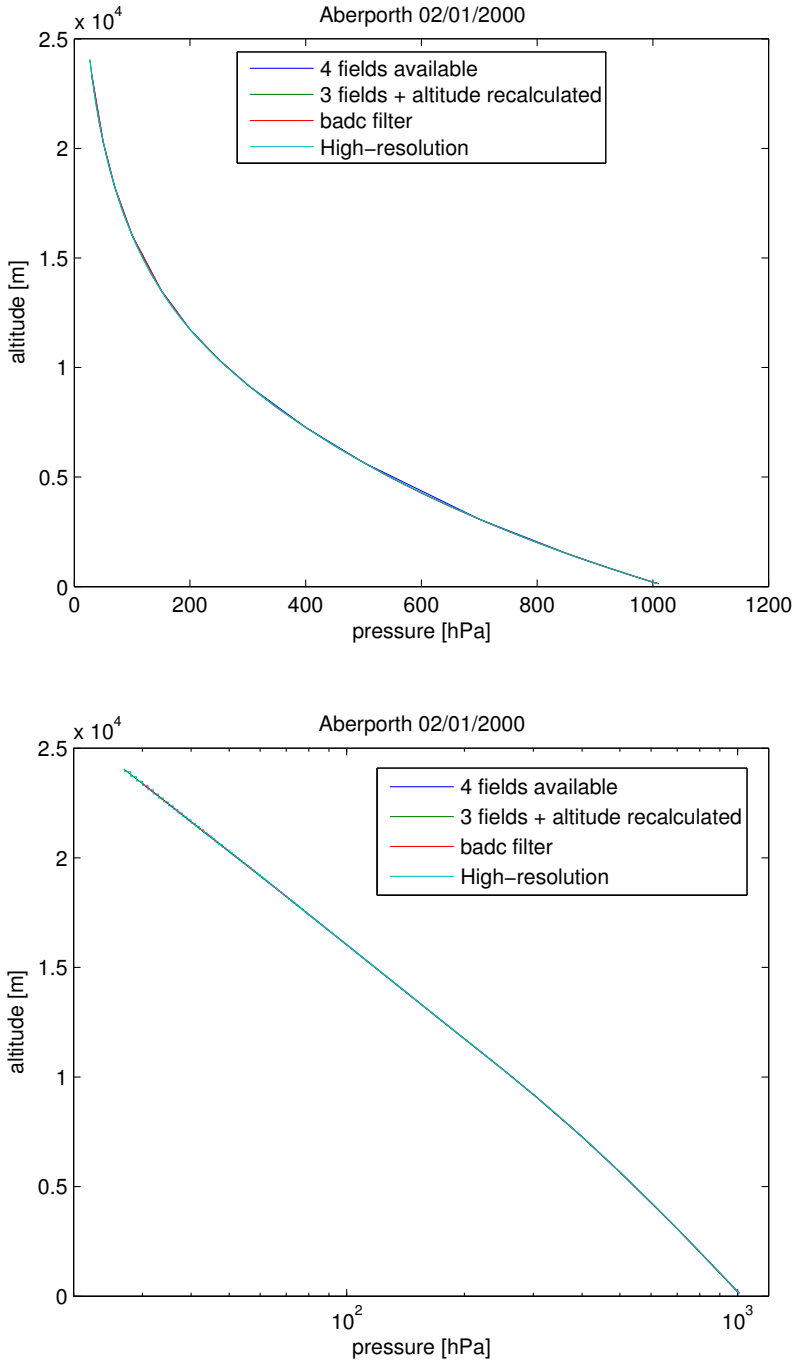

Figure 3.11: Graphics of the pressure as a function of the altitude with linear and logarithmic scales for the pressure. In the logarithmic presentation the profiles are lines. This proves that the hydrostatic equilibrium is respected. There are practically no differences between the various profiles.

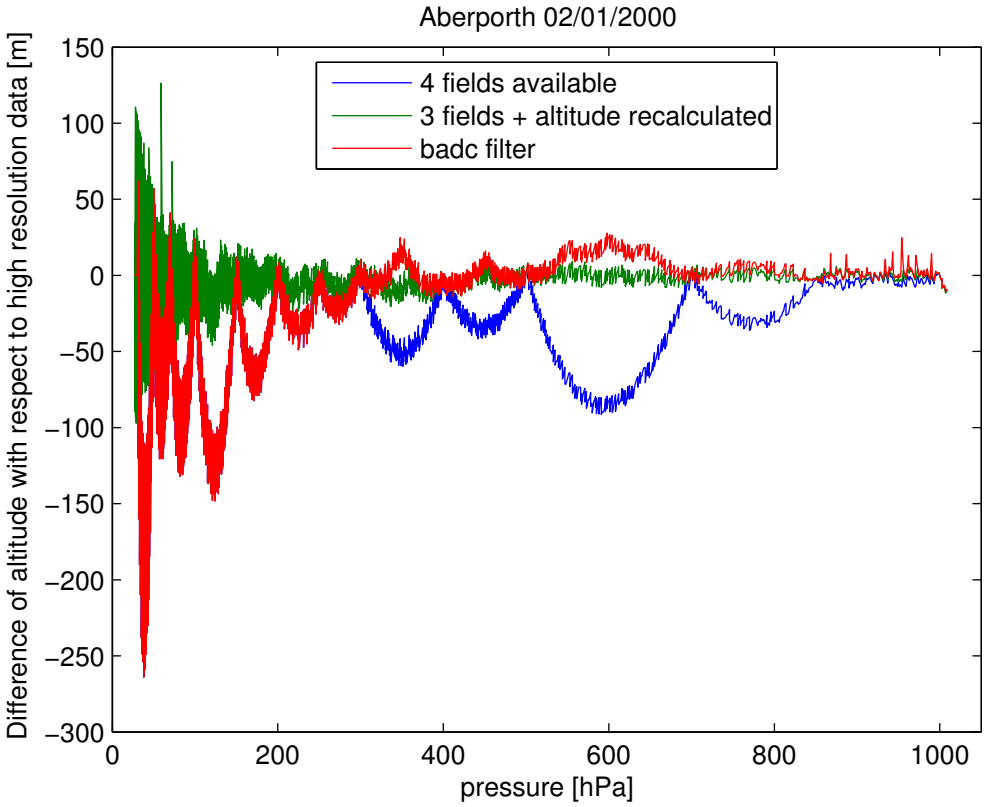

Figure 3.12: Graphic of the difference between the altitude of the three treatments of low resolution data and the altitude of the high resolution data taken as a reference.

As far as the pressure is concerned, this result was no surprise at all: the profile only shows that the atmosphere is in hydrostatic equilibrium so that the pressure decreases quasi-exponentially when height increases. There cannot be big fluctuations on pressure profiles. However, figure 3.12 shows the differences between the three treatments of low resolution data and the high resolution data. One observes that the altitude recovering leads to the maximum accuracy. At high pressure, which means near the surface, we can note that the BADC_UAD_FILTER gives a better result than the simple case for which we only consider levels where 4 variables are available. This increase of the difference of altitude when the pressure is low is likely to come from the accuracy limit of the high resolution data set as it is suggested by the zoom in the pressure profile. We can actually observe steps in the high resolution profile which does not seem to be really natural.

For water vapor pressure profiles, the situation is very different. The graphics show that with high resolution data or with altitude recovering, we can take into

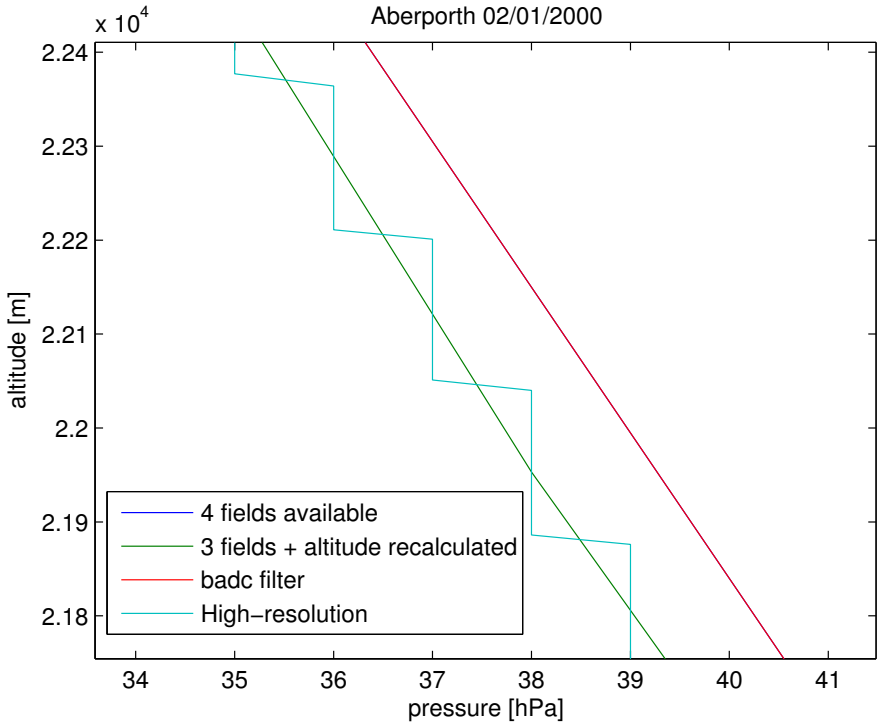

Figure 3.13: Zoom on the graphic of the pressure as a function of the altitude.

account large fluctuations of the vapor contend that were ignored when we used only complete levels or the BADC_UAD_FILTER. The temperature graphic shows more or less the same phenomenon, altitude recovering leads to the same curve as the high resolution data, while the two other curves neglect some temperature variations.

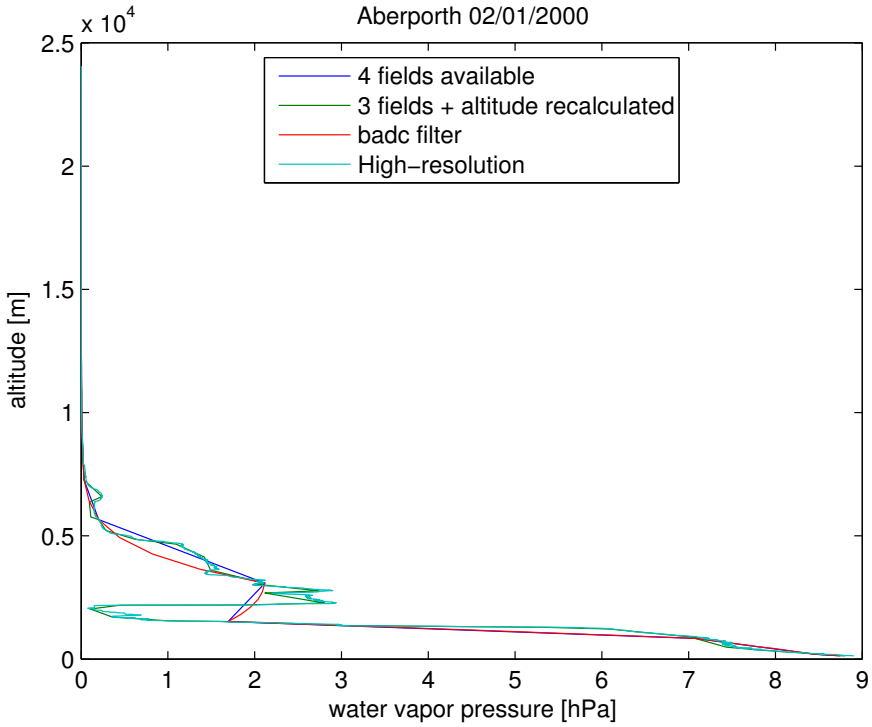

Figure 3.14: Graphic of the water vapor pressure as a function of the altitude. It is obvious that without height recovering, we are missing fluctuation.

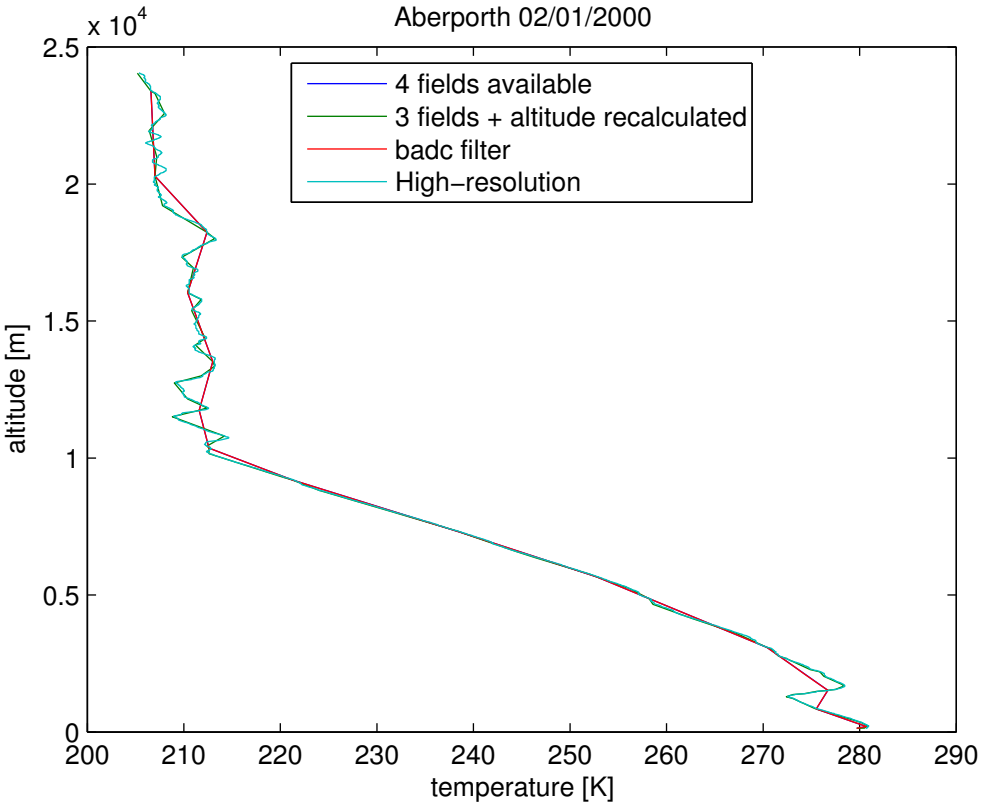

Figure 3.15: Graphic of the temperature as a function of the altitude. As in the previous graphic, we notice that altitude recovering improves the accuracy of the profile.

On the log-log graphic of the relationship between the total pressure and the water vapor pressure that the equation

$$e = e_s \left(\frac{p}{p_s} \right)^{\lambda+1} \tag{3.2}$$

is not strictly respected, otherwise the curve would look more like a line.

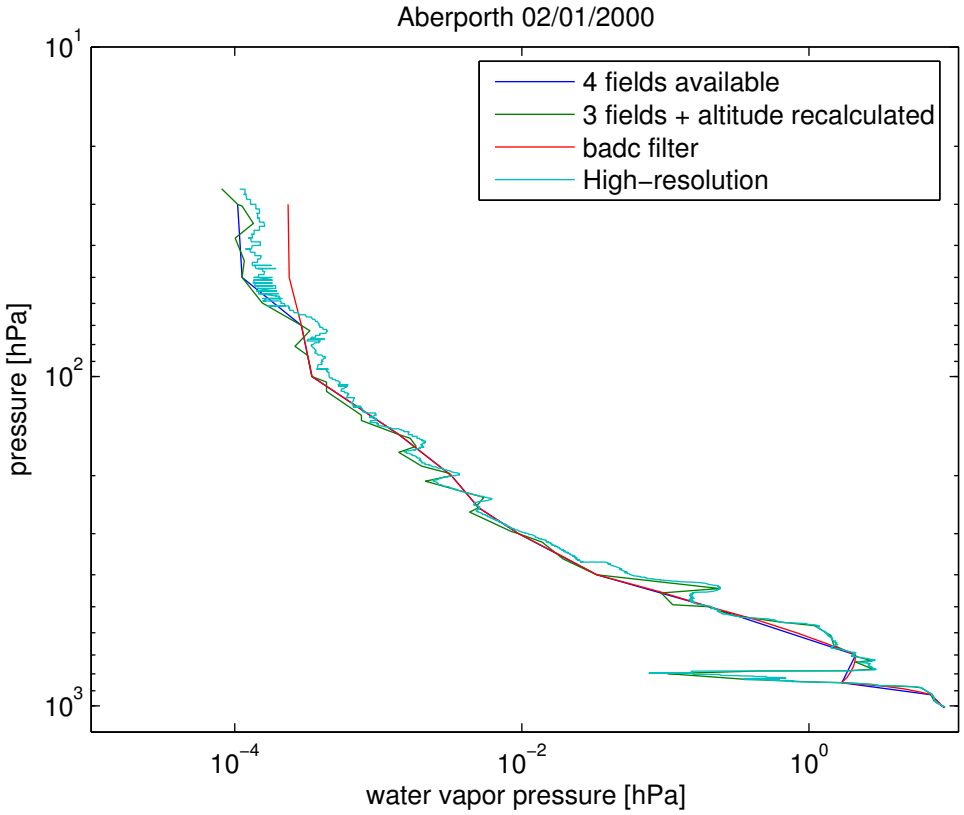

Figure 3.16: Graphic of the water vapor pressure as a function of the pressure in log-log scale.

We also compared the integrated zenith delay in order to see what we can gain by using all the available information. Of course before doing that we have to be sure that the maximum level of the 2 data sets is the same otherwise the comparison would not have any sense. Hopefully it is the case, the mean difference between the maximum levels is 10 meters[2], which is nothing compared to the altitudes considered (about 20000 meters).

The values of the delay are reported in the table 3.1. Once again we can take note of the improvement in accuracy thanks to the altitude recalculation. We calculated the mean difference between the three treatments of standard resolution data and the high resolution data for the month of January and the results are reported in table 3.2. We can remark that the interpolation from the BADC_UAD_FILTER the error greatly decreases compared to the simplest treat-

[2]The maximum altitudes are too close for coming from different balloons, even launched at the same time. As both data sets are coming from the same radiosonde, the comparison is totally licit.

ment. But with the recovering of the altitude, the error goes from 1,5 centimeter down to only 3 millimeters, which represents a considerable amelioration of the process.

Zenith total delay [m]	4 fields available	BADC UAD_FILTER	Altitude recovered	High resolution
01/01/00 5h	2.2341	2.2250	2.2466	2.2441
01/01/00 11h	2.2943	2.2859	2.2827	2.2813
01/01/00 17h	2.2455	2.2366	2.2568	2.2577
01/01/00 23h	2.3060	2.2979	2.3005	2.2970
02/01/00 5h	2.3104	2.2989	2.3057	2.3064
03/01/00 5h	2.1814	-	2.2159	2.2088
03/01/00 23h	2.2865	2.2741	2.2835	2.2809
04/01/00 5h	2.1842	-	2.2071	2.2033
23/02/00 23h	2.3520	2.3372	2.3432	2.3440
15/05/00 5h	2.3780	2.3614	2.3713	2.3684
13/06/00 5h	1.9985	-	2.0265	2.0250

Table 3.1: Comparison of the integrated delays using various methods in the acquisition of the atmospheric profiles for a sample of launches at Aberporth in 2000. Sometimes the BADC_UAD_FILTER rejected profiles because of the insufficient number of complete levels available.

	Mean difference [m]
4 fields available	0.0149
BADC_UAD_FILTER	0.0108
Altitude recovered	0.0028

Table 3.2: Mean differences for the month of January at Aberporth when the high resolution data set is taken as the reference.

3.4 Stratospheric water vapor pressure

We tried to check if the improvement in the treatment of the data was only useful on Aberporth[3] or if it could improve the recovery of profiles in other places. In fact in many other locations like Brasilia Airport, Milan Linate or Dakar, altitude was often missing whereas other variables were valid.

[3]We chose this location because we had high resolution data on this English site.

But another problem arose in some places: the maximal altitude in the profiles was only about 10 km and the minimum pressure was between 250 and 300 hPa. We were missing all the stratospheric data. The reason was that above that altitude the dew-point temperature was always invalid. As we know that at this altitude the water vapor pressure is very low and has no more influence on the delay, it would be a pity of losing useful pressure, altitude and temperature values because of the unavailability of a variable that has nearly no importance.

One solution would be to recover the water vapor pressure e from total pressure, ground total pressure p_0 and ground water vapor pressure e_0 and lambda as in equation 3.2. But this relationship would result in adding a model in the measurements. As these radiosonde profiles can then be used to assess models of the atmosphere, this could induce inappropriate conclusions[4]. Instead of assuming a pattern of water vapor contend it has been chosen to assign 0 to the water vapor contend when it was missing in the upper atmosphere.

The problem consisted in selecting a threshold under which the levels where the dew point temperature were missing should be discarded and above which the levels where dew point temperature is missing should lead to $e = 0$. We would like to link the threshold in the the water vapor contend to a variable directly available in the data sets. Equation 3.2 is suitable for this task as it allows a criterion on the pressure[5] : the researched threshold will be on the $\frac{p}{p_0}$ value.

The first approach simply resulted from observation of the data of Brasilia. As the minimum pressure before the humidity sensor failure is in the range between 250 and 300 hPa and assuming a surface pressure of 1013 hPa, this would lead to a threshold from 0,25 to 0,3. This method gives us an order of magnitude but cannot be satisfying, as it is only based on a unique place in the world randomly selected. We do not know whether this place is an exception or whether it is representative of a worldwide behaviour.

A second approach was to chose arbitrary $\frac{e}{e_0} = 0,01$ so that the value of the threshold depended strongly on λ. This parameter can vary from 1,5 to 4 depending on the way the water vapor contend is distributed as a function of the altitude. This results in

$$\frac{p}{p_0} = \begin{cases} 0,4 \ (\lambda = 4) \\ 0,16 \ (\lambda = 1,5) \end{cases}$$

The domain of values is wider than before, but this threshold is no longer based on local measurements in a random site but on worldwide statistical values. We can observe that this range contains the observed range in Brasilia, so we can conclude that Brasilia is no exceptional site.

[4]For example it would be preferable to avoid testing the accuracy of a model with data generated by the use of this (or another) model.

[5]Here we do not want to use the equation 3.2 to derive values but to design a criterion that has a physical meaning; this will not lead to a bias in the measurements.

	English Radiosondes	American Radiosondes	WMO standard
Pressure	0,5 hPa	2 hPa for P>300 hPa 1,5 hPa for 300<P<50 hPa 1 hPa for P<50 hPa	2 hPa
Temperature	0,5 K	0,5 K	1 K
Humidity	2%	5%	7%

Table 3.3: Table of the accuracies of the sensors.

The third approach would be to define the threshold so that the measurement error on the water vapor pressure at this level is equal to the measured value of this pressure. This would mean that we assume a null value as soon as the noise has the same order of magnitude than the signal. From the available variables we can deduce the water vapor pressure

$$e = e_{sat}(T_k)\frac{RH}{100}$$

where e_{sat} is the saturation vapor pressure at the temperature of T_k Kelvins and RH is the relative humidity in percentage.

In order to have an idea of the altitude at which this condition is achieved in statistically realistic conditions, we took profiles from the U.S. Standard Atmosphere. As the atmospheric water vapor contend is expressed in volume mixing ratio[6] (PPMv) in the tables, we have to translate it in water vapor pressure (e in hPa):

$$e = \frac{P.ppmv}{10^6 + ppmv}$$

where P is the pressure in hPa, $ppmv$ is the mixing ratio in part per million. We noticed that the altitude should be around 14 km above sea level, where pressure is approximately 140 hPa. We immediately realise that the criterion is too severe, this means that we would miss all the information between 10 and 14 km.

A fourth way to deal with this problem would be to fix the altitude at 10 km and look in the various atmospheric statistical models what would be the correspondent values for $\frac{p}{p_0}$. The Standard U.S. Atmosphere recommends a value of $p_{10km} = 265$ hPa, which leads to $\frac{p}{p_0} = 0,26$. On the other hand if we follow the ITU recommendations we obtain $p_{10km} = 284$ hPa and $\frac{p}{p_0} = 0,28$ for mid-latitude summer and $p_{10km} = 258$ hPa and $\frac{p}{p_0} = 0,25$ for mid-latitude winter. A third model can be extracted from ERA15 documents and the values are $p_{10km} = 230$ hPa and $\frac{p}{p_0} = 0,23$.

[6]The volume mixing ratio PPMv is the ratio of the number of moles of water vapor to the number of moles of dry air contained in the volume V occupied by the mixture.

In order to decide which value to adopt, we have to remember that we do not need a big precision on this parameter. If the parameter is too low, we will lose levels that could be useful, and if the parameter is too high we will assume a null value where water vapor pressure is not negligible. But at the top of the troposphere, water partial pressure is very low anyway and the vertical profile resolution is not as critical as in the lower levels. It results from the preceding considerations that a value of 0,25 would represent an acceptable threshold.

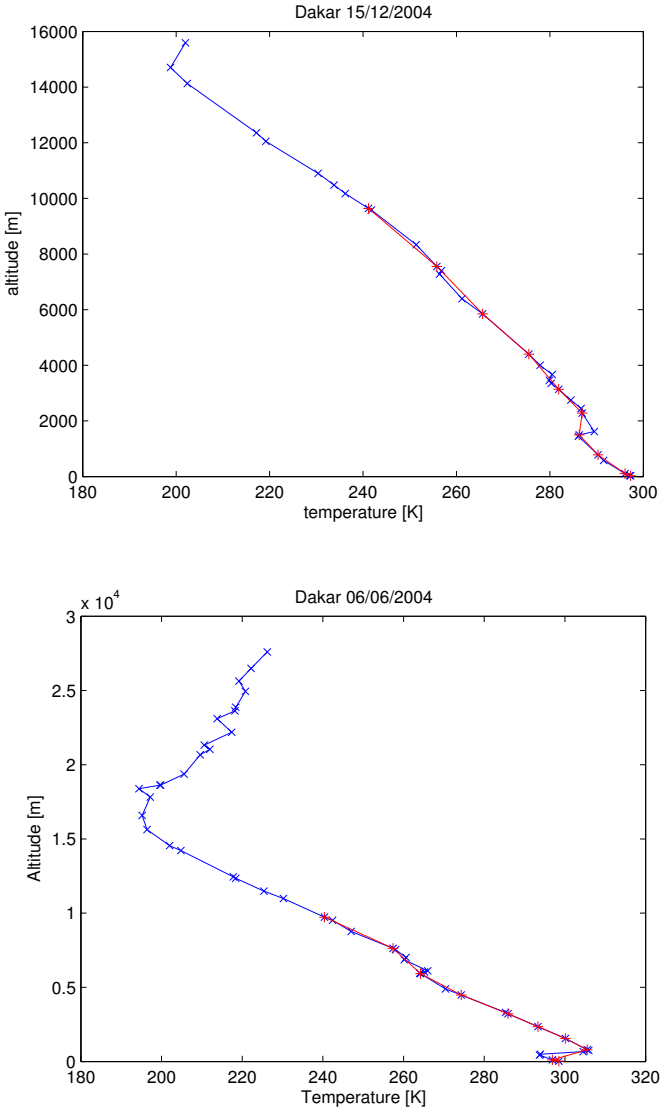

Figure 3.17: Graphics of the temperature as a function of the altitude in Dakar. We can see that our improvements increases the resolution of the profiles, putting temperature inversions in evidence. It is also noticeable that our assumption on the stratospheric water vapor pressure nearly doubles the number of valid levels and the maximum height.

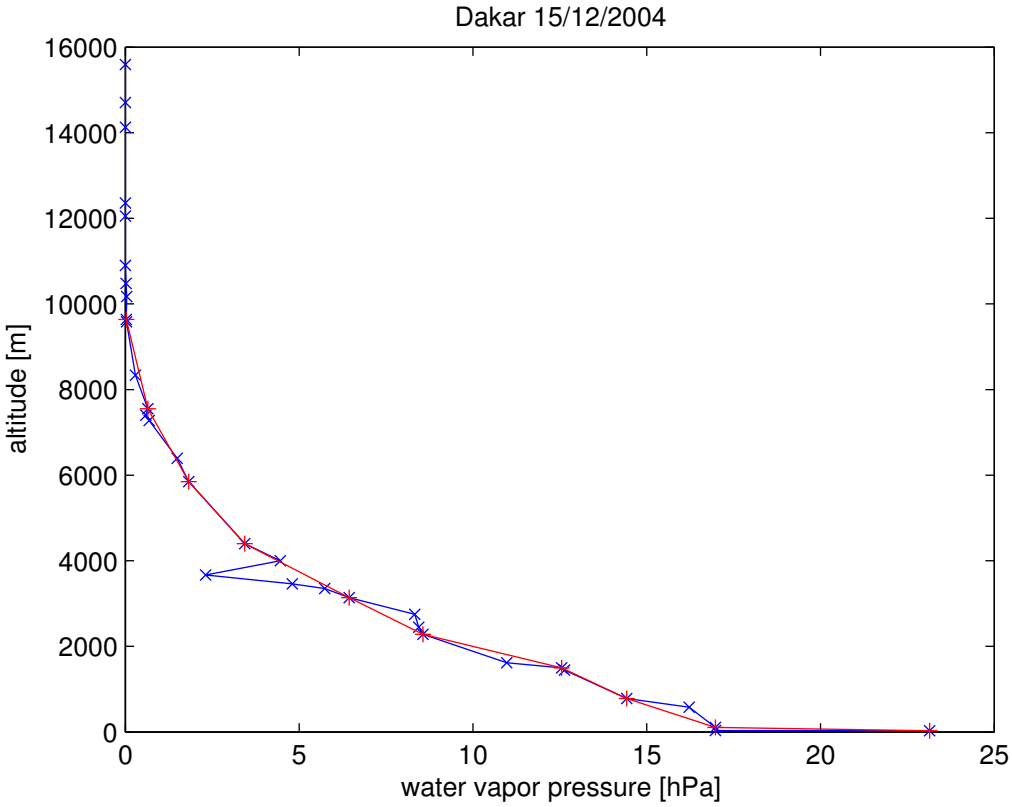

Figure 3.18: Graphic of the water vapor pressure as a function of the altitude in Dakar. Here we notice an amelioration of the accuracy in the profiles in the troposphere.

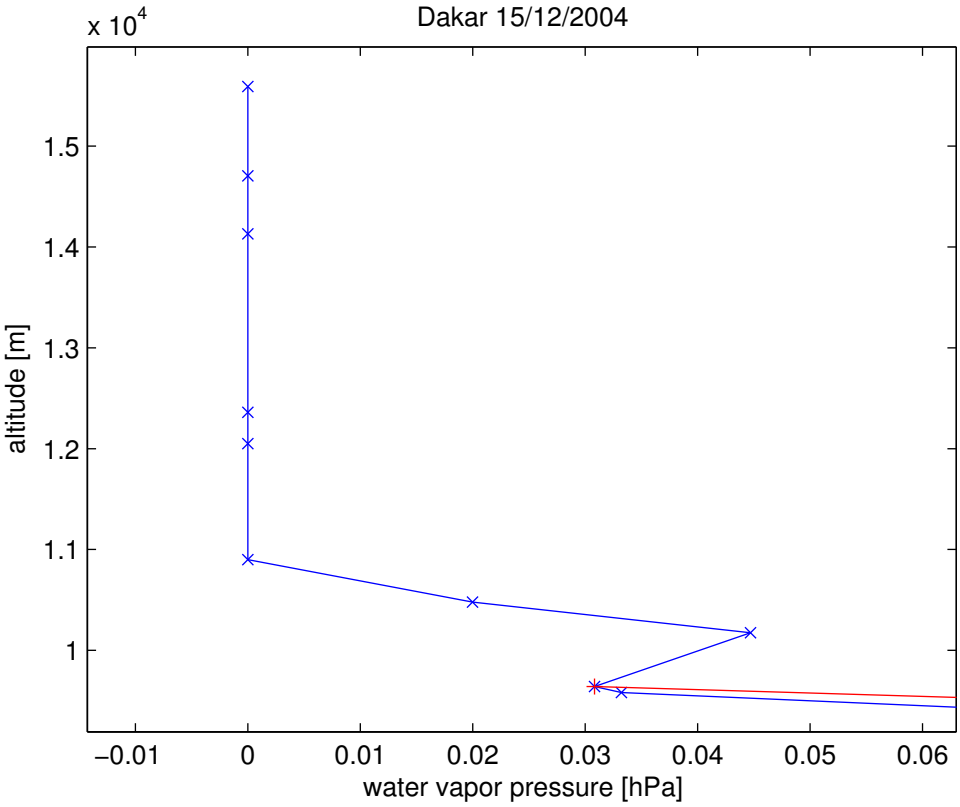

Figure 3.19: Zoom on the graphic of the water vapor pressure as a function of the altitude in Dakar. Here we can observe that the water vapor pressure is already far below 1% of the ground level partial pressure when we force the value down to zero.

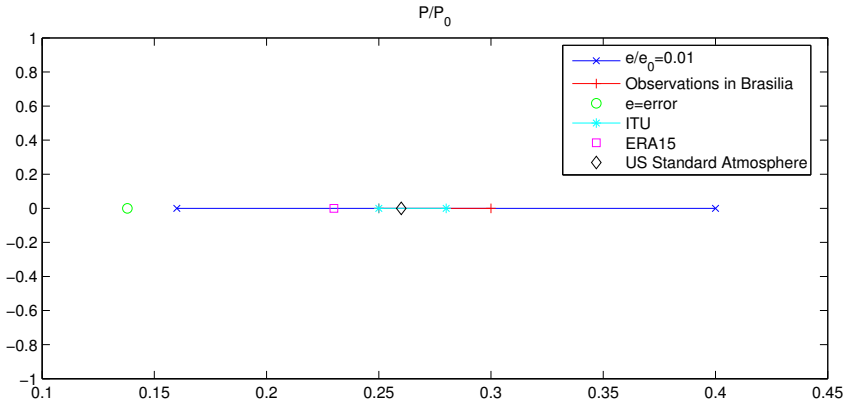

Figure 3.20: Values of the ratio $\frac{p}{p_0}$.

3.5 Integration algorithms

In order to integrate numerically the refractivity for each profiles, several integration algorithms have been tested. The principle remains the same for each method: the refractivity calculated for each layer with formula (2.5) is multiplied by the thickness of the layer and then added to the delay.

The first approach (method 1) was a naive one: it consisted in computing the refractivity of a layer between two levels thanks to the means of the parameter related to the level. For example, the parameters[7] of the layer L comprised between the levels 1 and 2 are expressed as $X_{L1} = 0,5(X_1 + X_2)$.

This way to evaluate the means is in fact equivalent to assuming a linear evolution of the parameters between two levels. This hypothesis is acceptable for the temperature because the temperature profile is generally linear. Nevertheless, it is not very precise for the pressure, as we know that the pressure profile is a decreasing exponential. A mean using a logarithmic weight would be more suitable to estimate the pressure of the layer:

$$P_L = \frac{P_1 - P_2}{\ln(P_1) - \ln(P_2)}$$

The case of water vapor profiles is not so clear because, even if the global profile also looks like a decreasing exponential, the curve is generally very irregular. For this reason, a linear relationship has been preferred in the second approach (method 2). The wet delay will be identical to the one in the first method.

[7] The pressure, the temperature and the water vapor pressure.

The third way to deal with the problem would be to compute directly the refractivity for each level. Then, assuming a decreasing exponential profile of the refractivity, the mean refractivities of each layer is calculated using logarithmic weight. Then the integration is performed by summing the mean refractivities previously multiplied to the thicknesses of the related layers. This algorithm is often preferred for computations of atmospheric absorption of telecommunication signals because of its robustness. It was already implemented in ESA routines, but refractivity was calculated from Liebe's formula instead of Rüger's one. We kept this formula in order to compare this previous formulation to new ones (method 3), but we also tested the calculation of the refractivity with the Rüger coefficients (Method 4).

In order to compare the 4 methods, standard and high resolution radiosonde profiles for the same location (Aberporth U.K.) at the same time (January 2000) have been used. In the following graphics, we compared the integrated total, hydrostatic and wet delays. For numerical integration, the precision depends not only on the method, but also on the width of the steps. This is the reason why we decided to plot the differences of delay as a function of the width of the largest step[8] of the profile. We chose the second method as a reference because it was the one with the strongest physical background.

The first observation is that the differences are below 2 mm in any case, which is below the precision of vertical integration of radiosonde profiles, so that all these algorithms can be used without any problem. It is nevertheless interesting to notice that all the methods using Rüger's coefficient converge when the steps are decreasing: the differences of delay went from approximately 1,5 mm to less than 0,01 mm as we move to high resolution profiles. We can also remark that the deviation between method 1 and method 2 increases as the maximal altitude difference between two levels increases. This observation leads to the same conclusion: the two methods converge when we reduce the integration steps.

On the other hand, the difference between method 2 and method 3 slightly decreases when we improve the resolution, but the difference does not seem to vanish. This is an indication that Liebe's coefficient leads to a small underestimation of the delay if we consider Rüger's ones as references. Comparing the hydrostatic and the wet delay graphs, we can see that the major part of the deviation between methods 2 and 3 comes from the hydrostatic part but the scattering of the total delay samples comes from the wet delay. Concerning the deviation between methods 2 and 4, the dry delay has nearly no influence, all the differences are induced by the wet delay.

The conclusion is that, taking Rüger's set of coefficients as the reference, method 1 is a little bit rough if the number of layers is small, but methods 2 and 4 provide very similar results. If we consider the mean deviation taking

[8]The largest step means the biggest altitude difference between two levels.

method 2 for high resolution profiles as a reference, we can see that the monthly mean deviation of method 4 is smaller than the same quantity for method 2, so that we can conclude that method 4 is the best one.

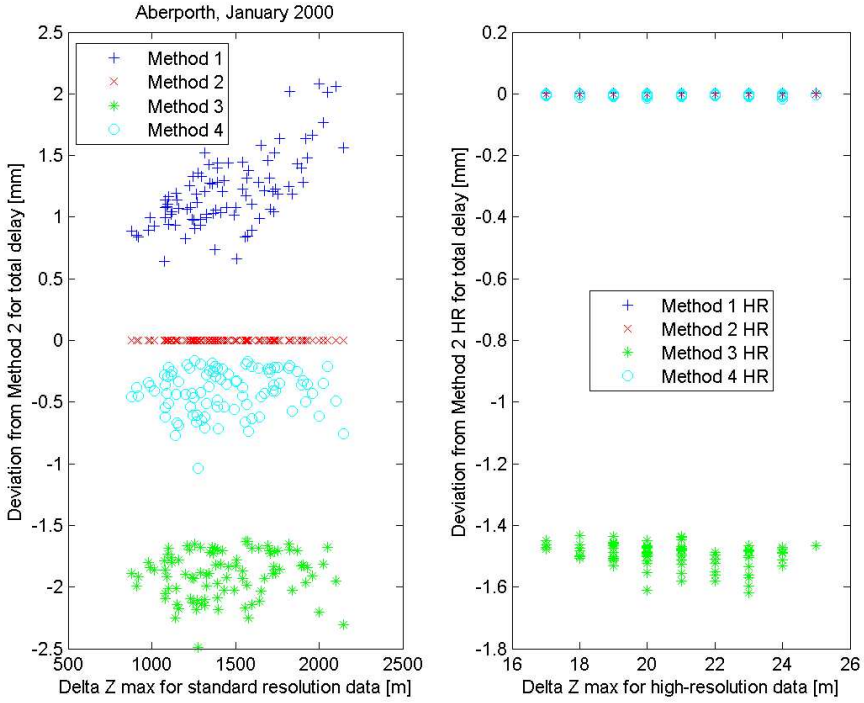

Figure 3.21: Comparison of the 4 integration algorithms for the total delay. The graph on the left plots the deviation of the total delay (method 2 considered as the reference) as a function of the maximal difference of height between 2 levels. The grph on the right represents the same deviation, but for high resolution profiles. The methods 1HR, 2HR, 3HR and 4HR are respectively equivalent to methods 1, 2, 3 and 4 but for high resolution profiles.

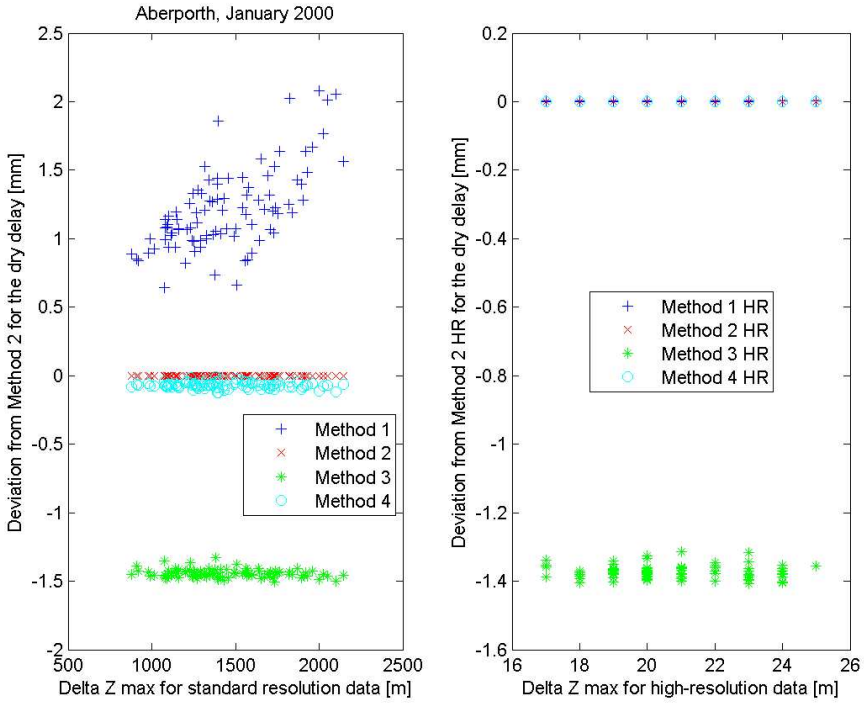

Figure 3.22: Comparison of the 4 integration algorithms for the hydrostatic delay. The graph on the left plots the deviation of the total delay (method 2 considered as the reference) as a function of the maximal difference of height between 2 levels. The grph on the right represents the same deviation, but for high resolution profiles. The methods 1HR, 2HR, 3HR and 4HR are respectively equivalent to methods 1, 2, 3 and 4 but for high resolution profiles.

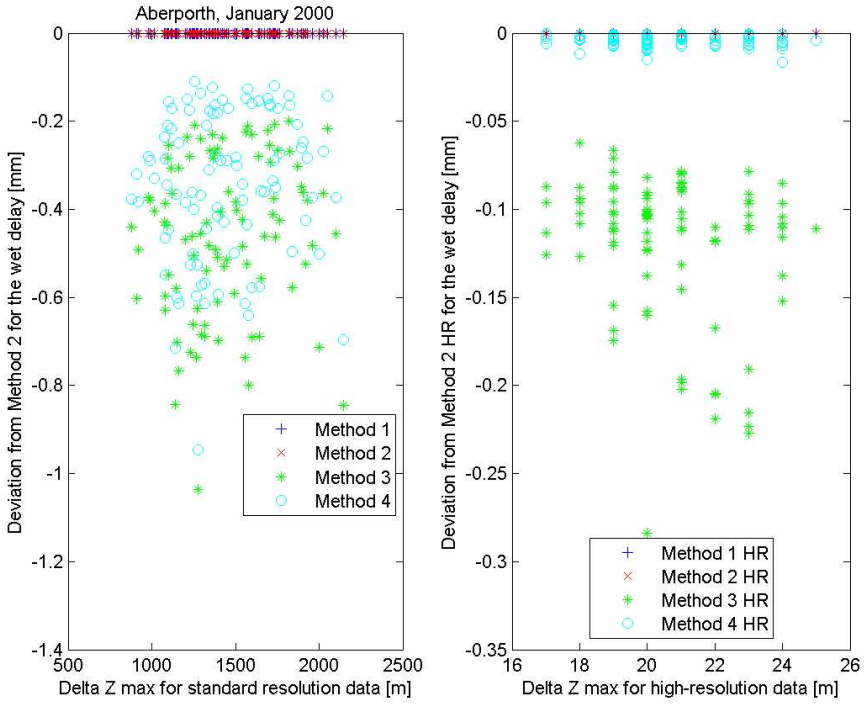

Figure 3.23: Comparison of the 4 integration algorithms for the wet delay. The graph on the left plots the deviation of the total delay (method 2 considered as the reference) as a function of the maximal difference of height between 2 levels. The grph on the right represents the same deviation, but for high resolution profiles. The methods 1HR, 2HR, 3HR and 4HR are respectively equivalent to methods 1, 2, 3 and 4 but for high resolution profiles.

3.6 Problem encountered in Uccle during the year 1990

When Judith Spiegel[9] compared two data sets of the radiosondes profiles in Uccle and Saint-Hubert in 1990 from BADC and from IRM (RMI in English) for her study of scintillation on satellite links she remarked abnormal differences.

Expecting a bias or a problem in an eventual processing of the data from the BADC, we first compared BADC profiles with another source of radiosonde data, the American NOAA website [35]. We did not use this data set previously because BADC data generally contain more levels, even if there are also more

[9]Judith Spiegel works in the Microwave Laboratory of the Université catholique de Louvain (UCL) in Belgium.

outliers. Randomly taking several sites over the world, we compared the heights, the temperatures and dew point temperatures when the pressure levels were identical and we concluded that these values were always identical, even at Uccle or St Hubert.

When we compared the RMI profiles to the ones from BADC, the differences were obvious. At equal pressure levels the values were not strictly the same and the RMI profiles were more detailed.

In our applications, the most important thing was to evaluate the impact on the delay if we chose a data source instead of the other one. As we can notice on the following picture, the mean value of the RMS total difference is below half a centimeter, which is smaller than the measurement uncertainty, so we should not worry about the precision obtained thanks to BADC radiosonde profiles.

We still do not know why the data from RMI and from BADC are different, because it is very improbable that the data come from different balloons (the maximum altitude is always the same in the two data sets). But as RMI data give sharper results on scintillation, we could reasonably assume that the levels from RMI profiles were selected and processed in a different way than for the usual meteorological applications.

3.7 Assessment of the models

Now that the data processing is defined, we are able to compare the models to vertical integration. As far as the wet delay is concerned, the reference value should be the integration of the wet refractivity. The determination of the reference value for the hydrostatic delay is not so clear. Effectively the radiosonde profiles usually stop between 20 and 30 km. A simple vertical integration would neglect the effect of the layers situated above this limit. This assumption is valid for the wet delay but not for the hydrostatic delay. As the best model to calculate the hydrostatic zenith delay is the Saastamoinen model, two solutions are possible: we can use the model for the layers above the highest radiosonde level or we can use the Saastamoinen model alone, without using the vertical integration. Comparisons between the two methods to GPS measurements during GSTB-V1 proved that the second technique was the most accurate.

For our comparisons, we assumed that the equation of the Saastmoinen hydrostatic delay as expressed in the ESA Blind model (with the Rüger k_1 coefficient) was the best one.

In the following table and the ones located in Annex A, we are showing the delay estimation error for 9 different ways to calculate it. The six first ones do not require any additional explanation, they are the Saastamoinen, the Hopfield, the Black and the Askne Nordius models as described in Chapter 2.

The ESA Ground model consists in the use of the equations of the ESA Blind

model used with the real measured (or calculated in the case α and λ) parameters instead of the tabulated ones. This model can be used in order to test the ability of the wet delay equation to model the atmosphere if the real α and λ where available without taking the tabulated ones into account.

The ESA Met model is also derived from the ESA Blind model. For this model, only the surface pressures[10] and temperature are provided from surface measurements. This model simulates the results given by the model using parameters that can be easily measured from a ground station with barometers, thermometers and hygrometers.

For this validation test, we chose to compare the methods for January 2005 for 9 well distributed locations all around the world: Adelaide in Australia, Brasilia in Brazil, Jeddah King Abdul Aziz international airport in Saudi Arabia, Dakar in Senegal, Fairbanks in USA (Alaska), Gibraltar, Pretoria in South Africa, Sapporo in Japan, St-Hubert in Belgium and Vandenberg in USA (California). The choice of the stations and of the period was arbitrary, because we can not be exhaustive with such an amount of data. The values in the tables represent the bias and the rms error associated to the model during the month. Next to the name of the station the number of acceptable profiles have been considered for the mean. Only the table for Pretoria is reported here but the results for this site are representative. The other tables are located in Annex A.

First of all, we can notice that the errors are most of the time below 10 cm. Even if the main part of the delay is due to the hydrostatic part, we can see that the error is mainly due to the wet part. The RTCA and Saastamoinen models give the worst values, going up to a 16 cm rms error in Dakar and Pretoria respectively. We can notice that the best models are Askne-Nordius'one and ESA Ground with an rms value below 5 mm. Their results are very close because the models are very similar. This shows that a good estimation of the λ parameter (and of α to a lesser extend) is essential for calculating the delay.

Among the models only using surface data (and not α nor λ), the ESA Met model is the most accurate one. The Hopfield model is particularly bad for the hydrostatic delay. If a Hopfield-like model is chosen, the Black hydrostatic delay should be preferred. The poor results of the Black model are explained by the fact that it does not provide an effective model of the wet delay. Among the blind models, we can clearly notice the improvement brought by the ESA Blind model. The bias of this model is often below 1 cm and the rms error is below 3 cm. Nevertheless this error can go up to 9 cm in Dakar. Generally the ESA Met model is more precise than the Blind model, but the improvement is not spectacular (often around 0,5 cm). This analysis gives us a first idea of the order of magnitude of the errors and of the respective behaviour of the models. The numbers provided here are quite similar to the one found for GSTB-V1.

[10]The total pressure and the water vapor pressure.

Pretoria (S.Afr.)	55 profiles								
Mean error [cm]	Saastamoinen	Hopfield	Black	Askne-Nordius	RTCA	ESA Blind	ESA Ground	ESA Met	Integration
Total delay	-14.9571	1.4004	4.8649	-0.1190	4.5411	2.3189	0.1109	-2.1892	0.7663
Hydrostatic delay	-0.3969	4.3180	0.1301	0.0458	0.2130	0.0165	0	0	0.7663
Wet delay	-14.5602	-2.9176	4.7348	-0.1648	4.3280	2.3024	0.1109	-2.1892	0
RMS error [cm]									
Total delay	15.6749	3.8372	5.8241	0.3032	5.5933	3.8047	0.2743	4.5980	0.7708
Hydrostatic delay	0.3969	4.3338	0.1355	0.0458	0.5866	0.5545	0	0	0.7708
Wet delay	15.2966	4.8110	5.7019	0.3239	5.3673	3.7199	0.2743	4.5980	0

Chapter 4

Assessment of the models with Numerical Weather Prediction maps

4.1 Introduction

The second part of our analysis concerns Numerical Weather Prediction data. Oppositely to radiosonde profiles, NWP maps provide the state of the atmosphere worldwide, including the oceans. The main drawback is the low resolution of the maps. Vertically, the profiles are composed of only 23 levels (considering mean sea level and surface) and the vertical resolution is 1° in latitude and longitude. Note also that these maps are issued from an assimilation process and not from direct measurements. For example, we have to remain conscious that we can not expect the same precision from a NWP profile over the Indian ocean and a radiosonde profile in England. The temporal resolution is 6 hours. This is better than standard radiosonde profiles for which the launches typically occur every 12 hours. But this is still above the temporal scale of the evolution of the water vapor contend (typically 30 minutes only).

As it was explained in section (2.1.2.2), the parameters included in the ESA Blind model come from ECMWF's ERA15 re-analysis. In order to provide a sufficiently independent database, we used for this validation another set of NWP, the ECMWF PDS data that ESA used in 2002 to calibrate Envisat's RA2 radar altimeter[1]. This data set concerns a year that was not included in ERA15, has a better spatial resolution (ERA15 was $1{,}5^{\circ}$ in latitude and longitude) and is issued from slightly different assimilation procedures. The ERA15 data set came from a re-analysis exercise, re-calculating NWP maps with state-of-the-art procedures. The data set that we used was created directly, day after day, for operational purposes (essentially weather forecast). The concerned period began on 24th

[1]The data set comes from the Ra2 CalVal campaign that took place in the Balearic Islands in 2002 (see [30]).

March 2002 at 18:00 and ended on 24th October 2002. Samples are missing from 18 th July at 18:00 to 21 th July 12:00. Altogether we have 859 samples, as we have 4 samples (at midnight, 6 o'clock, noon and at 18 o'clock) per day.

The original data contain for each sample: geopotential profiles, temperature profiles and relative humidity profiles for fixed pressure levels from 1000 hPa to 1 hPa[2], plus the mean sea level pressure and the surface pressure.

As far as the integration of the delay is concerned, we need the altitude of the levels instead of the geopotential. As it is described in the next section, the routine employed previously to convert one quantity to the other has been analysed and has been compared to some others. Finally an improved one has been proposed and has been implemented.

Another problem came from the fact that only the pressure at surface was known and we had to interpolate or extrapolate the other parameters. Section 4.3 will be devoted to these issues.

Two model performances comparisons have been performed for these NWP maps, one comparing delays at surface and one comparing delays at an altitude of 5 km. This last analysis requires the knowledge of the pressure at this level and we will see in section 4.4 how to deal with that problem.

Finally, the last section of this chapter is devoted to the analysis of the performances of the different models on a global scale.

4.2 From geopotential to altitude

4.2.1 Definitions

The definition of the geopotential gives:

$$d\phi = g\, dz$$

where $d\phi$ is the increment of geopotential in m^2/s^2, g is the acceleration of gravity in m/s^2 and dz is the increment of heights in m. The value of the acceleration of gravity depends on the position of the Earth where it is measured. We can model it with a good approximation just by taking in account latitude and height. For the latitude dependence the World Meteorological Organisation recommends the formula at mean sea level:

$$\begin{aligned} g_{msl}(lat) &= 9,806.(1 - 2,637\, 10^{-3} \cos(2.lat)) \\ &= P_0 \end{aligned}$$

[2]The 21 fixed pressure levels are 1000, 925, 850, 700, 500, 400, 300, 250, 200, 150, 100, 70, 50, 30, 20, 10, 7, 5, 3, 2 and 1 hPa.

For the height dependence, we have two solutions. First of all we can follow the recommendation of the WMO

$$\begin{aligned} g(lat,z) &= g_{msl}(lat) - 9,806.\left(3,1.10^{-7}z\right) \\ &= P_0 - P_1 z \end{aligned} \tag{4.1}$$

The other solution would be to remember that the gravitational force at sea level is equal to$F_{grav} = G\frac{Mm}{R^2} = g_{msl}m$ where R and M are respectively the radius and the mass of the Earth and G is the Cavendish constant. From that law we can deduce a quadratic relation:

$$g = g_{msl}(R/R+z)^2 \tag{4.2}$$

The mean radius of the Earth is equal to 6371,03 km. If we need more precision we can assume a sinusoidal decrease of the radius as we move from the equator (where the radius is 6378,16 km) to the pole (the polar radius is equal to 6356,78 km):

$$R = 6378,16 - 21,38\sin(lat)^2$$

4.2.2 Review of the formulae

Several approximations have been evaluated in order to calculate the altitude as a function of the geopotential.

The first approximation considered is rather rough and consists in dividing the geopotential by the acceleration of gravity at the center of gravity of the air column.

$$Z = \frac{\phi}{g_m} \tag{4.3}$$

Another approach would be to divide the geopotential by the acceleration of gravity at mean sea level.

$$Z = \frac{\phi}{g(lat,0)} \tag{4.4}$$

A third solution would be to calculate the ratio between the geopotential and the acceleration of gravity at the point considered using the WMO formula:

$$\begin{aligned} Z &= \frac{\phi}{g(lat,Z)} \\ &= \frac{\phi}{P_0 - P_1 Z} \\ \Rightarrow 0 &= P_1 Z^2 - P_0 Z + \phi \\ \Rightarrow Z &= \frac{P_0}{2P_1} \pm \sqrt{\left(\frac{P_0}{2P_1}\right)^2 - \frac{\phi}{P_1}} \end{aligned} \tag{4.5}$$

Only the solution with the minus sign should be kept.

A very similar approach could be adopted, but considering the quadratic relation for g:

$$\begin{aligned} Z &= \frac{\phi}{g(lat, Z)} \\ &= \frac{\phi}{P_0(R/R+z)^2} \\ \Rightarrow 0 &= \phi Z^2 + \left(2R\phi - R^2 P_0\right) Z + \phi R^2 \\ \Rightarrow Z &= \frac{-2R\phi + P_0 R^2 \pm \sqrt{R^4 P_0^2 - 4R^3 \phi P_0}}{2\phi} \end{aligned} \tag{4.6}$$

for geopotentials greater than 0, the minus sign should be taken and for negative geopotentials the plus sign should be considered.

Nevertheless the best solutions remain the calculation of the integral taking into account either the WMO formula or the relation deduced from the definition of the acceleration of gravity.

Following the first solution we have:

$$\begin{aligned} \phi(Z) &= \int_0^Z (P_0 - P_1 z) dz \\ &= P_0 Z - P_1 \frac{Z^2}{2} \end{aligned}$$

By reversing the equation we obtain:

$$\begin{aligned} 0 &= -\frac{Z^2}{2} P_1 + P_0 Z - \phi \\ \Rightarrow Z &= \frac{P_0}{P_1} \pm \sqrt{\left(\frac{P_0}{P_1}\right)^2 - \frac{2\phi}{P_1}} \end{aligned} \tag{4.7}$$

And in fact only the solution with the minus sign should be kept.

If we integrate the formula (4.2) in order to calculate the geopotential we get:

$$\begin{aligned} \phi(Z) &= \int_0^Z g_{msl} \left(\frac{R}{R+Z}\right)^2 dz \\ &= g_{msl} R^2 \int_0^Z \frac{dz}{(R+Z)^2} \\ &= g_{msl} R^2 \int_R^{R+Z} \frac{da}{a^2} \\ &= g_{msl} R^2 \left[-\frac{1}{a}\right]_R^{R+Z} \end{aligned}$$

$$
\begin{aligned}
&= g_{msl} R^2 \frac{R + Z - R}{R(R + Z)} \\
&= g_{msl} R \frac{Z}{R + Z}
\end{aligned}
$$

It is now easy to express the altitude above mean sea level as a function of the geopotential:

$$
\begin{aligned}
\phi R + \phi Z &= g_{msl} R Z \\
\Rightarrow Z &= \frac{\phi R}{g_{msl} R - \phi}
\end{aligned}
\tag{4.8}
$$

4.2.3 Conclusions

In order to compare the different formulas we plotted the relative error for each method as a function of the altitude above sea level, taking as a reference the formula (4.8). We chose to consider this value as the correct one because it is the one for which the lesser assumptions are performed.

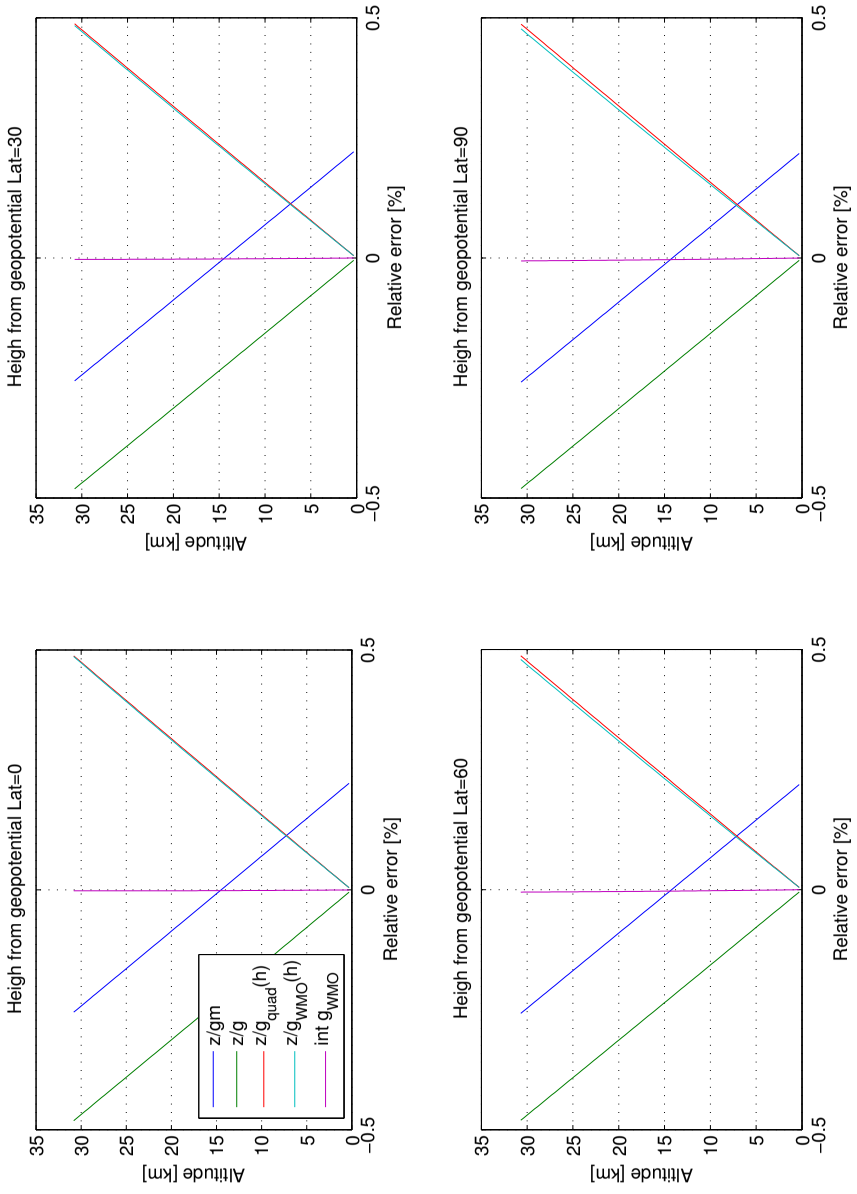

Figure 4.1: Graphic of the relative error in altitude as a function of the altitude. The reference relation is equation (4.8) The blue curve is related to equation (4.3), the green one to equation (4.4), the red one to equation (4.5), the cyan one to equation (4.6) and the purple one to equation (4.7).

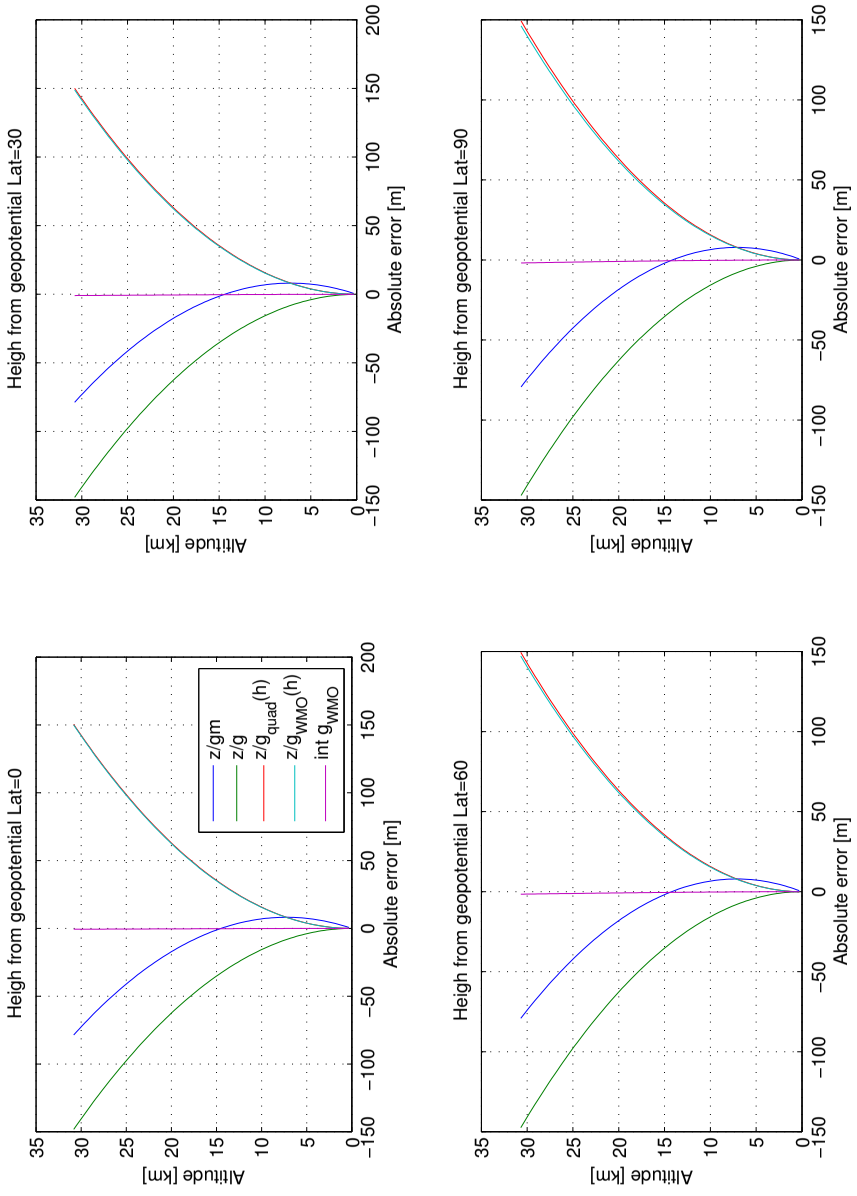

Figure 4.2: Graphic of the absolute error as a function of the altitude. The reference relation is equation (4.8) The blue curve is related to equation (4.3), the green one to equation (4.4), the red one to equation (4.5), the cyan one to equation (4.6) and the purple one to equation (4.7).

We can see that the relative error is relatively low even for the rougher approximations: the maximal difference at an altitude of 30 km is only around 0,5%.

We can also notice that when g is taken at sea level, the altitude is underevaluated. When g is taken at the considered point the altitude is logically overestimated. The similarity of the results, using either the WMO formula or the quadratic one is remarkable. Finally, we can see that the latitude does not influence the conclusions on the methods to be applied.

Even if the error should not be important whatever the equation in use would be, it is recommended to use one of the two formulas deduced from the integration (i.e. equations (4.7) or (4.8)).

4.3 Surface height retrieval

For this data set, ECMWF does not provide the surface geopotential, so that we cannot apply the same procedure as above. If the surface pressure is under 1000 hPa, the altitude could be recovered by interpolation. If surface pressure is comprised between 1000 hPa and mean sea level pressure, interpolation can also be applied. But we have to keep in mind that, in both cases, the higher pressure value is already an extrapolated one. For the model contained into the data, there is always a level at 1000 hPa: if the real surface pressure is 980 hPa, the point associated to the pressure level 1000 hPa would be underground. If the surface pressure is above mean sea level pressure and 1000 hPa, an extrapolation of the surface height has to be performed.

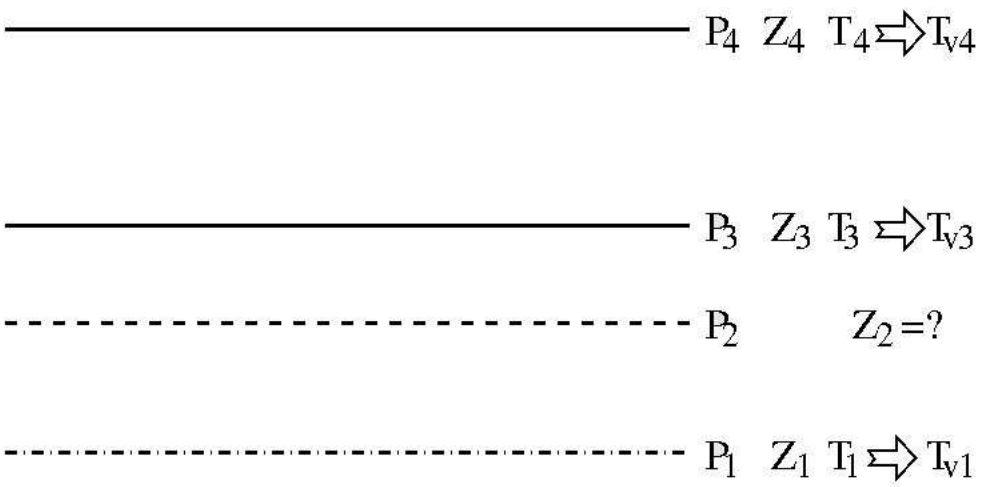

Figure 4.3: Schema of the levels. We are looking for the altitude Z_2 linked to level 2. In our tests, level 1 is available when we consider interpolation but not when we consider extrapolation.

As a first attempt a simple purely mathematical interpolation/extrapolation law was considered. The idea was simply to relate linearly the height with the logarithm of the pressure. Unfortunately the altitude was varying a lot from one day to another because this method was not precise enough. We tried to rely on the pressure scale height rather than on extrapolation, as the hydrostatic equilibrium can be expressed as:

$$\frac{dp}{p} = -\frac{dz}{H}$$

where H is the scale height calculated from linear fitting, but the results were even worse.

A review of different techniques and formulas has been performed and they have been assessed against radiosonde profiles in order to chose the best one.

4.3.1 Review of the formulae

4.3.1.1 Interpolation

- Linear interpolation:

$$Z_2 = Z_3 - (Z_3 - Z_1)\frac{\ln\left(\frac{P_2}{P_3}\right)}{\ln\left(\frac{P_1}{P_3}\right)} \tag{4.9}$$

- Deduction from H_3 and "sea" level:

$$Z_2 = Z_3 - H_3 \ln\left(\frac{P_1}{P_2}\right) \tag{4.10}$$

with H_3 is the pressure scale height coming from a linear fitting using only the levels above level 2.

- Deduction from H_1 and "sea" level:

$$Z_2 = Z_3 - H_0 \ln\left(\frac{P_1}{P_2}\right) \tag{4.11}$$

with H_0 is the pressure scale height coming from a linear fitting using all the levels but level 2 (the unknown).

- Formula deduced from integration of the hydrostatic equilibrium and assuming a linear relationship between the virtual temperature and the logarithm of the pressure:

$$Z_2 = Z_1 + \frac{R_d}{g}\left(T_{v1} \ln\left(\frac{P_1}{P_2}\right) - \frac{1}{2}\frac{T_{v3} - T_{v1}}{\ln\left(\frac{P_3}{P_2}\right)} \ln^2\left(\frac{P_2}{P_1}\right)\right) \tag{4.12}$$

This formula can also be considered using the "normal temperature" instead of the virtual temperature.

- By reversing the equation $P_2 = P_1\left(1 - \frac{\alpha(Z_2 - Z_1)}{T_1}\right)^{\frac{g}{R_d'^{\alpha}}}$ found in the Galileo Reference Troposphere ([**?**]), we obtain

$$Z_2 = Z_1 + \left(1 - \left(\frac{P_2}{P_1}\right)^{\frac{\alpha R_d}{1000g}}\right)\frac{T_1}{\alpha} \tag{4.13}$$

α can be calculated from linear fitting or from $\alpha = -\frac{T_1 - T_3}{Z_1 - Z_3}$.

- An analog approach, using the temperature lapse rate, can be followed from the formula $T_2 = T_S\left(\frac{P_2}{P_1}\right)^{\frac{\alpha R_d}{g_m}}$ from Askne-Nordius ([3, **?**]):

$$Z_2 = Z_1 + \frac{T_1}{\alpha}\left(\frac{1}{P_1}\right)^{\frac{\alpha R_d}{1000 g_m}}\left(P_1^{\frac{\alpha R_d}{1000 g_m}} - P_2^{\frac{\alpha R_d}{1000 g_m}}\right) \tag{4.14}$$

4.3.1.2 Extrapolation

- Linear extrapolation

$$Z_2 = Z_3 - (Z_3 - Z_4)\frac{\ln\left(\frac{P_2}{P_3}\right)}{\ln\left(\frac{P_4}{P_3}\right)} \tag{4.15}$$

- Deduction from H_3 and the first level above level 2

$$Z_2 = Z_3 + H_3 \ln\left(\frac{P_3}{P_2}\right) \tag{4.16}$$

- Formula deduced from integration of the hydrostatic equilibrium and assuming a linear relationship between the virtual temperature and the logarithm of the pressure, but using only levels 3 and 4:

$$Z_2 = Z_3 + \frac{R_d}{g}\left(T_{v3}\ln\left(\frac{P_3}{P_2}\right) - \frac{1}{2}\frac{T_{v4} - T_{v3}}{\ln\left(\frac{P_4}{P_3}\right)}\ln^2\left(\frac{P_2}{P_3}\right)\right) \tag{4.17}$$

  As in equation (4.12), we could also use the temperature instead of the virtual temperature.

- By using the equation found in the Galileo Reference Troposphere ([?]), we obtain

$$Z_2 = Z_3 + \left(1 - \left(\frac{P_2}{P_3}\right)^{\frac{\alpha R_d}{1000g}}\right)\frac{T_3}{\alpha} \tag{4.18}$$

  α can be calculated from linear fitting or from $\alpha = -\frac{T_1 - T_3}{Z_1 - Z_3}$.

4.3.2 Results

In order to assess these equations we compared their precision using radiosonde profiles. Concerning interpolation, we tried to compare the behaviour of the equations in a realistic case. A set of 16 randomly selected profiles was chosen so that there was always at least one level between 1000 hPa and 925 hPa. If more than one level was comprised between these two values, one of them was randomly selected. The idea was to compare the altitude provided by the tested formulas to the one available in the profiles for this level.

The scenario proposed to test the extrapolation formulas is very similar: we tried to evaluate the altitude at the same level as before, but only thanks to the 925 hPa level and the following one.

4.3.2.1 Interpolation

In the following graph the errors of the equation for the interpolation are compared. On the left there are the mean, the standard deviation and the root mean square error of the absolute error and on the right there are the same graphs for the relative error. Only the best formulae have been kept for this graph.

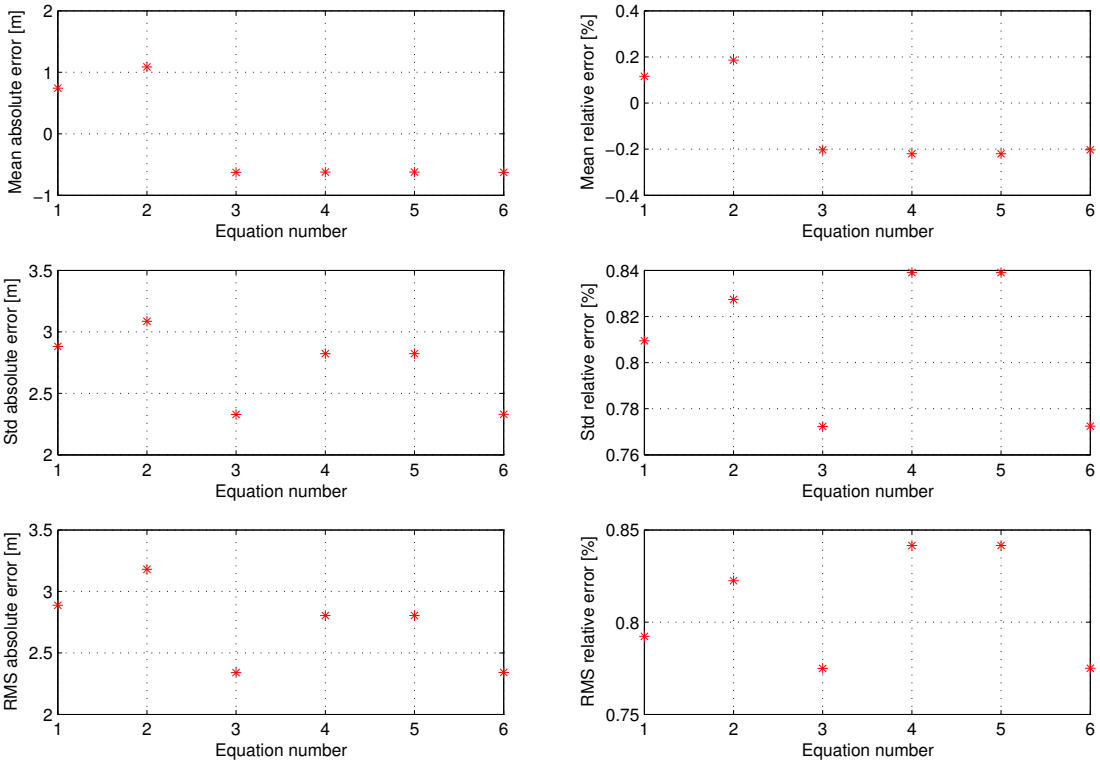

Figure 4.4: Graph of the absolute and the relative errors of the altitude calculated by the interpolation equation. Equation 1 corresponds to formula (4.9), equation 2 corresponds to formula (4.12) using the virtual temperature, equation 3 corresponds to formula (4.12) using the temperature, equation 4 corresponds to formula (4.14) using α from linear fitting, equation 5 corresponds to formula (4.13) using α from linear fitting and equation 6 corresponds to formula (4.13) using α calculated locally.

No formulas based on the scale height are represented on the graph because they were not accurate enough. The scale height can also be expressed as:

Figure 4.5: Graphic of the pressure scale height as a function of the altitude for

$$H = \frac{kT}{mg}$$

where k is the Boltzmann constant, T is the temperature and mg is the mean weight of an air particle. As we can observe on figure (4.5), this quantity is not constant all over the profile. In fact, a linear relationship between the logarithm of the pressure and the altitude can only be rigorously assumed for an isothermal atmosphere. That is the reason why these methods gave very poor results.

The best results come from (4.12) and (4.13) with α calculated locally. Their rms error is below 2,5 m and the bias stays below 1 m. We chose to implement the first one.

4.3.2.2 Extrapolation

As far as the extrapolation equations are concerned, a graph similar to the one for interpolation is provided. Here again, only the best results are considered.

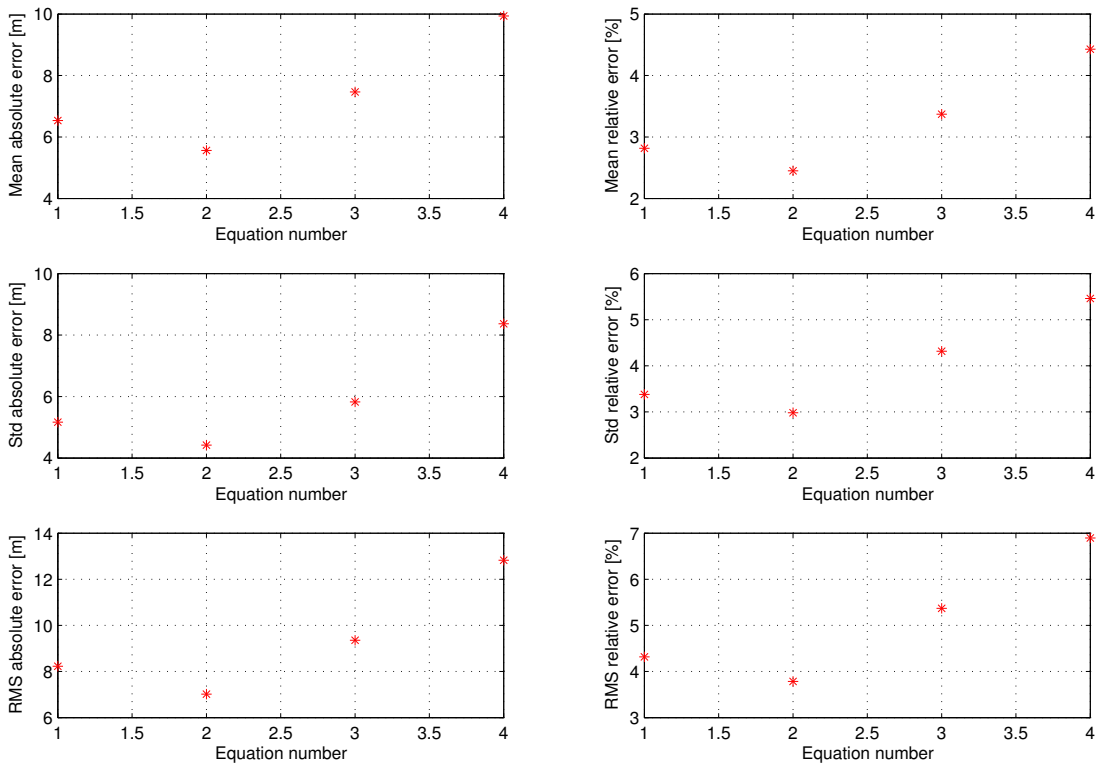

Figure 4.6: Graph of the absolute and the relative errors of the altitude calculated by the extrapolation equations. Equation 1 corresponds to formula (4.15), equation 2 corresponds to formula (4.17) using the virtual temperature, equation 3 corresponds to formula (4.17) using the temperature, equation 4 corresponds to formula (4.18) using α calculated locally.

We can observe that the best method is the (4.17) formula with the virtual temperature. Unfortunately this equation requires the virtual temperature at mean sea level, which has to be extrapolated too. For this reason we chose to implement formula (4.15) which provides a similar accuracy (rms around 8 meters and a bias around 6 meters).

4.3.2.3 Additional considerations for extrapolation

We have seen that for extrapolation, the best formula was equation (4.15). For a better accuracy in the extrapolation, we use the mean sea level pressure (where altitude is equal to zero) and the altitude associated with level 1000 hPa. Nevertheless we have to be careful because sometimes mean sea level pressure can be so

close to 1000 hPa that the extrapolated altitude is doubtful for numerical reasons. A detailed calculation of the error has been performed, but lead to a formula that was too complex to implement. Instead, we chose a more conservative but simpler approach. If $|P_{msl} - 1000| < 1hPa$, then the altitude of level 925 hPa is used for the extrapolation.

4.4 Water vapor pressure and temperature recovery

Concerning interpolation, these two parameter are computed by assuming a linear relationship between these quantities and the logarithm of the pressure. This is equivalent to assuming a linear law between the water vapor pressure (or the temperature) and the altitude.

As far as the extrapolation was concerned, the water vapor pressure was derived from the λ parameter:

$$e_0 = e_1 \left(\frac{p_0}{p_1} \right)^{\lambda}$$

It may happen that for some reasons, the computed λ adopts particularly high or low values. In these case, we considered that the extrapolation was not accurate enough and if $-0,75 > \lambda$ or $\lambda > 7,5$, we assigned a Not-a-Number value to the water vapor pressure.

The surface temperature is computed by means of:

$$T_0 = T_1 - \alpha(h_0 - h_1)$$

4.5 Pressure recovery

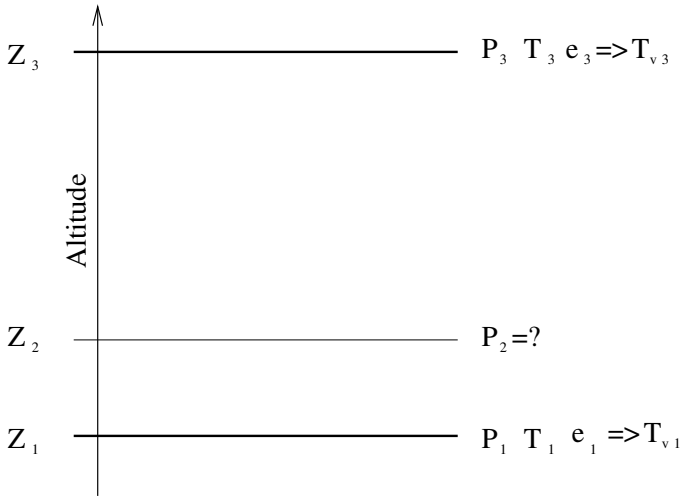

Figure 4.7: Schema of the levels

Starting from the equation

$$Z_2 = Z_1 + \frac{R_d}{g}\left(T_{v1}\ln\frac{P_1}{P_2} - 0,5\frac{T_{v3}-T_{v1}}{\ln\frac{P_3}{P_1}}\ln^2\frac{P_2}{P_1}\right) \tag{4.19}$$

we can deduce

$$\ln P_2 = \frac{-D \pm \sqrt{D^2 - 4BC}}{2B} \tag{4.20}$$

with

$$\begin{aligned} A &= (Z_2 - Z_1)\frac{g}{R_d} - T_{v1}\ln P_1 \\ B &= 0,5\frac{T_{v3}-T_{v1}}{\ln\frac{P_3}{P_1}} \\ C &= A + B\ln^2 P_1 \\ D &= T_{v1} - 2B\ln P_1 \end{aligned}$$

In the equation (4.20), the positive sign should be considered if $T_{v1} > T_{v3}$ and the negative sign has to be used in the other case. Gathering all the terms, we finally obtain (with the same sign convention sign):

$$P_2 = \exp\left(-T_{v1}\frac{\ln\frac{P_3}{P_1}}{T_{v3}-T_{v1}} + \ln P_1 \pm\sqrt{\left(T_{v1}\frac{\ln\frac{P_3}{P_1}}{T_{v3}-T_{v1}} - \ln P_1\right)^2 - 2\frac{\ln\frac{P_3}{P_1}}{T_{v3}-T_{v1}}\left((Z_2-Z_1)\frac{g}{R_d} - T_{v1}\ln P_1)\right) - \ln^2 P_1}\right)$$

If $T_{v1} = T_{v3}$, this equation would lead to a division by zero. In this case we have to consider this equation:

$$P_2 = \exp\left(\ln P_1 + \frac{T_{v1}g}{R_d}(Z_1 - Z_2)\right)$$

This equation was tested in Matlab on radiosonde profiles in Lima Airport (18/03/99 at 16:00), Gibraltar (1/12/01 at 12:00) and Sodankyla (14/07/03 at 11:00). The test consisted in the recovery of the pressure for the closest level to 5000 m using the information related to the superior and inferior levels. The difference between the calculated pressure and the measured one was below 0,4 hPa in each case.

The number of samples is quite low, but the values found are far under the pressure accuracy of radiosonde data (typically1 hPa), so we can consider this result satisfying.

4.6 Analysis of the data

As we already mentioned it, this data set is composed of world maps of the atmospheric profiles, so it will be used to compare the models on a world basis. The data presented here are mainly maps presenting for each point a statistical parameter calculated over the 7 months of data. This statistical parameter can be the mean difference, the root mean square (rms) difference or the standard deviation of the difference between the delay calculated from the model and the reference delay.

Tables of statistics for each model are also presented. They represent the temporal mean of the statistics calculated for each sample map. For each sample (for example the 25/05/2002 at 6:00), a spatial mean of the total delay deviation of all the points of the map is computed, as well as other statistical parameters (means, rms and maximal deviations for all the delays). Then a temporal mean of all these parameters is calculated.

Similarly to the radiosonde data analysis, the reference zenith wet delay is computed from vertical integration and the reference hydrostatic delay is obtained by means of the Saastamoinen model (with Rüger's set of coefficients). Nevertheless,

[cm]	Total delay	Hydrostatic delay	Wet delay
Mean	-3.1218860e+000	-3.4799148e+000	3.5802880e-001
Rms	5.9663469e+000	4.1837065e+000	4.3389151e+000
Min	-2.2490903e+001	-9.6532344e+000	-1.6384951e+001
Max	1.5843509e+001	5.7844978e-001	2.4615407e+001

Table 4.1: Table of the Hopfield's model statistics.

when we compared the integrated hydrostatic delay to the reference one, we found that the mean differences were below 10^{-6}cm and the rms differences were below 10^{-5} cm.

As the Black model does not provide any solution for the wet delay, we discarded it from this analysis. The Askne-Nordius was not tested neither because it has no practical application and it is too similar to the ESA Ground model[3].

We made two types of delay comparison: one to compare the performances of the model at surface and one at 5000. This second one could simulate the delay calculated for a landing plane for example. The second test possesses the advantage of being free of orographic problems.

4.6.1 Delay at surface

4.6.1.1 Models based on surface measurements

The three models that are only based on ground measurements are Hopfield's one, Saastamoinen's one and ESA Met. A first look at the maps shows that the major problem are located at the equatorial belt. The worst results come from the Hopfield model with a maximal rms value around 16 cm and rms values over 12 cm over South-East Asia, over Indian Ocean and over Pacific Ocean. The poor performances of the Hopfield model for the total delay come essentially from a large error in the calculation of the hydrostatic delay. This error introduces an underestimation bias approximately equal to 3.1 cm. The white points on the map correspond to Not-a-Number values for the water vapor pressure. The same mask has been applied to the hydrostatic delay.

Concerning the Saastamoinen error, the hydrostatic errors (in the order of 0,24 cm) is only due to the wrong choice of the k_1 coefficient. The wet delay error is very similar to Hopfield's one.

As far as the ESA Met hydrostatic delay is concerned, the equation used is the reference one, so the total delay deviation comes only from the wet delay.

[3]Just for remainder, the ESA Ground model consists in the ESA Blind model equations, but all the input parameters are deduced from the real state of the atmosphere instead of tabulated coefficients.

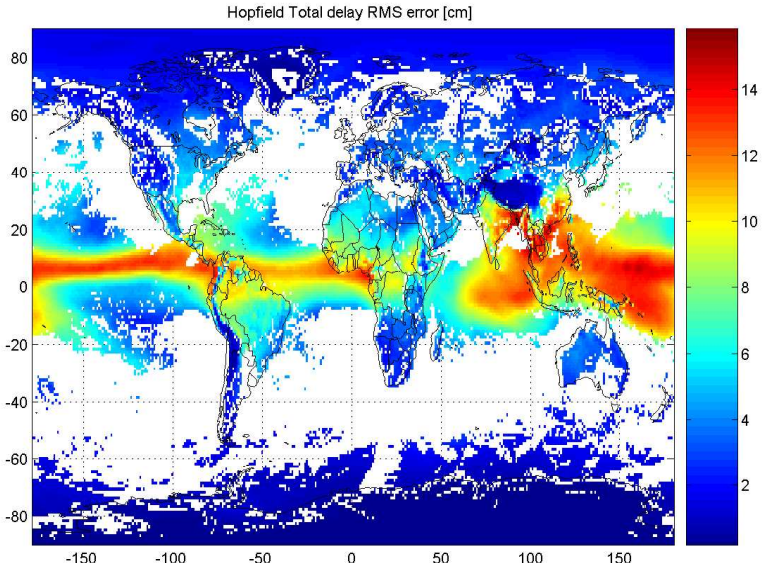

Figure 4.8: Map of the rms deviation of the Hopfield total delay.

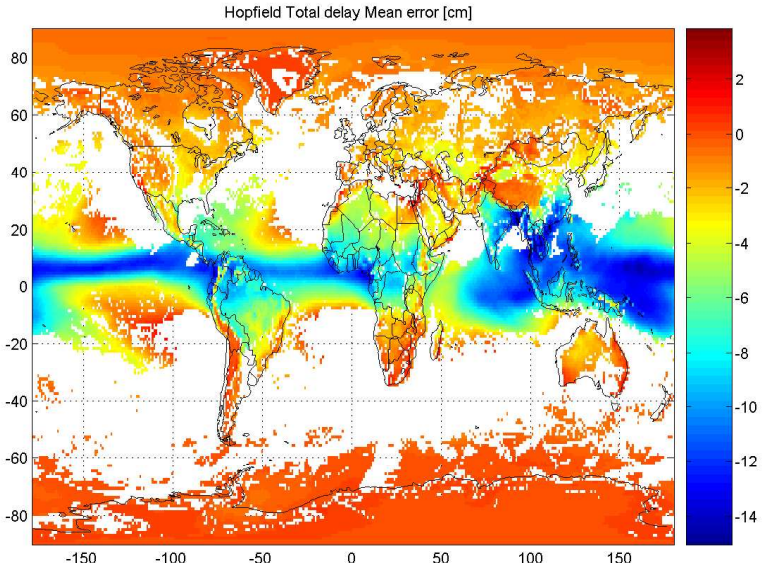

Figure 4.9: Map of the mean deviation of the Hopfield total delay.

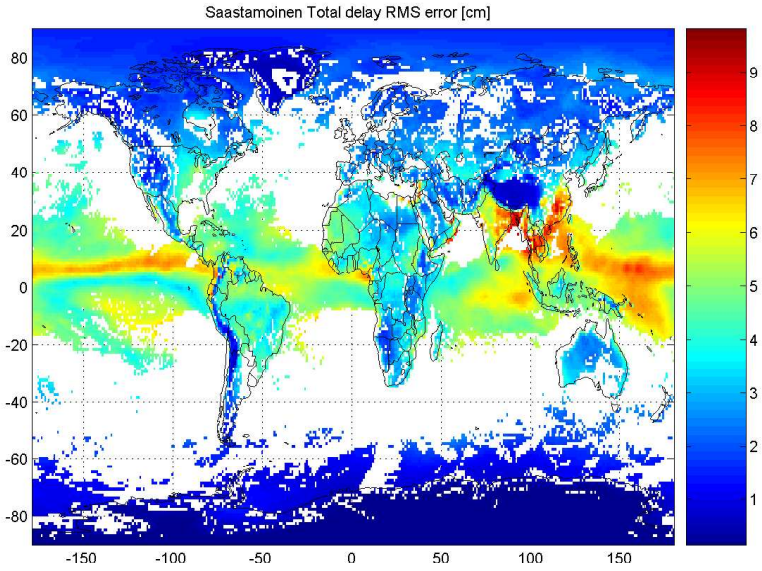

Figure 4.10: Map of the rms deviation of the Saastamoinen total delay.

[cm]	Total delay	Hydrostatic delay	Wet delay
Mean	2.4335710e-001	2.3866881e-001	7.3416855e-003
Rms	4.2828438e+000	2.3969729e-001	4.2748827e+000
Min	-1.6510622e+001	1.0725041e-001	-1.6754679e+001
Max	2.5437368e+001	2.5227167e-001	2.5193381e+001

Table 4.2: Table of the Saastamoinen's model statistics.

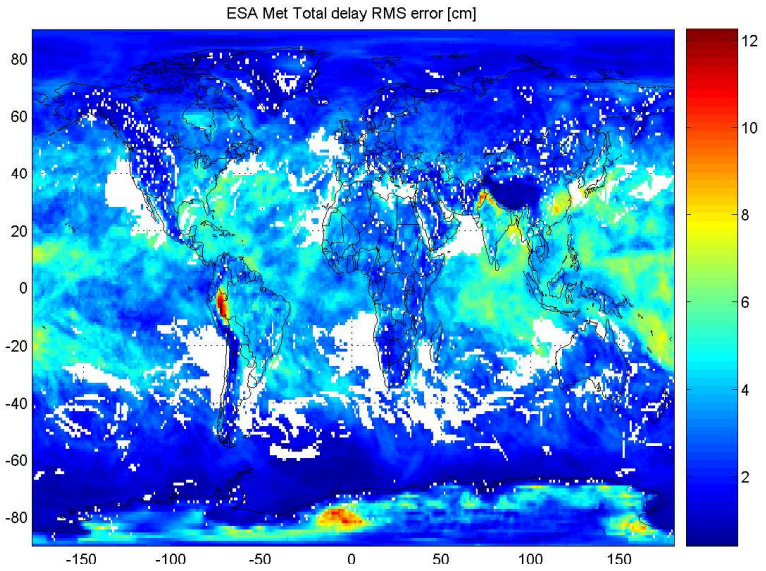

Figure 4.11: Map of the rms deviation of the ESA Met total delay.

[cm]	Total delay	Hydrostatic delay	Wet delay
Mean	-3.5862106e-001	1.3276368e-002	-3.7171406e-001
Rms	3.6328591e+000	1.5593134e-002	3.6348861e+000
Min	-1.7409586e+001	-4.9707719e-003	-1.7426489e+001
Max	2.1532957e+001	2.2914273e-002	2.1524922e+001

Table 4.3: Table of the ESA Met model statistics.

The performances of the wet delay are globally better than the previous ones, but there are some hot-spots. The decrease of the global error is not obvious when looking at the maps because the color scale is not the same, but by comparing the wet rms error in tables 4.2 and 4.3 we can notice that the values went from 4,3 cm to 3,6 cm. The overall improvement is due to a better approximation of the temperature and the water vapor pressure profiles: in the ESA Met the α and λ coefficients depend on the location, on the date of the year and on the hour of the day. Nevertheless, there are regions where this model gives very bad results, like at the frontier between Brazil and Peru, in the Himalaya or in Antarctica. A more in depth study should be performed in order to determine the origin these errors.

4.6.1.2 Blind models

We will continue our comparisons with the blind models. We can notice that this model has a largest deviation than surface models. For example the overall rms error is around 6,6 cm and the maximum rms can exceed 15 cm over the Persian Gulf and along the western coasts of South America and Africa. The error is also higher than 10 cm along the US west coast, above the Sahara desert, in the South-East Asia region, over Australia and to a lesser extend over the Pacific Ocean. The origin of these error is the wet delay computation. The Antarctic Ocean is characterised with a high error as well, but this error is mainly due to errors in the hydrostatic delay estimation.

We can note from table 4.4 than this model has an overall bias of 1,7 cm, which means that this model slightly overestimates the delay (the wet delay in particular).

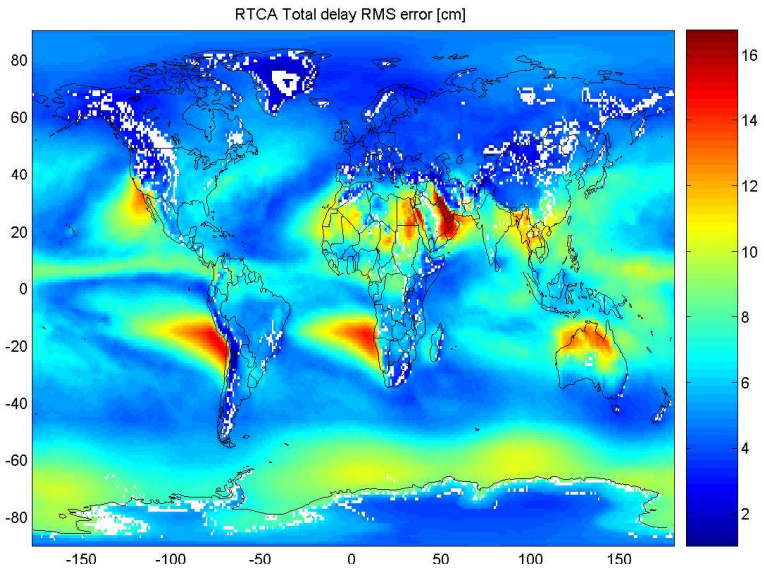

Figure 4.12: Map of the rms deviation of the RTCA model total delay.

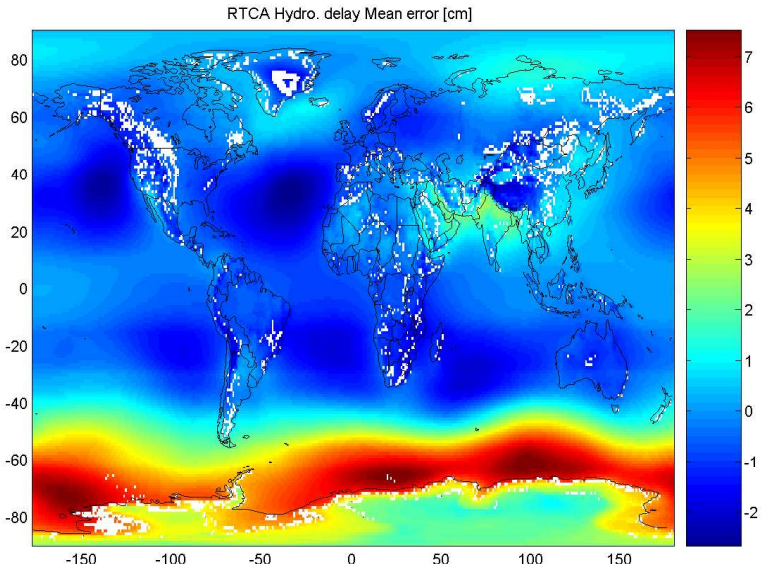

Figure 4.13: Map of the mean deviation of the RTCA model hydrostatic delay.

[cm]	Total delay	Hydrostatic delay	Wet delay
Mean	1.6953831e+000	2.0593932e-001	1.4894438e+000
Rms	6.6200313e+000	2.4747382e+000	6.4181380e+000
Min	-2.0055026e+001	-5.0998730e+000	-2.1689089e+001
Max	2.1321161e+001	1.4587972e+001	2.0599500e+001

Table 4.4: Table of the RTCA model statistics.

When comparing the rms map of the RTCA model with the ESA Blind one, and particularly when we look at the colorbar, we notice a general decrease of the error. This is especially obvious along the South American and the African western coasts. Comparing the statistic tables, we can see that the overall rms total delay error went from 6.6 cm to 4.5 cm with the ESA Blind model. Additionally, the overall bias is now below 0,9 cm (the RTCA overall bias was 1,6 cm). If we compare the performances of the hydrostatic delays (figures 4.13 and 4.15), we can see that the hydrostatic deviation has been divided by two, but there is a major problem over Antarctica. Nevertheless, we can consider that the ESA Blind model for the hydrostatic delay generally leads to an error below 2 cm.

As this model will be the one used in Galileo receivers, we paid a particular attention to the analysis of the remaining errors. The purpose of this study is to distinguish the effect due to the model and to the tabulated parameters from the

effects due to the processing of the NWP data (a wrong recovery of the orography has an effect on the seeming hydrostatic delay error) or from the effects due to the particular climatic conditions of the year of interest. In order to evaluate the performances of the physical model and of the table, we tested different models going from the ESA Ground model presented in chapter 3 to the ESA "Met without temperature" model, which consists in using the tabulated coefficients of the blind model excepted for total pressure and water vapor pressure. The next section is devoted to the description of these models and the the explanation of the results. Nevertheless, if we look at the maps of the rms deviation of the ERA 15 observations from the harmonic model (in the Annex B), we can easily understand the origin of some poor results in some particular areas. For example, the model does not perform perfectly in the center of Africa because the water vapor pressure and the total pressure can not be well represented by an harmonic function.

As far as these climatic conditions are concerned, we found that 2002 was an El-Niño year. As we can see on figure (4.18), this phenomenon is characterised by an increase of the water temperature in the middle of the Pacific Ocean and by a decrease of the water temperature on the western part of the Pacific Ocean. The increase of temperature leads to a higher evaporation rate, and thus to a higher water vapor contend of the air column (of course, the decrease of temperature has exactly the opposite effect). This could explain why both blind models underestimate the wet delay over the Pacific Ocean and overestimate it over Indonesia and Australia. The El-Niño event induces error in the wet delay estimation of the the surface models as well. This is probably due to a mis-modeling of the water pressure profile over these regions of high evaporation rate.

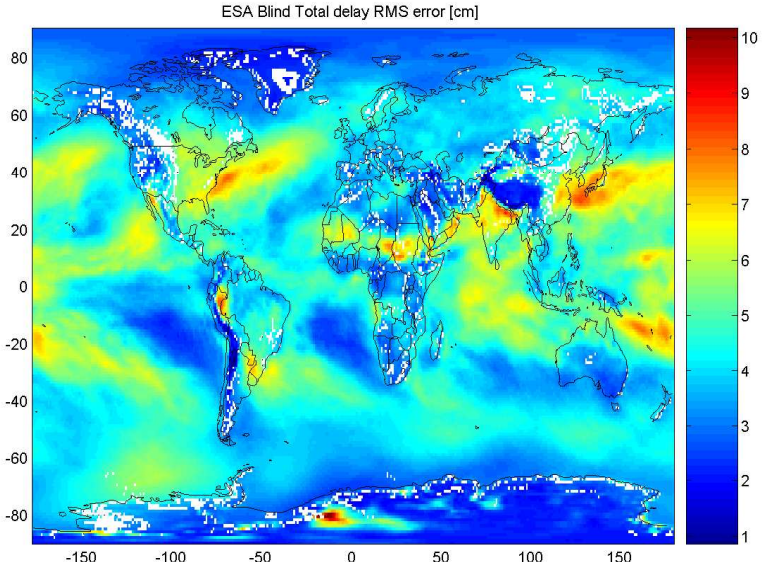

Figure 4.14: Map of the rms deviation of the ESA Blind total delay.

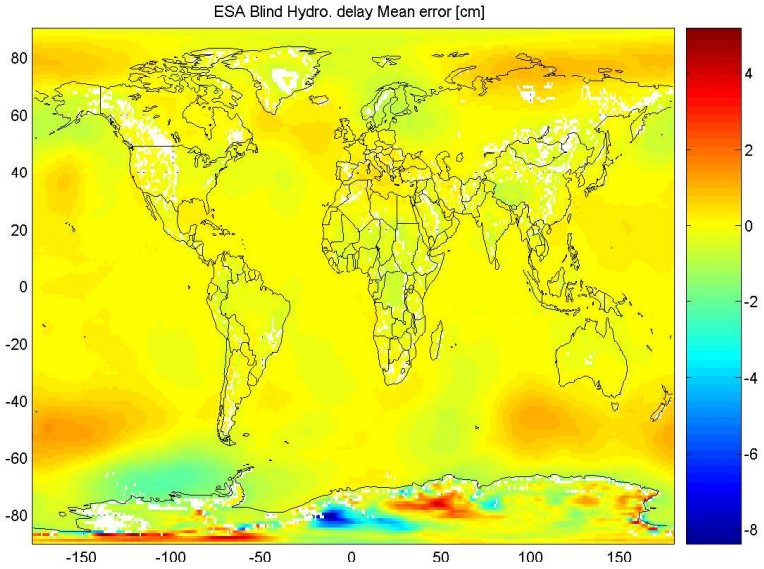

Figure 4.15: Map of the mean deviation of the ESA Blind hydrostatic delay.

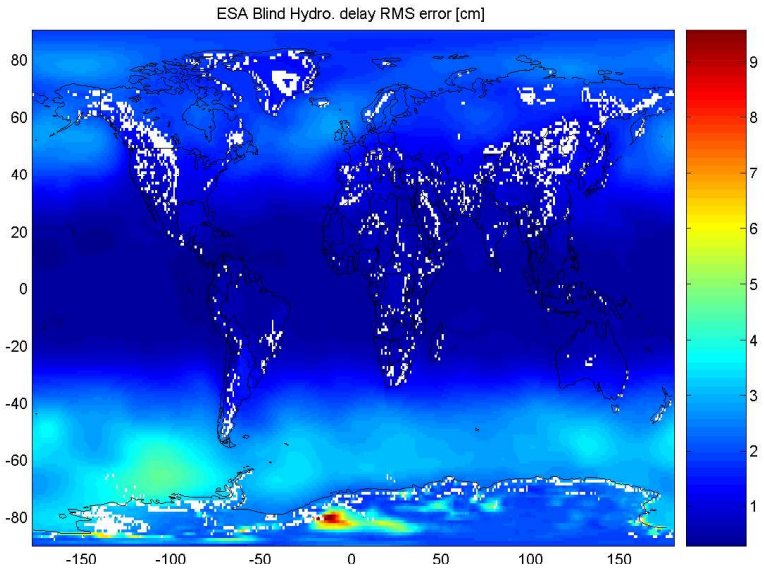

Figure 4.16: Map of the rms deviation of the ESA Blind hydrostatic delay.

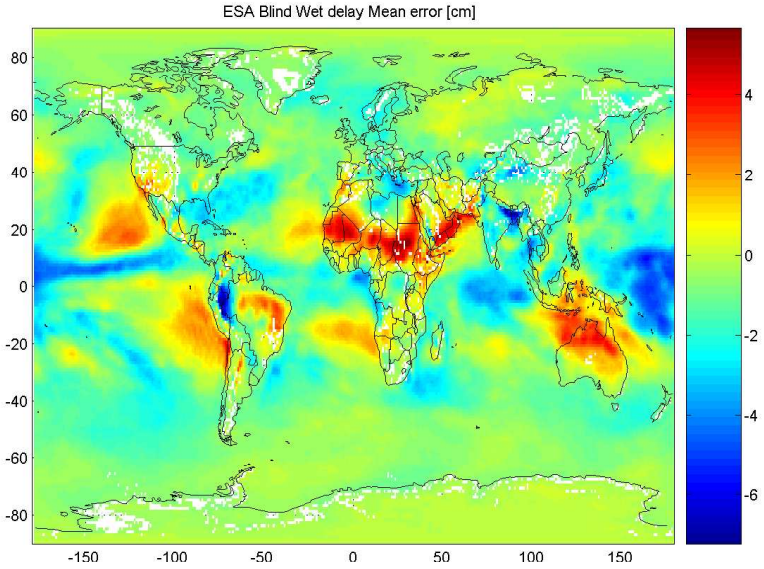

Figure 4.17: Map of the mean deviation of the ESA Blind wet delay. If we compare this map to the figure 4.18 , the correlation between the wet delay deviation over the Pacific Ocean and the temperature anomaly is striking.

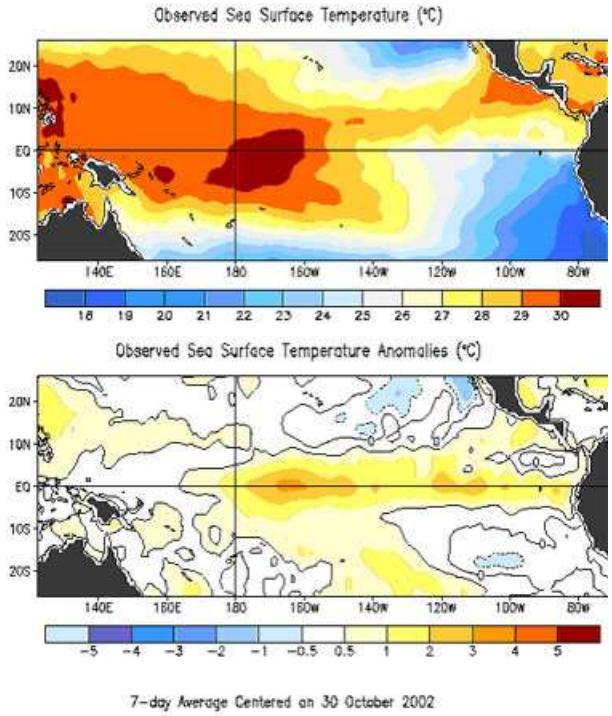

Figure 4.18: Maps of the Sea Surface Temperature and of the Sea Surface Anomaly above the Pacific Ocean in October 2002. Image from www.intellicast.com/DrDewpoint/Library/1357/

[cm]	Total delay	Hydrostatic delay	Wet delay
Mean	-8.7369113e-001	-5.8349008e-002	-8.1534212e-001
Rms	4.5446085e+000	1.6125861e+000	4.4368735e+000
Min	-2.0587233e+001	-1.1299080e+001	-2.1601681e+001
Max	1.6157922e+001	1.0088440e+001	1.6124336e+001

Table 4.5: Table of the ESA Blind model statistics.

	Total pressure	Water vapor pressure	Temperature	α	λ
ESA Blind	No	No	No	No	No
ESA Blind with λ	No	No	No	No	Yes
ESA Met without T	Yes	Yes	No	No	No
ESA Met	Yes	Yes	Yes	No	No
ESA Met with α	Yes	Yes	Yes	Yes	No
ESA Met with λ	Yes	Yes	Yes	No	Yes
ESA Met with λwithout T	Yes	Yes	No	No	Yes
ESA Ground	Yes	Yes	Yes	Yes	Yes

Table 4.6: Summary of the models derived from the ESA Blind model

4.6.1.3 Models derived from the ESA Blind model

In order to study the performances of the ESA Blind model, we have to know what are the parts of the model to be improved. Are the physical equations, the harmonic fitting or the values of the parameter to be blamed for the loss of precision?

If we want to test the equations without any additional information, we have to use what we called the ESA Ground model in chapter 3.

It is noticeable that the high error values in Antarctica have disappeared. Some point characterised with a particularly high error appear on the map. These points should be considered as outliers, as they are due to some errors in the calculation of the λ coefficient. The maximum values of the error are now around 6 cm and are essentially localised in Himalaya. This is not worrying, because we know that the orography stored in the PDS data encounters difficulties to describe mountainous areas.

We can see in table 4.7 that with the measured or calculated values as input of the equations, the overall bias is nearly null and the overall rms is approximately equal to 7,3 mm. We can conclude that the equations as such provide totally satisfying results on a global basis. This means that the ESA Blind model error comes essentially from the tabulated parameters.

We have seen that introducing measured surface total pressure, temperature and water vapor pressure totally removes the hydrostatic delay error, but the rms overall error for the total delay has only reduced of approximately 1.1 cm. This means either α or λ or both play a important role in the accuracy of the wet delay.

The "ESA Met with alpha" model is precisely the ESA Met model where the local α calculated from the real profile has been provided as an input. Looking at the figures and at the tables, we can remark that there are nearly no differences with the ESA Met model. Similarly, the "ESA Met with lambda" model

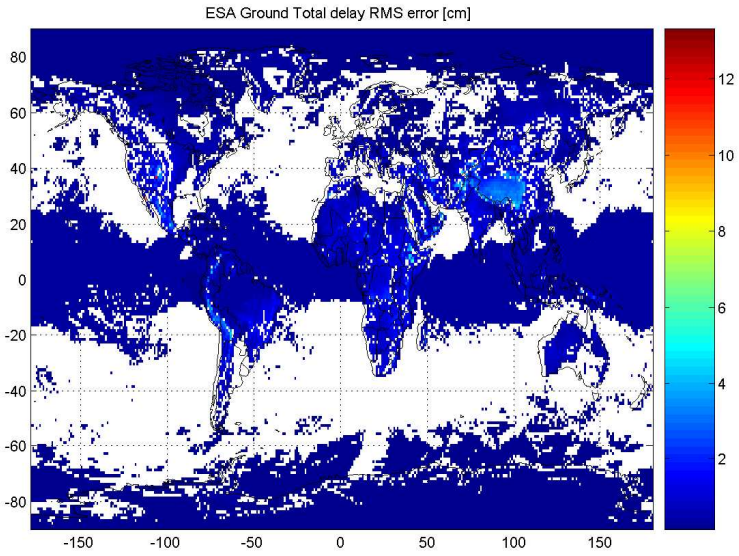

Figure 4.19: Map of the rms deviation of the ESA Ground total delay. The color bar is not well centered because of an outlier point in the Middle-East. More investigations have to be performed in order the understand the origin of this anomaly.

	Total delay	Hydrostatic delay	Wet delay
Mean	-7.8795080e-002	1.3277340e-002	-9.1897275e-002
Rms	7.3223696e-001	1.5594122e-002	7.3561478e-001
Min	-5.7311300e+000	-4.9580440e-003	-5.7470475e+000
Max	5.8662211e+001	2.2904294e-002	5.8647488e+001

Table 4.7: Table of the ESA Ground model statistics.

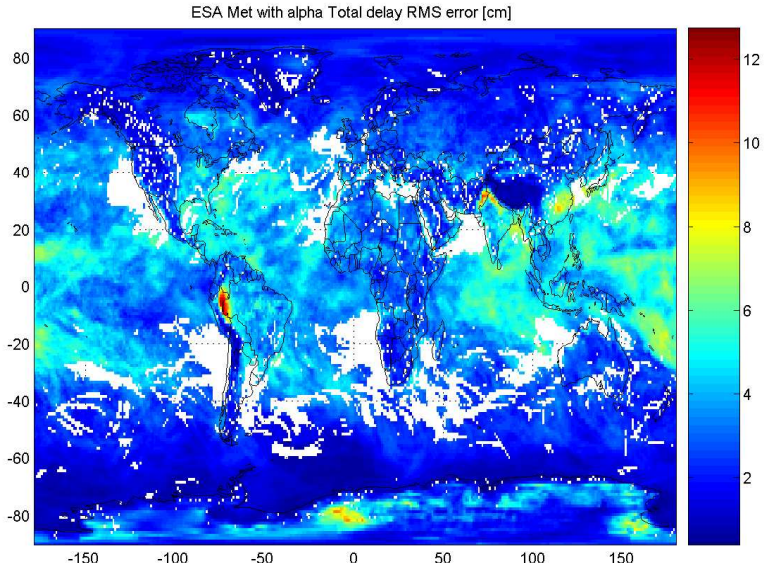

Figure 4.20: Map of the rms deviation of the ESA Met with alpha total delay.

is identical to the ESA Met model, but this time, λ is additionally provided as an input. This model provides excellent results, nearly equivalent to the ESA Ground model. We can see that the South-American and the Antarctic anomalies have now disappeared.

In order to check if the λ parameter was the only one that should be given with a higher precision to increase the accuracy, we imagined a Blind model where only the λ parameter was provided as an input. The results are equivalent to those of the ESA Met model, with an overall rms value around 3,6 cm. It is obvious that neither the surface parameters alone nor λ alone can reduce the blind model error of more then 1 cm. Please note the very high values of the extreme errors of the wet delay. The reason is that sometimes the values of the calculated λ can be quite high in some points and this leads to huge inaccuracies if the surface water vapor pressure is over-estimated.

In order to test the relative influence of the various parameters, we tried the "ESA Met with lambda" without providing the surface temperature as an input. Strangely, the results are even better then with the ESA Ground model. In fact, this can be easily explained: the temperatures in the atmosphere are not as variable as the ground temperature. That is the reason why tabulated temperatures, which are kinds of mean temperatures, provide better results.

In order to understand the origin of the big hydrostatic error of the ESA Blind model over Antarctica, we tried a last model: the ESA Met model without temperature. Or if you prefer, the ESA Blind model where the real pressure and

[cm]	Total delay	Hydrostatic delay	Wet delay
Mean	-2.5437962e-001	1.3276368e-002	-2.6747262e-001
Rms	3.6030496e+000	1.5593134e-002	3.6045472e+000
Min	-1.7342755e+001	-4.9707719e-003	-1.7325844e+001
Max	2.0756130e+001	2.2914273e-002	2.0743813e+001

Table 4.8: Table of the ESA Met with alpha model statistics.

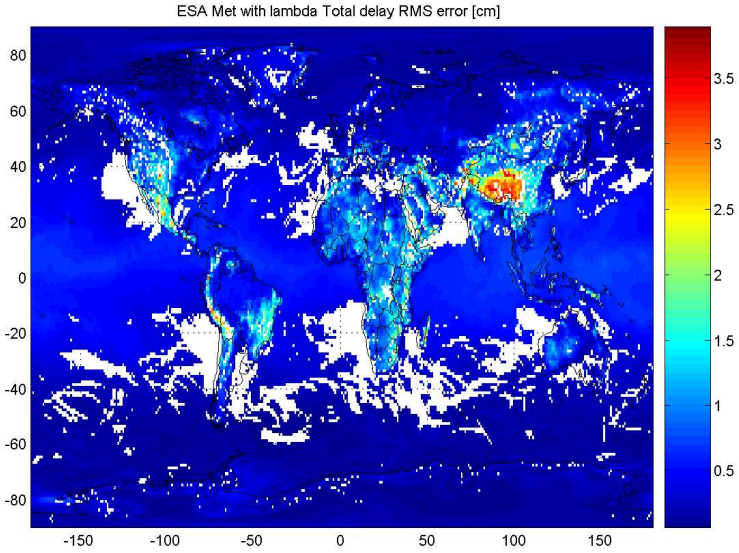

Figure 4.21: Map of the rms deviation of the ESA Met with lambda total delay.

[cm]	Total delay	Hydrostatic delay	Wet delay
Mean	-1.9438533e-001	1.3276368e-002	-2.0747833e-001
Rms	7.7931086e-001	1.5593134e-002	7.8524895e-001
Min	-5.6564560e+000	-4.9707719e-003	-5.6709818e+000
Max	6.4379479e+001	2.2914273e-002	6.4364206e+001

Table 4.9: Table of the ESA Met with lambda model statistics.

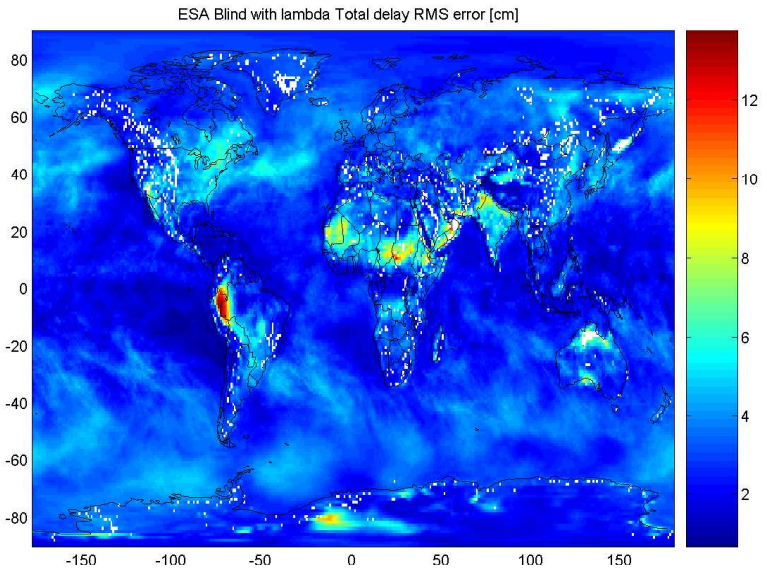

Figure 4.22: Map of the rms deviation of the ESA Blind with lambda total delay.

[cm]	Total delay	Hydrostatic delay	Wet delay
Mean	-6.4796647e-001	-6.0958638e-002	-5.8700782e-001
Rms	3.6409970e+000	1.6398751e+000	3.3850317e+000
Min	-1.6436166e+001	-1.0598319e+001	-1.6313624e+001
Max	1.9106434e+002	1.0198992e+001	1.9101049e+002

Table 4.10: Table of the ESA Blind with lambda model statistics.

[cm]	Total delay	Hydrostatic delay	Wet delay
Mean	-1.9518643e-001	1.3234946e-002	-2.0823875e-001
Rms	6.4772491e-001	1.5520370e-002	6.5382866e-001
Min	-5.5090276e+000	-4.9360522e-003	-5.5232585e+000
Max	2.6350593e+001	2.2907087e-002	2.6335765e+001

Table 4.11: Table of the ESA Met with lambda but without temperature model statistics.

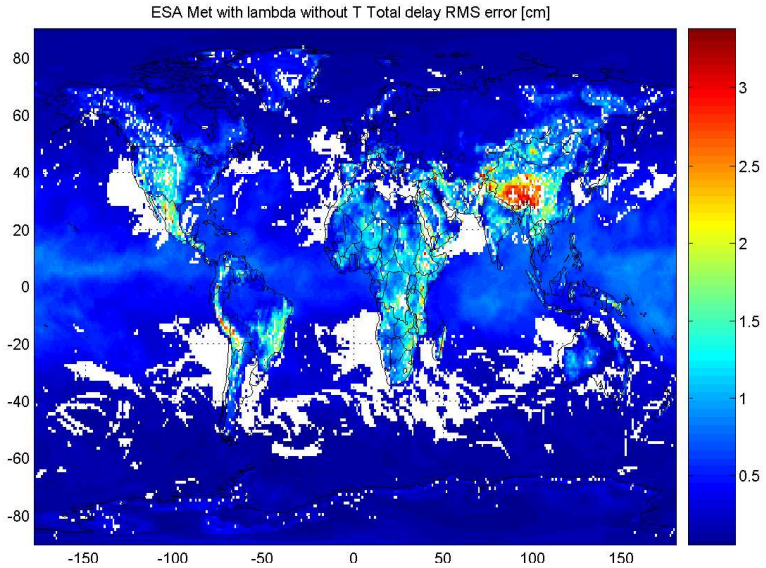

Figure 4.23: Map of the rms deviation of the ESA Met with lambda but without temperature model total delay.

[cm]	Total delay	Hydrostatic delay	Wet delay
Mean	-3.3980838e-001	1.3234946e-002	-3.5286068e-001
Rms	3.5922996e+000	1.5520370e-002	3.5941167e+000
Min	-1.7372928e+001	-4.9360522e-003	-1.7390212e+001
Max	1.9256973e+001	2.2907087e-002	1.9240487e+001

Table 4.12: Table of the ESA Met without temperature model statistics.

water vapor pressure are provided as input. The hydrostatic error for this model is quasi equal to zero, which means that the error came from a mis-modeling of the pressure over Antarctica. We could already deduce it from the map of the pressure error in the Annex B, but this test shows that the related error is really huge. Nevertheless, we still can see an significant error over Antarctica on the total delay rms error map. Comparing this one with map 4.23, we can deduce that this error is due to the λ parameter.

4.6.1.4 Latitude dependence of the delay

In the previous assessments of the ESA Blind model, during the Galileo test bed, a figure of the latitude dependence of the rms error for the total delay was provided. The figure shown below comes from an assessment of the version 2.3 of the Blind

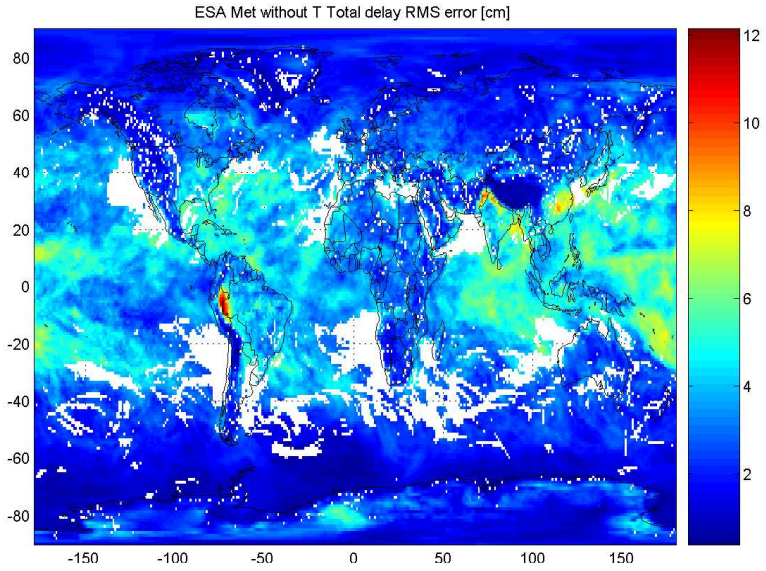

Figure 4.24: Map of the rms deviation of the ESA Met without temperature model total delay.

model that has been made during GSTB-V1.

If we plot the same curve for the version 2.4, considering our ECMWF data set, we obtain the figure 4.26. Comparing with the previous one, the peak seems higher (5.7 instead of 4,8 cm). This does not mean that the version 2.4 of the model is worse than version 2.3. This is simply due to the fact that our data set does not contain data over a whole year but only summer months. This period corresponds to winter in the southern hemisphere, which mean more precipitations and consequently a biggest wet delay. As the wet delay is more important, the error on the wet delay increases in the same way. We tried to simulate the other months of 2002 by adding to the curve its symmetric and then to perform the mean (see figure 4.27). The shape of the curve looks more like the previous one and the peak amplitude has decreased.

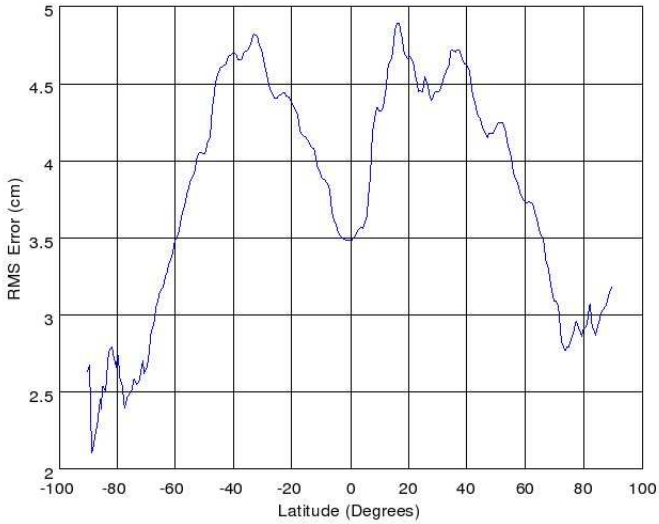

Figure 4.25: Graph of the latitude dependence of the rms error using NWP from 2003 and using the version 2.3 of the model.

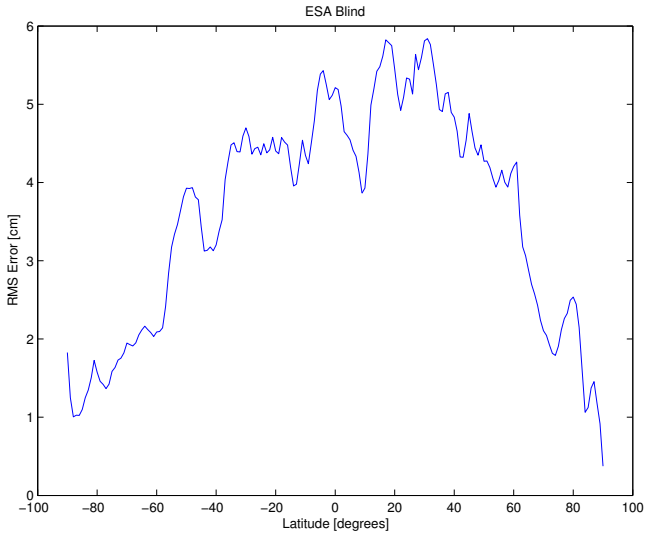

Figure 4.26: Graph of the latitude dependence of the RMS error.

[cm]	Total delay	Hydrostatic delay	Wet delay
Mean	-8.4119908e+000	-8.0216496e+000	-3.9034127e-001
Rms	8.9268328e+000	8.4896327e+000	7.0784939e-001
Min	-1.7215047e+001	-1.6282297e+001	-3.7338172e+000
Max	2.7366795e+000	2.7015742e+000	9.7531154e-001

Table 4.13: Table of the Hopfield's model statistics.

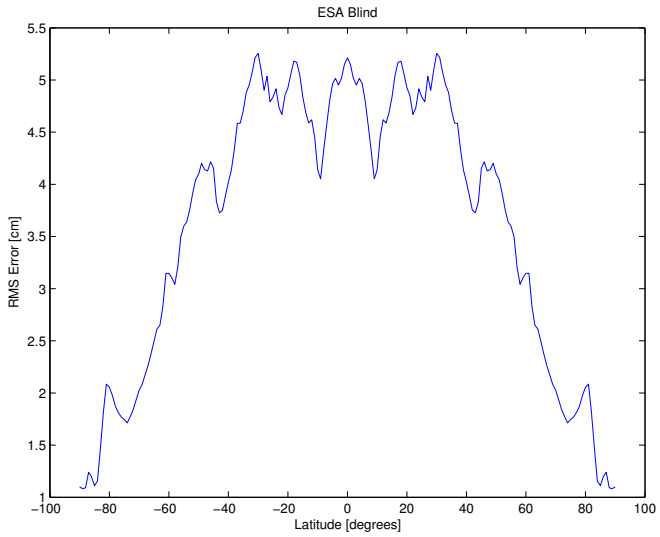

Figure 4.27: Graph of the simulated latitude dependence of the RMS error for a whole year.

4.6.2 Delay at 5000 meters high

The main observation that could be made out of these tests at high altitude is that the wet delay error has dramatically decreased for all the models. This is obviously due to the fact that the water vapor in mainly concentrated at low altitude.

The results of the Hopfield model at high altitude are not convincing either. The hydrostatic delay is particularly under-estimated over the northern hemisphere.

As far as the Saastamoinen model is concerned, the performances are very good: the overall rms error is below 5 mm.

Both hydrostatic and wet error are decreasing in the RTCA model. The main hydrostatic error is mainly concentrated on Antarctica while the wet error is located in South-East Asia.

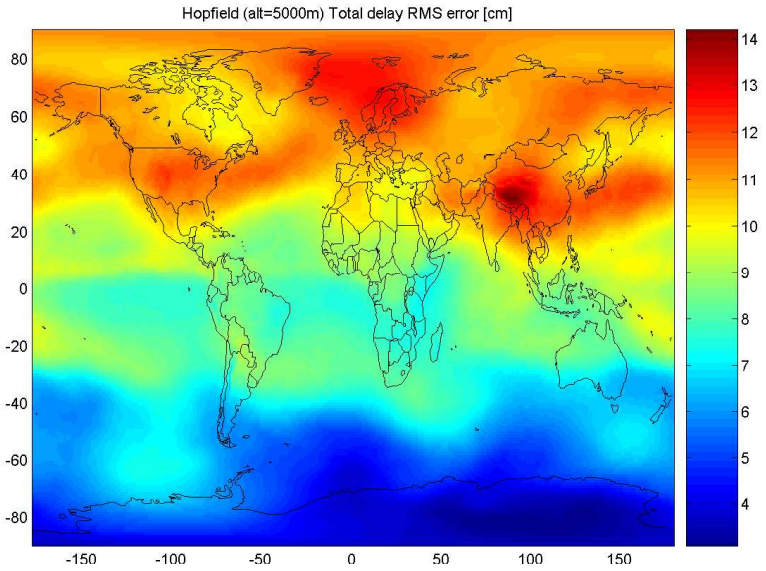

Figure 4.28: Map of the rms deviation of the Hopfield's model total delay at 5000 m.

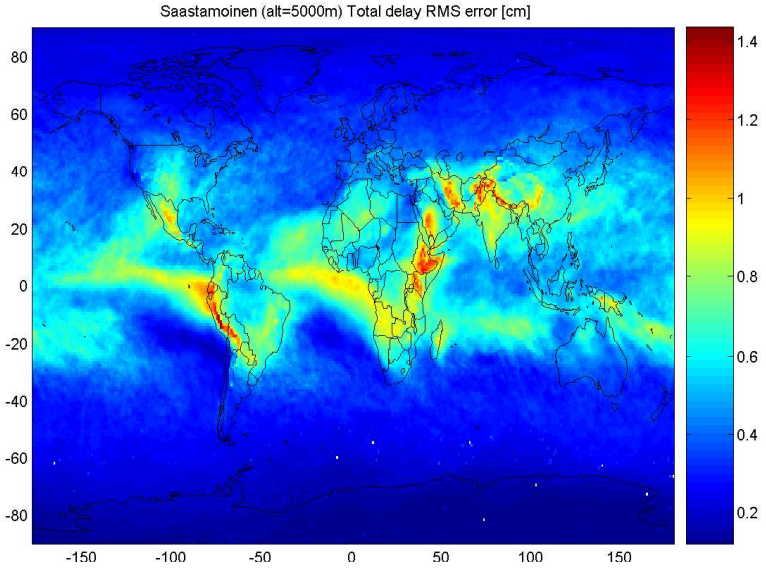

Figure 4.29: Map of the rms deviation of the Saastamoinen's model total delay at 5000 m.

[cm]	Total delay	Hydrostatic delay	Wet delay
Mean	2.7145450e-001	1.1676530e-001	1.5468922e-001
Rms	4.9519366e-001	1.1730297e-001	4.4150404e-001
Min	-1.9716906e+000	-8.6263464e-001	-1.9306363e+000
Max	2.8789095e+000	1.7695831e+000	2.6352280e+000

Table 4.14: Table of the Saastamoinen's model statistics.

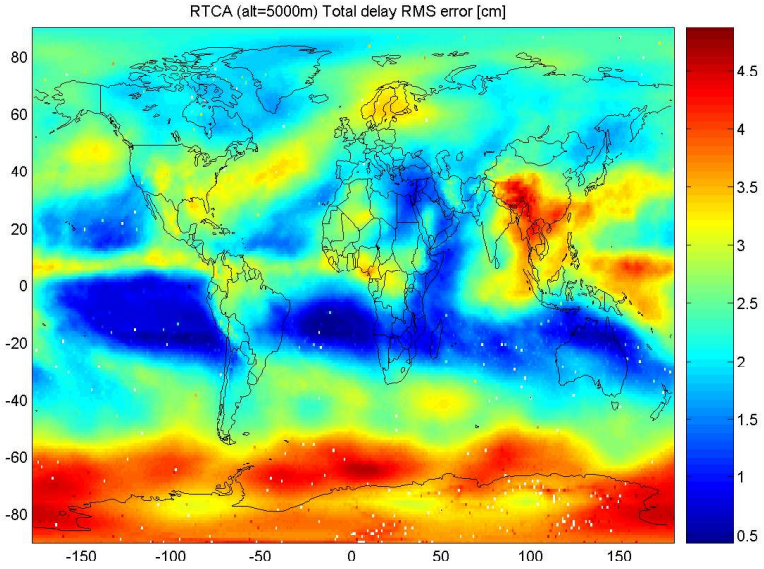

Figure 4.30: Map of the rms deviation of the RTCA model total delay at 5000 m.

The results found for the ESA Blind delay are quite surprising, the overestimation of the hydrostatic delay in Antarctica reaches 25 cm. On map 4.32, the color bar has been re-centered, so that we can see that the problem really come from the Antarctica. Anywhere else the results are quite good.

The error pattern of the ESA Ground model is very similar to the one at surface, but the outliers have disappeared. Note that this is the only model for which the overall rms error has slightly increased. We can see that at high altitude, the Saastamoinen model performs better. Nevertheless, the error is in the order of 1 cm, which remains very small.

[cm]	Total delay	Hydrostatic delay	Wet delay
Mean	-1.0827908e+000	-1.6779149e+000	5.9512348e-001
Rms	2.4938416e+000	2.4200184e+000	1.3846695e+000
Min	-2.2081065e+001	-2.2862322e+001	-6.0052821e+000
Max	1.8473125e+001	1.7547598e+001	2.8684048e+000

Table 4.15: Table of the RTCA model statistics.

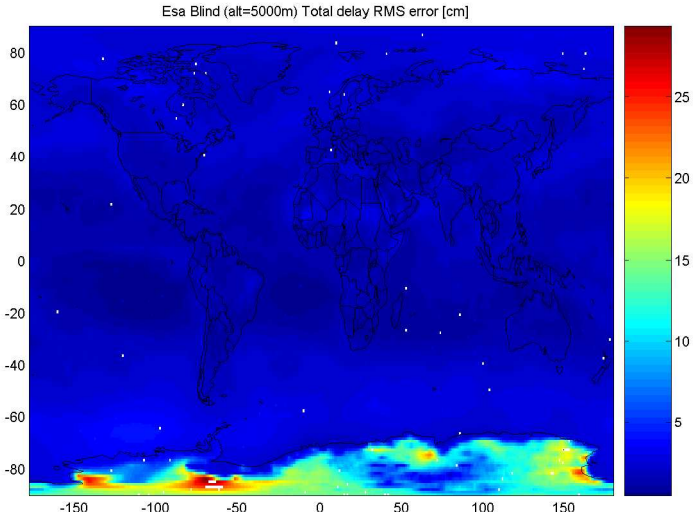

Figure 4.31: Map of the rms deviation of the ESA Blind model total delay at 5000 m.

[cm]	Total delay	Hydrostatic delay	Wet delay
Mean	-1.3745504e-001	-2.6606575e-001	1.2861071e-001
Rms	2.5386523e+000	2.1994713e+000	1.0623852e+000
Min	-2.0033689e+001	-2.0012680e+001	-5.5417618e+000
Max	3.5508147e+001	3.5154051e+001	4.4294307e+000

Table 4.16: Table of the ESA Blind model statistics.

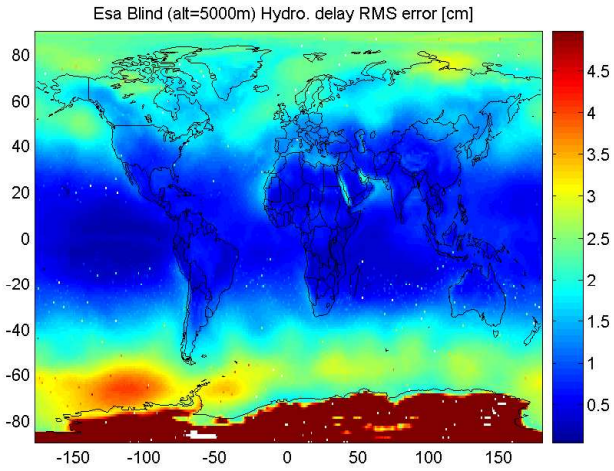

Figure 4.32: Map of the mean deviation of the ESA Blind model hydrostatic delay at 5000 m. The color bar has been re-centred.

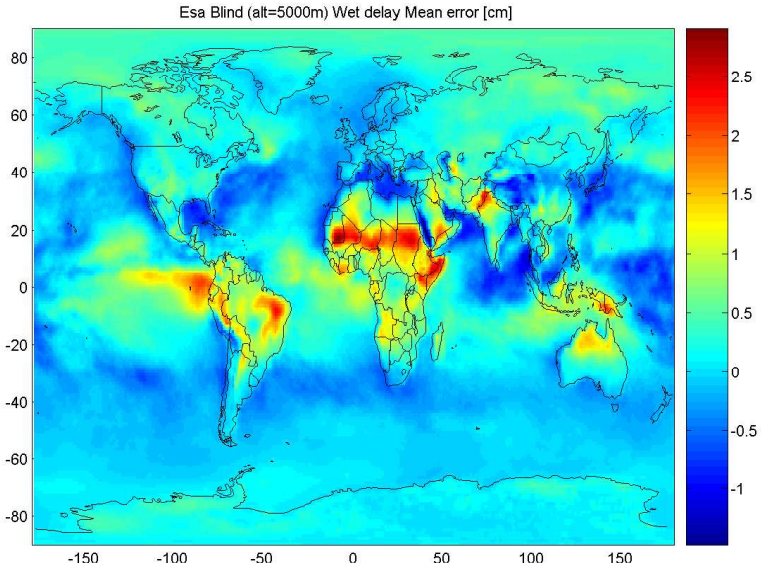

Figure 4.33: Map of the mean deviation of the ESA Blind model wet delay at 5000 m.

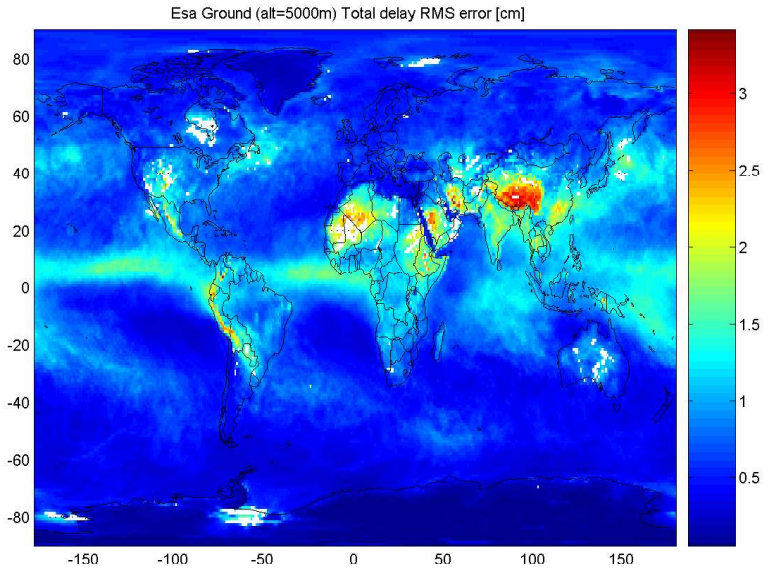

Figure 4.34: Map of the rms deviation of the ESA Ground model total delay at 5000 m.

[cm]	Total delay	Hydrostatic delay	Wet delay
Mean	3.7912786e-001	7.5042222e-003	3.7162362e-001
Rms	1.0024271e+000	1.2714513e-002	9.9876486e-001
Min	-2.4857919e+000	-9.6717141e-001	-2.3545035e+000
Max	5.9581246e+001	1.6610808e+000	5.9572535e+001

Table 4.17: Table of the ESA Ground model statistics.

Chapter 5

Conclusions

During this study, many assumptions and hypothesis used both for tropospheric delay models and for meteorological data processing have been analysed and criticised. The first interesting point of this work is the discussion on the refractivity coefficients. By analysing in detail the arguments in literature, we found out that the proposed coefficients in the previous Galileo tropospheric model were not the best available. Rüger's set of coefficients will probably be used in the next versions of the Galileo tropospheric model.

Concerning the validation exercise based on radiosondes, we managed to highly improve the processing of the profiles. A better accuracy of the integrated delay has been obtained thanks to the recovery of all the information contained in the BADC files.

We also got a first picture of the performances of the different models for several sites located all around the world. The results showed that the models developed for the Galileo project, the ESA Met and the ESA Blind models, were providing real improvements compared respectively to the other models based on surface measurements and to the RTCA model. We also noticed that the performances of the different models can vary from a place to another.

Assessments performed at global scale are more relevant to localise the problematic regions. Nevertheless, for the next steps in the fine-tuning of the blind delay, it could be very useful to go back to the radiosonde data in order to understand more precisely the reasons of the poor accuracy encountered in those areas. It is also very important to compare global estimations to local measurements.

Another interesting point is the fact that we also corrected the wrong implementation of the saturation pressure equation. When the coefficients of the future versions of ESA Blind model are re-computed, the new formula will be used. Finally the know-how derived from this analysis has been very useful during the tests of the NWP data processing algorithms.

The second part of this study concerned NWP data gathered during seven month in 2002. The detailed analysis of the processing procedures lead to several

improvements as well. Some of these modified routines will also be used in the re-computation of the parameters in the next versions of the ESA Blind model.

If we consider the results, the first observation is that seven months of data are not enough to assess the general behaviour of the models. Our data set was centered on the summer months and the biggest errors were observed in the southern hemisphere. It is very probable that we miss other problematic areas on the northern part of the world which would appear during winter. Now that the procedures have been updated, it would be easy to repeat this validation exercise on an extended set of data. Two or three years would be more appropriate for these tests.

We also have to notice that the year 2002 was not a "standard" year, because an El-Niño event occurred on the Pacific Ocean. The positive side of this particularity is that we henceforth know that during an El-Niño event, the mean delay over the Pacific Ocean can increase by more or less 7 cm. The ESA Blind model only models daily and yearly fluctuations, so that cycles lasting more than one year, like the El-Niño Southern Oscillations, are neglected. That is the reason why it was interesting to measure the effects of this kind of events.

Focusing on the ESA Blind model, we noticed that this model represented a real improvement considering the RTCA model. The introduction of the longitude dependence of the parameters and of diurnal cycles, as well as the increase of the resolution in latitude, lead to a diminution of the overall rms error in the order of 30%. The gain of accuracy is even more important if we do not take the Antarctica into account. The analysis of different models derived from the ESA Blind model allowed us to understand better the behaviour of the different parts of the model. This will be useful for future improvements of the model because this test not only pointed out the problematic areas, but also underlined the problematic parameters.

To conclude, the results of this work are triple. First of all, we performed a validation of the latest ESA Blind model with radiosonde data and NWP data that have never been used before for this application. Then we improved some procedures in the data processing and these new procedures will be used to generate future versions of the model. Finally, we started to build a validation tool[1] for the fine-tuning and the optimization of the model.

[1]In order to complete the validation tool, additionally to the extension of the NWP data set, some microwave radiometer measurements and GPS delay measurements should also be considered.

Annex A: Tables of errors for radiosonde profiles

Adelaide (Aus)	61 profiles								
Mean error [cm]	Saastamoinen	Hopfield	Black	Askne-Nordius	RTCA	ESA Blind	ESA Ground	ESA Met	Integration
Total delay	-1.8800	0.8426	-0.7070	-0.0698	-11.2793	-1.0664	0.0636	-0.4195	0.7060
Hydrostatic delay	-0.4862	2.5101	-0.1101	0.0546	0.2826	-0.0134	0	0	0.7060
Wet delay	-1.3938	-1.6675	-0.5969	-0.1244	-11.5619	-1.0530	0.0636	-0.4195	0
RMS error [cm]									
Total delay	4.0491	3.4078	3.4503	0.2319	11.6092	2.9578	0.2027	3.5186	0.7105
Hydrostatic delay	0.4862	2.6292	0.1186	0.0546	1.5044	1.4827	0	0	0.7105
Wet delay	3.8469	4.0111	3.4398	0.2536	12.0468	3.5592	0.2027	3.5186	0
Brasilia (Bra)	31 profiles								
Mean error [cm]	Saastamoinen	Hopfield	Black	Askne-Nordius	RTCA	ESA Blind	ESA Ground	ESA Met	Integration
Total delay	-8.3814	4.0238	8.8563	-0.1175	4.1730	0.8083	0.1733	-3.2862	0.6192
Hydrostatic delay	-0.4188	4.7835	0.2404	0.0483	0.2778	0.7673	0	0	0.6192
Wet delay	-7.9626	-0.7597	8.6159	-0.1659	3.8952	0.0411	0.1733	-3.2862	0
RMS error [cm]									
Total delay	8.6094	4.3895	9.0650	0.1661	4.5815	2.0111	0.2037	3.9335	0.6248
Hydrostatic delay	0.4188	4.7901	0.2407	0.0483	0.4878	0.8527	0	0	0.6248
Wet delay	8.2022	1.9521	8.8292	0.2032	4.3470	1.9070	0.2037	3.9335	0
Jeddah King Abdul Aziz int (Sau.Ar.)	43 profiles								
Mean error [cm]	Saastamoinen	Hopfield	Black	Askne-Nordius	RTCA	ESA Blind	ESA Ground	ESA Met	Integration
Total delay	-4.5374	-0.3382	1.5261	-0.0657	-7.1165	-0.5620	0.1040	0.4403	0.8629
Hydrostatic delay	-0.4813	3.8452	0.0909	0.0546	-0.1481	-0.0692	0	0	0.8629
Wet delay	-4.0561	-4.1833	1.4352	-0.1203	-6.9684	-0.4929	0.1040	0.4403	0
RMS error [cm]									
Total delay	6.9045	4.5035	4.8758	0.3071	8.4119	4.4594	0.2845	4.5994	0.8673
Hydrostatic delay	0.4813	4.0381	0.1006	0.0546	0.4460	0.4136	0	0	0.8673
Wet delay	6.5982	6.6357	4.8394	0.3232	8.3705	4.6202	0.2845	4.5994	0

Dakar (Sen)	28 profiles								
Mean error [cm]	Saastamoinen	Hopfield	Black	Askne-Nordius	RTCA	ESA Blind	ESA Ground	ESA Met	Integration
Total delay	-5.5433	-1.9612	-1.9669	0.0594	-15.2382	-8.5836	0.1669	-1.9140	0.8590
Hydrostatic delay	-0.4791	3.2985	0.2083	0.0546	0.7568	0.4250	0	0	0.8590
Wet delay	-5.0642	-5.2598	-2.1753	0.0049	-15.9950	-9.0085	0.1669	-1.9140	0
RMS error [cm]									
Total delay	7.1087	4.2618	3.0541	0.1441	15.4169	8.8941	0.2151	4.2235	0.8792
Hydrostatic delay	0.4791	3.4168	0.2087	0.0546	0.8824	0.6346	0	0	0.8792
Wet delay	6.7420	6.9326	3.1932	0.1314	16.1649	9.3052	0.2151	4.2235	0
Fairbanks (USA)	52 profiles								
Mean error [cm]	Saastamoinen	Hopfield	Black	Askne-Nordius	RTCA	ESA Blind	ESA Ground	ESA Met	Integration
Total delay	1.2117	1.1237	-8.6996	-0.3788	1.6116	4.0730	-0.3796	0.9323	0.0105
Hydrostatic delay	-0.4905	-0.3838	-0.1679	0.0538	0.8165	1.8122	0	0	0.0105
Wet delay	1.7022	1.5075	-8.5317	-0.4326	0.7951	2.2609	-0.3796	0.9323	0
RMS error [cm]									
Total delay	2.1972	2.1317	8.9975	0.5962	3.3996	5.1683	0.5799	2.1284	0.0832
Hydrostatic delay	0.4906	0.4512	0.2303	0.0538	2.8528	3.3156	0	0	0.0832
Wet delay	2.4992	2.3586	8.8653	0.6315	2.4198	3.2564	0.5799	2.1284	0
Gibraltar (U.K.)	61 profiles								
Mean error [cm]	Saastamoinen	Hopfield	Black	Askne-Nordius	RTCA	ESA Blind	ESA Ground	ESA Met	Integration
Total delay	-4.2723	-2.3711	-5.4403	0.0275	-2.4935	0.5143	0.0787	-2.6451	0.5288
Hydrostatic delay	-0.4931	1.9138	-0.0406	0.0553	1.8274	3.0382	0	0	0.5288
Wet delay	-3.7792	-4.2849	-5.3997	-0.0278	-4.3209	-2.5239	0.0787	-2.6451	0
RMS error [cm]									
Total delay	4.6747	2.7829	5.7180	0.0541	3.6662	2.6873	0.0921	3.0979	0.5333
Hydrostatic delay	0.4931	2.0277	0.0524	0.0553	2.3267	3.3541	0	0	0.5333
Wet delay	4.2281	4.7230	5.6845	0.0543	4.6355	3.0180	0.0921	3.0979	0

Sapporo (Jap)	61 profiles								
Mean error [cm]	Saastamoinen	Hopfield	Black	Askne-Nordius	RTCA	ESA Blind	ESA Ground	ESA Met	Integration
Total delay	-0.5425	-0.1205	-8.4080	0.0487	-5.7884	-0.2006	0.0483	0.8749	0.9591
Hydrostatic delay	-0.4862	0.3259	0.0282	0.0542	-2.0915	-1.5346	0	0	0.9591
Wet delay	-0.0563	-0.4464	-8.4362	-0.0055	-3.6969	1.3340	0.0483	0.8749	0
RMS error [cm]									
Total delay	0.8891	0.7674	8.5270	0.0646	6.2417	2.2998	0.0587	1.1965	1.0075
Hydrostatic delay	0.4862	0.3990	0.0499	0.0542	2.8586	2.4706	0	0	1.0075
Wet delay	0.7063	0.8321	8.5606	0.0429	3.9649	1.9554	0.0587	1.1965	0
St-Hubert (Bel)	24 profiles								
Mean error [cm]	Saastamoinen	Hopfield	Black	Askne-Nordius	RTCA	ESA Blind	ESA Ground	ESA Met	Integration
Total delay	-3.6286	-1.9748	-8.1526	0.0345	1.6962	0.8900	0.0445	-2.1866	0.9066
Hydrostatic delay	-0.4609	0.7791	-0.1252	0.0514	2.2459	1.5597	0	0	0.9066
Wet delay	-3.1677	-2.7539	-8.0274	-0.0169	-0.5497	-0.6696	0.0445	-2.1866	0
RMS error [cm]									
Total delay	3.8941	2.2547	8.2858	0.0606	2.7026	2.2818	0.0624	2.4925	0.9881
Hydrostatic delay	0.4609	0.8678	0.1337	0.0514	2.7122	2.1651	0	0	0.9881
Wet delay	3.4684	3.0361	8.1684	0.0527	1.5373	1.5904	0.0624	2.4925	0
Vandenberg (USA)	33 profiles								
Mean error [cm]	Saastamoinen	Hopfield	Black	Askne-Nordius	RTCA	ESA Blind	ESA Ground	ESA Met	Integration
Total delay	-2.2975	-0.2241	-3.7470	-0.0445	-2.0949	0.3541	0.0336	-1.2112	1.2716
Hydrostatic delay	-0.4824	1.8142	0.0038	0.0542	0.6118	-0.2946	0	0	1.2716
Wet delay	-1.8151	-2.0383	-3.7508	-0.0988	-2.7067	0.6487	0.0336	-1.2112	0
RMS error [cm]									
Total delay	2.8205	1.6710	4.7689	0.1464	3.3508	2.5470	0.1212	2.0972	1.2750
Hydrostatic delay	0.4824	1.9086	0.0494	0.0543	1.0293	0.8925	0	0	1.2750
Wet delay	2.4433	2.6250	4.7690	0.1708	4.0060	2.9670	0.1212	2.0972	0

Annex B: Maps of the rms deviation of the harmonic model (ESA Blind 2.4)

The ESA Blind Model tables were calculated assuming a seasonal (and daily) harmonic model for each physical quantity. The mean values of the parameters, the amplitudes of the cosine functions and the positions of the maxima were derived in order to achieve the best fitting to the real meteorological situation over the 15 years studied in the ERA 15 re-analysis. As the parameters do not exactly obey to a cosine function, we can compute the rms error of the harmonic assumption for each of them.

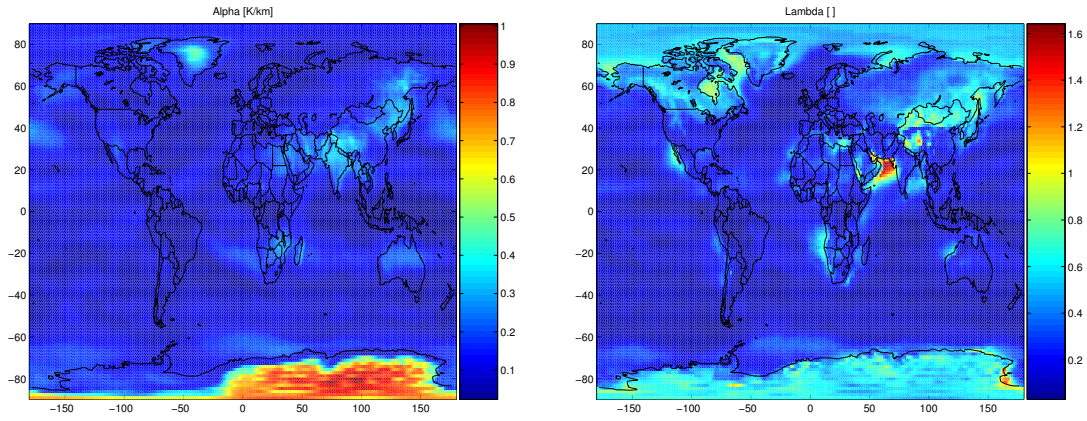

Figure 5.1: *(Left)* Map of the error of the harmonic model for α. *(Right)* Map of the error of the harmonic model for λ.

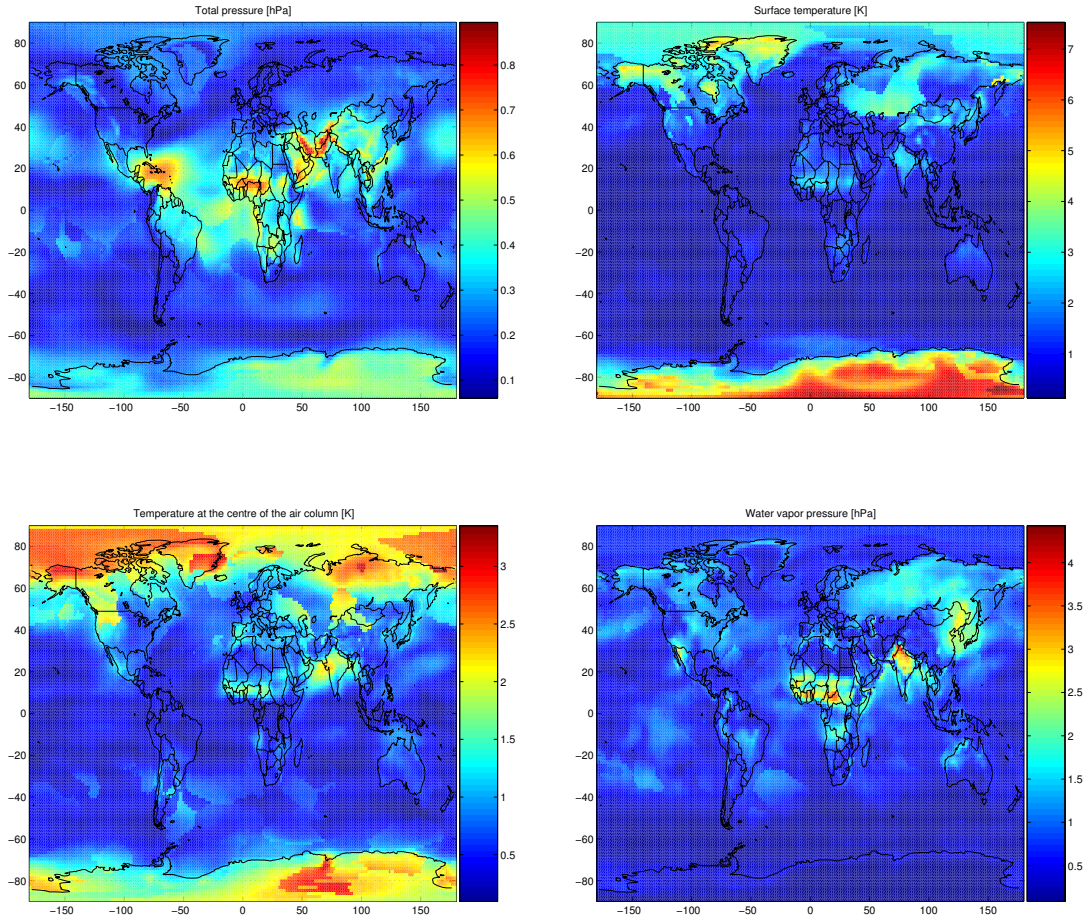

Figure 5.2: *(Top left)* Map of the error of the harmonic model for the total pressure. *(Top right)* Map of the error of the harmonic model for the surface temperature.*(Bottom left)* Map of the error of the harmonic model for the temperature at the center of the air column. *(Bottom right)* Map of the error of the harmonic model for the water vapor pressure.

Bibliography

[1] J. Allnutt, *Satellite-to-ground radiowave propagation*, IEE Electromagnetic Waves Series 29, Peter Peregrinus Ltd, 1989.

[2] G. P. Anderson & al., *AFGL Atmospheric Constituent Profiles (0-120km),* Air Force Geophysics Laboratory, Environmental Research Papers, n° 954, 15 May 1986.

[3] J. Askne and H. Nordius, Estimation of tropospheric delay for microwaves from surface weather data, in *Radio Science,* vol. 22, pp. 379-386, 1986.

[4] Y. E. Bar-Sever & al., Estimating horizontal gradients of tropospheric path delay with a single GPS receiver, in *Journal of Geophysical Research,* vol. 103, n° B3, pp. 5019-5035, 1998.

[5] J. Benedicto & al., Galileo: Satellite System Design and Technology Developments, http://esamultimedia.esa.int/docs/galileo_world_paper_Dec_2000.pdf, November 2000.

[6] M. Bevis and al., GPS Meteorology: Remote Sensing of Atmospheric Water Vapor Using the Global Positioning System, in *Journal of Geophysical Research,* vol. 97, n° D14, pp. 15,787-15,801, 1992.

[7] M. Bevis and al., GPS Meteorology: Mapping Zenith Delay onto Precipitable Water, in *American Meteorological Society,* vol. 33, pp 379-386, 1994.

[8] H. D. Black, An Easily Implemented Algorithm for Tropospheric Range Correction, in *Journal of Geophysical Research,* vol. 83, pp. 1825-1828, 1978.

[9] J. L. Davis and al., Geodesy by interferometry: Effects of atmospheric modeling errors on estimates of baseline length, in *Radio Sciences*, vol. 20, n° 6, pp. 1593-1607, 1985.

[10] ECMWF ERA 15 website, www.ecmwf.int/research/era/ERA15.

[11] ECMWF Research Department, *IFS Documentation, Part III: Dynamics and numerical procedures,* CY23R4, edited by P. W. White.

[12] G. Elgered, Tropospheric radiopath delay from ground-based microwave radiometry, in *Atmospheric Sensing by Microwave Radiometry,* edited by Michael A. Janssen, pp. 215-257, 1993.

[13] T. R. Emardson, G. Elgered and J. M. Johansson, Three months of continuous monitoring of atmospheric water vapor with a network of Global Positioning System receivers, in *Journal of Geophysical Research,* vol. 103, n° D2, pp. 1807-1820, 1998.

[14] R.G. Fleagle & J. A. Businger, *An Introduction to Atmospheric Physics,* pp. 15-16 & pp. 345-349, Academic, Orlando, Fla., 1980.

[15] G. K. Hartmann, The Determination of Tropospheric Conditions (especially H_2O) Affecting the Accuracy of Position Measurements, in *Geophysical Monograph 73,* IUGG vol. 13 (*Environmental Effects on Spacecraft Trajectories and Positioning*), Am. Geophys. Union, pp. 73-82, 1993.

[16] S. Hasegawa & D. P. Strokesburry, Automatic digital microwave hygrometer, in *Review of Science Instruments,* vol. 46, n° 7, July 1975.

[17] J. P. Hauser, Effects of Deviation From Hydrostatic equilibrium on Atmospheric Corrections to Satellite and Lunar Laser Range Measurements, in *Journal of Geophysical Research,* vol. 94, n° B8, pp. 10182-10186, August 1989.

[18] G. W. Hein & al., Status of Galileo Frequency and Signal Design, http://europa.eu.int/comm/dgs/energy_transport/galileo/doc/galileo_stf_ion2002.pdf, 2002.

[19] T. A. Herring and K. Quinn, Atmospheric Delay Correction to GLAS Laser Altimeter Ranges, 1999.

[20] R. J. Hill & al., Theoretical and calcalutionnal aspects of radio refractive index of water vapor, in *Radio Science,* vol. 17, n° 5, pp 1251-1257, September-October 1982.

[21] H. S. Hopfield, Two-Quartic Tropospheric Refractivity Profile for Correcting Satellite Data, in *Journal of Geophysical Research,* vol. 74, pp. 4487-4499, 1969.

[22] H. S. Hopfield, Tropospheric effect on electromagnetically measured range: Prediction from surface weather data, in *Radio Sciences,* vol. 6, n°3, pp. 357-367, March 1971.

[23] HyperPhysics, http://hyperphysics.phys-astr.gsu.edu/hbase/hph.html, Georgia State University, 2005.

[24] IERS Convention (2003), D. D. McCarthy and G. Petit, *IERS Technical Note n°32,* Frankfurt am Main, Verlag des Bundesamts fur Kartographies und Geodäsie, pp. 99-103, 2004. (www.iers.org/iers/publications/tn/tn32/)

[25] Recommendation ITU-R P.835-3, *Reference Standard Atmosphere*, Question ITU-R 201/3,1999.

[26] H. J. Liebe, Models of the Refractive Index of the Neutral Atmosphere at Frequencies Below 1000GHz, Chapter II.3.1.2, in *The Upper Atmosphere-Data Analysis and Interpretation,* edited by Dieminger-Hartmann-Leitinger, pp. 270-287, 1996.

[27] D.S. MacMillan, Atmospheric gradient from very long baseline interferometry observations, in *Geophysical Research Letters,* vol 22, n°9, pp. 1041-1044, 1995.

[28] A. Martellucci, Galileo Reference Troposphere Model for the User Receiver, ESA-APPNG-REF/00621-AM, Iss. 2 Rev. 3, 21/01/2004.

[29] A. Martellucci, Galileo Reference Troposphere Description of models, ESA-APPNG-SPEC/00165-AM, Iss. 2 Rev. 2, 31/08/2004.

[30] A. Martellucci & T. Schüler, Comparison of radiometric and GPS measurements in Balearic islands with numerical weather prediction data, 8th Specialist Meeting on Microwave Radiometry and Remote Sensing Applications, Faculty of Engineering, University "Le Sapienza", Rome, February 2004.

[31] Mendes and al., Improved mapping functions for atmospheric refraction correction in SLR, in *Geophysical Research Letters,* vol. 29, n°10,pp. 53-1 53-4, 2002.

[32] V. B. Mendes and E.C. Pavlis, High-accuracy zenith delay at optical wavelengths, in *Geophysical Research Letters,* vol. 31, 2004.

[33] A. E. Niell, Global mapping function for the atmosphere delay at radio wavelengths, in *Journal of Geophysical Research,* vol. 101, n° B2, pp. 3227-3246, 1996.

[34] A. E. Niell, Improved atmospheric mapping functions for VLBI and GPS, in *Earth Planets Space,* vol. 52, pp. 699-702, 2000.

[35] NOAA radiosonde observations website, http ://raobs.fsl.noaa.gov.

[36] J.C. Owens, Optical Refractive Index of Air: Dependence on Pressure, Temperature and Composition, in *Applied Optics,* vol. 6, n° 1, pp. 51-59, January 1967.

[37] N. Penna, A. Dodson and W. Chen, Assessment of EGNOS Tropospheric Correction Model, in *Journal of Navigation,* vol 54(1), pp 37-55, 2001 (espace.lis.curtin.edu.au/archive/00000013/01/Journal_of_Nav54(1)_penna.pdf)

[38] Rogers & Yau, *A Short Course in Cloud Physics*, Pergamon Press.

[39] RTCA, *Minimum operational performance standards for Global Positioning System/Wide Area Augmentation System airborne equipment,* 6 October 1999.

[40] J. M. Rüger, Refractive Index Formulae for Radio Waves, Proceedings, *FIG XXII International Congress*, Washington DC, 19-26 April 2002. (www.fig.net/pub/fig_2002/Js28/JS28_rueger.pdf)

[41] J. Saastmoinen, Atmospheric Correction for the Troposphere and Stratosphere in Radio Ranging of Satellites, in *The Use of Artificial Satellites for Geodesy, Geoph. Monogr. Ser.,* vol 15, edited by S. W. Henriksen and al., pp. 247-251, AGU, Washington, D. C., 1972.

[42] E. K. Smith and S. Weintraub, The Constants in the Equation for Atmospheric Refractive Index at Radio Frequencies, in *Proceedings of the institute of Radio Science,* 41, pp. 1035-1037, 1953.

[43] W. L. Smith, Note on the Relationship Between Total Precipitable Water and Surface Dew Point, *Journal of applied Meteorology,* vol. 5, pp. 726-727, 1966.

[44] J. J. Spilker Jr., Tropospheric Effects on GPS, in Parkinson & Spilker (eds.) *GPS Theory and Applications*, vol.1, Progress in Astronautics ans Aeronautics, vol. 163, pp. 517-546, 1996.

[45] T. Schüler, *On Ground-based GPS Tropospheric Delay Estimation,* Schriftenreihe, Studiengang Geodäsie und Geoinformation, Universität ser Bundeswehr Münche,, vol. 73, 2001.

[46] G. D. Thayer, An improved equation for the radio refractive index, in *Radio Science,* vol. 9, n° 10, pp. 803-807, October 1974.

[47] H. Vömel, *Saturation vapor pressure formulation,* http://cires.colorado.edu/~voemel/vp.html, University of Colorado, Boulder, April 2004.

[48] J. M. Wallace & P. V. Hobbs, *Atmospheric Science: An Introductory Survey,* Academic Press.

[49] World Meteorological Organisation, *Guide to Meteorological Instruments and Methods of Observation, Fifth edition*, Secretariat of the World Meteorological Organisation, Geneva, 1983.